



저작자표시-비영리-변경금지 2.0 대한민국

이용자는 아래의 조건을 따르는 경우에 한하여 자유롭게

- 이 저작물을 복제, 배포, 전송, 전시, 공연 및 방송할 수 있습니다.

다음과 같은 조건을 따라야 합니다:



저작자표시. 귀하는 원저작자를 표시하여야 합니다.



비영리. 귀하는 이 저작물을 영리 목적으로 이용할 수 없습니다.



변경금지. 귀하는 이 저작물을 개작, 변형 또는 가공할 수 없습니다.

- 귀하는, 이 저작물의 재이용이나 배포의 경우, 이 저작물에 적용된 이용허락조건을 명확하게 나타내어야 합니다.
- 저작권자로부터 별도의 허가를 받으면 이러한 조건들은 적용되지 않습니다.

저작권법에 따른 이용자의 권리는 위의 내용에 의하여 영향을 받지 않습니다.

이것은 [이용허락규약\(Legal Code\)](#)을 이해하기 쉽게 요약한 것입니다.

[Disclaimer](#)

공학박사 학위논문

**Development of Solution  
Processable Carbon Nanomaterials  
and Its Application to Composite  
and Thin-Film Transistor**

용액공정이 가능한 탄소나노물질의 개발과 이를  
이용한 복합재료와 박막트랜지스터의 제조

2014년 2월

서울대학교 대학원

재료공학부

김 경 태

# Development of Solution Processable Carbon Nanomaterials and Its Application to Composite and Thin-Film Transistor

지도 교수 조 원 호

이 논문을 공학박사 학위논문으로 제출함  
2013년 12월

서울대학교 대학원  
재료공학부  
김 경 태

김경태의 박사 학위논문을 인준함  
2013년 12월

위 원 장	_____	(인)
부위원장	_____	(인)
위 원	_____	(인)
위 원	_____	(인)
위 원	_____	(인)

**Abstract**

**Development of Solution  
Processable Carbon Nanomaterials  
and Its Application to Composite  
and Thin-Film Transistor**

Kyung Tae Kim

Department of Materials Science and Engineering  
The Graduate School  
Seoul National University

The solution processable carbon-based nanomaterials, in particular carbon nanotube (CNT) and graphene, were synthesized and functionalized for efficient and easy application. First, a new compatibilizer, poly(vinyl benzyloxy ethyl naphthalene)-*g*-poly(methyl methacrylate), for poly(styrene-*co*-acrylonirile) (SAN)/multi-walled carbon nanotubes (MWCNTs) composites was synthesized. It has been identified that naphthalene unit in backbone of compatibilizer interacts with MWCNTs via  $\pi$ - $\pi$  interaction and that the graft chain of the compatibilizer is miscible with the SAN matrix. When a small amount of compatibilizer was added to SAN/MWCNT composites, MWCNTs were more homogeneously dispersed in SAN matrix than the case without compatibilizer, indicating that the compatibilizer improves the compatibility between SAN and MWCNTs. As a consequence, mechanical and electrical properties of the composites with compatibilizer were largely improved as compared with those of composites without compatibilizer.

Second, A new compatibilizer, poly(vinyl benzyloxy methyl naphthalene)-*g*-poly(*t*-butyl methacrylate-*co*-methacrylic acid), was synthesized for Nylon 66 (N66)/ MWCNT composites. It has been shown that the carboxylic acid

unit in the graft chain of the compatibilizer interacts with the amide group of N66. The use of the compatibilizer produces well-dispersed MWCNTs in N66 matrix, which results in improved mechanical and electrical properties of the composites, while the simple mixture of N66/MWCNTs without the compatibilizer exhibits poor mechanical and electrical properties due to severe aggregation of MWCNTs. It is also found that the compatibilizer with a small amount of carboxylic acids is more effective for improving the mechanical and electrical properties of N66/MWCNT composites.

Third, novel precursor polymers containing phenylene, naphthalene and anthracene units were synthesized for fabrication of graphene nanoribbons (GNRs) by the Suzuki coupling reaction between dibrominated monomers and diboronic ester monomers. The precursor polymers were converted into GNRs by intramolecular cyclodehydrogenation. The degree of cyclodehydrogenation was determined by analysis of nuclear magnetic resonance spectra. All GNR films show ambipolar charge transport behavior in thin-film transistor (TFT). The GNR film prepared from anthracene-based polymer exhibits the highest TFT performance due to its longer conjugation length and larger width of nanoribbon than GNRs prepared from phenylene and naphthalene-based polymers.

Fourth, novel nitrogen-doped graphene nanoribbons (GNR-Ns) were synthesized by the coupling reaction between pyrazine (or benzene) derivative and naphthalene followed by cyclodehydrogenation. The amount of nitrogen doping in GNR-N was controlled by changing the monomer feed ratio of pyrazine to benzene for polymerization. The electron mobility of GNR-N increases while the hole mobility decreases, as the amount of nitrogen doping in GNR increases, indicating that the charge transport behavior of GNRs is changed from ambipolar to n-type semiconductor. The threshold voltage of GNR-Ns also shifts from 20 V to -6 V as the amount of nitrogen doping increases.

Finally, the water-soluble conducting polymer, polystyrenesulfonic acid-g-polyaniline (PSSA-g-PANI), easily exfoliates graphenes from graphite and produces well-dispersed graphene in water, which results in improved capacitance of PSSA-g-PANI/graphene composites. It is also found that the longer length of PANI is more effective for improving the capacitance of

PSSA-g-PANI composites.

**Keywords:** carbon nanomaterial, solution process, carbon nanotube, compatibilizer, graphene, graphene nanoribbon, composite, thin-film transistor, supercapacitor, capacitance.

**Student Number:** 2011-30181

# Contents

<b>Chapter 1 Introduction .....</b>	<b>1</b>
1.1 Carbon nanomaterials .....	1
1.2 Polymer/carbon nanotube composites .....	13
1.3 Graphene nanoribbon (GNR).....	21
1.4 Graphene electrode for supercapacitor .....	28
1.5 Objectives of this study.....	31
<b>Chapter 2 Experimental .....</b>	<b>38</b>
2.1 Synthesis of compatibilizers .....	38
2.1.1 Materials.....	38
2.1.2 Synthesis of compatibilizer for SAN/MWCNT composite..	39
2.1.3 Synthesis of compatibilizer for Nylon 66 (N66) /MWCNT composite .....	41
2.1.4 Preparation of composite films.....	43
2.2 Synthesis of GNRs .....	45
2.2.1 Materials.....	45
2.2.2 Synthesis of GNRs.....	45
2.2.3 Synthesis of GNR-Ns.....	48
2.2.4 Thin-film transistor (TFT) fabrication .....	51
2.3 Preparation of graphene/PSSA-g-PANI composites.....	53
2.4 Measurements .....	55
2.4.1 Characterization methods.....	55
2.4.2 Composite properties measurements .....	56
2.4.3 TFT performance measurements .....	56
2.4.4 Capacitance measurement .....	57
<b>Chapter 3 Results and Discussion .....</b>	<b>58</b>
3.1 SAN/compatibilizer/MWCNT composites .....	58
3.1.1 Synthesis and characterization.....	58
3.1.2 Identification of interactions .....	58
3.1.3 Dispersity of MWCNTs in SAN matrix.....	63

3.1.4	Tensile properties of composites .....	68
3.1.5	Electrical properties .....	72
3.1.6	Summary .....	75
3.2	N66/compatibilizer/MWCNT composites .....	79
3.2.1	Synthesis and characterization.....	79
3.2.2	Identification of interactions .....	80
3.2.3	Dispersity of MWCNTs in N66 matrix.....	88
3.2.4	Tensile properties of composites .....	88
3.2.5	Electrical properties .....	94
3.2.6	Effect of the number of carboxylic acid groups .....	97
3.2.6	Summary .....	102
3.3	Graphene nanoribbons .....	103
3.3.1	Synthesis and characterization.....	103
3.3.2	Identification of cyclodehydrogenation .....	104
3.3.3	TFT performance .....	112
3.3.4	Crystallinity of GNRs .....	112
3.3.5	Summary .....	121
3.4	Nitrogen-doped graphene nanoribbons.....	122
3.4.1	Synthesis and characterization.....	128
3.4.2	Identification of cyclodehydrogenation .....	123
3.4.3	Nitrogen doping.....	129
3.4.4	TFT performance .....	129
3.4.5	Summary .....	132
3.5	Graphene electrode for supercapacitor.....	135
3.4.1	Exfoliation of graphene.....	135
3.4.2	Capacitance .....	135
3.4.3	Summary .....	138

**Chapter 4 Conclusions .....** 143

**Bibliography.....** 147

**Korean Abstract.....** 162

## List of Tables

Table 1.1	Theoretical and experimentally measured properties of CNTs .....	14
Table 3.1	Molecular characteristics of compatibilizers .....	61
Table 3.2	Molecular characteristics of compatibilizers .....	85
Table 3.3	Mechanical and electrical properties of composites with 1 wt.% MWCNTs.....	101
Table 3.4	Hole and electron mobility of GNRs.....	115
Table 3.5	Interchain and $\pi$ - $\pi$ stacking distance of GNRs .....	119
Table 3.6	Electrochemical property and charge carrier mobility and threshold voltage of GNR-Ns .....	131
Table 3.7	Characteristic of PSSA-g-PANI and capacitance of composites. .....	141

## List of Schemes

Scheme 3.1	The overall synthesis route of the compatibilizer, PVBEN- <i>g</i> -PMMA.....	59
Scheme 3.2	Synthesis route of compatibilizers, PVBMN- <i>g</i> -P( <i>t</i> BMA- <i>co</i> -MAA)s.....	81
Scheme 3.3	Synthetic routes of GNRs .....	105
Scheme 3.4	Synthesis route of GNR-Ns.....	124

## List of Figures

Figure 1.1	Carbon-based nanomaterials .....	3
Figure 1.2	Schematic representation of a single graphite sheet with hexagonal carbon lattice and wrapping vector $C_h$ (A) and chirality of CNTs (B).....	8
Figure 1.3	Graphene and GNRs with armchair (transverse strip) and zigzag edges (longitudinal strip). .....	22
Figure 1.4	(a) SWCNT and GNR. Different techniques for unzipping of CNTs: (b) plasma etching of partially embedded CNTs; (c) longitudinal cutting of CNTs by chemical attack; (d) intercalation of alkali metal atoms followed by exfoliation of CNTs; and (e) metal particle catalyzed cutting of CNTs. (f) Final GNRs. ....	24
Figure 2.1	Chemical structure, $^1\text{H}$ NMR spectrum (a) and GPC trace (b) of poly(styrene- <i>co</i> -acrylonitrile) (SAN). ....	40
Figure 2.2	Chemical structure of PSSA- <i>g</i> -PANI.....	54
Figure 3.1	Chemical structures and $^1\text{H}$ NMR spectra of P(CMS- <i>co</i> -VBEN) (a) and PVBEN- <i>g</i> -PMMA (b).....	60
Figure 3.2	GPC traces of PCMS, P(CMS- <i>co</i> -VBEN) and PVBEN- <i>g</i> -PMMA.....	61
Figure 3.3	Fluorescence emission spectra of compatibilizer in chloroform solution (a) and in film (b). ....	64
Figure 3.4	Raman spectra of the MWCNT (a), SAN/MWCNT (b), and SAN/MWCNT/C (c) with 1 wt.% MWCNTs. ....	65
Figure 3.5	DSC thermograms of compatibilizer, SAN, SAN/compatibilizer with 10 wt.% compatibilizer .....	66
Figure 3.6	FE-SEM images of SAN/MWCNT composite using P(CMS- <i>co</i> -VBEN) without PMMA graft chain. The content of MWCNTs is 1 wt.%.....	67
Figure 3.7	TGA traces of MWCNT, SAN, SAN/MWCNT, SAN/MWCNT/C with 1 wt.% MWCNTs.....	69
Figure 3.8	TEM images of (a) SAN/MWCNT and (b) SAN/MWCNT/C with 1 wt.% MWCNTs .....	70

Figure 3.9	FE-SEM images of the fracture surface of (a) SAN/MWCNT and (b) SAN/MWCNT/C with 1 wt.% MWCNTs. Right side images are magnified ones.....	71
Figure 3.10	Stress-strain curves for the neat SAN, SAN/MWCNT, and SAN/MWCNT/C with 0.5 wt.% MWCNTs .....	73
Figure 3.11	Tensile properties of SAN/MWCNT ( $\Delta$ ) and SAN/MWCNT/C ( $\circ$ ) composites as a function of the MWCNT content.....	74
Figure 3.12	Electrical conductivity of SAN/MWCNT and SAN/MWCNT/C composite films as a function of MWCNT content .....	76
Figure 3.13	Determination of percolation threshold concentration of SAN/MWCNT (a) and SAN/MWCNT/C (b) composite films .....	77
Figure 3.14	Chemical structure and $^1\text{H}$ NMR spectra of P(CMS- <i>co</i> -VBMN).....	82
Figure 3.15	Chemical structure and $^1\text{H}$ NMR spectra of PVBMN- <i>g</i> -PtBMA.....	83
Figure 3.16	Chemical structure and $^1\text{H}$ NMR spectra of PVBMN- <i>g</i> -P( <i>t</i> BMA- <i>co</i> -MAA).....	84
Figure 3.17	FT-IR spectra before and after hydrolysis of PVBMN- <i>g</i> -PtBMA.....	86
Figure 3.18	Fluorescence emission spectra of compatibilizer in solution (a) and in film (b) .....	89
Figure 3.19	Raman spectra of the MWCNTs (a), N66/MWCNT (99/1 w/w) (b), and N66/MWCNT/C44 (99/1/1 w/w/w) (c) with 1 wt.% MWCNTs.....	90
Figure 3.20	FT-IR spectra of N66 and N66/C44. Close examination reveals that the absorption band of hydrogen-bonded N-H stretching of N66/C44 at $3300\text{ cm}^{-1}$ is stronger than that of N66.....	91
Figure 3.21	TEM images of N66/MWCNT (a) and N66/MWCNT/C44 (b).....	92
Figure 3.22	FE-SEM images of the fracture surface of N66/MWCNT (a) and N66/MWCNT/C44 (b) with 1 wt.% MWCNTs. Right	

	side images are magnified ones.....	93
Figure 3.23	Tensile properties of N66/MWCNT ( $\Delta$ ) and N66/MWCNT/C44 ( $\circ$ ) composites as a function of the MWCNT content.....	95
Figure 3.24	DSC thermograms of neat N66, N66/MWCNT, N66/MWCNT/C44 with 1 wt.% MWCNT.....	96
Figure 3.25	Electrical conductivity of N66/MWCNT and N66/MWCNT/C44 composites.....	98
Figure 3.26	Percolation threshold concentration of N66/MWCNT ( $\Delta$ ) and N66/MWCNT/C44 ( $\circ$ ) composites.....	99
Figure 3.27	Fluorescence emission spectra of N66/MWCNT composites with different compatibilizers (C44, C66 and C130).....	101
Figure 3.28	Chemical structure and $^1\text{H}$ NMR spectra of (a) Poly-An and (b) GNR-An.....	106
Figure 3.29	Chemical structure and $^1\text{H}$ NMR spectra of (a) Poly-Ph and (b) GNR-Ph.....	107
Figure 3.30	Chemical structure and $^1\text{H}$ NMR spectra of (a) Poly-Np and (b) GNR-Np.....	108
Figure 3.31	Chemical structure and $^{13}\text{C}$ NMR spectra of (a) Poly-An and (b) GNR-An.....	109
Figure 3.32	Chemical structure and $^{13}\text{C}$ NMR spectra of (a) Poly-Ph and (b) GNR-Ph.....	110
Figure 3.33	Chemical structure and $^{13}\text{C}$ NMR spectra of (a) Poly-Np and (b) GNR-Np.....	111
Figure 3.34	UV-Vis absorption spectra of (a) Poly-An and GNR-An, (b) Poly-Np and GNR-Np, and (c) Poly-Ph and GNR-Ph.....	113
Figure 3.35	Raman spectra of (a) Poly-An and GNR-An, (b) Poly-Np and GNR-Np, and (c) Poly-Ph and GNR-Ph.....	114
Figure 3.36	GPC chromatograms of precursor polymers and GNRs.....	115
Figure 3.37	Transfer curves of field-effect transistor based on (a) GNR-Ph, (b) GNR-Np and (c) GNR-An. Dotted line: transfer curve of current versus gate voltage at positive source-drain bias (+60 V). Solid line: transfer curve of current versus gate voltage at negative source-drain bias (-60 V).....	116

Figure 3.38	Output curves of field-effect transistor based on GNR-Ph (a), GNR-Np (b) and GNR-An (c). Left: output curve as a function of gate voltage at negative source-drain bias. Right: output curve as a function of gate voltage at positive source-drain bias.....	117
Figure 3.39	DSC thermograms of three GNRs .....	119
Figure 3.40	XRD spectra of three GNRs .....	120
Figure 3.41	Schematic representation of GNR-An crystal orientation... ..	120
Figure 3.42	Chemical structure and <sup>1</sup> H NMR spectra of Poly-N50 .....	125
Figure 3.43	Chemical structure and <sup>1</sup> H NMR spectra of (a) Poly-N100 (b) GNR-N100.....	126
Figure 3.44	UV-Vis absorption spectra of (a) Poly-N0 and GNR-N0, (b) Poly-N50 and GNR-N50, and (c) Poly-N100 and GNR-N100 .....	127
Figure 3.45	Raman spectra of (a) Poly-N0 and GNR-N0, (b) Poly-N50 and GNR-N50, and (c) Poly-N100 and GNR-N100.....	128
Figure 3.46	Cyclovoltammograms (a) and G-band frequency (b) of GNR-N0, GNR-N50 and GNR-N100 .....	130
Figure 3.47	XRD spectra of three GNR-Ns .....	131
Figure 3.48	Transfer curves of field-effect transistor based on (a) GNR-N0, (b) GNR-N50 and (c) GNR-N100. The drain-source voltage for transfer characteristics was –60 V and the field effect mobility ( $\mu$ ) was measured from the transfer curve in the saturation regime and calculated from the gradient of transfer curve.....	133
Figure 3.49	UV-Vis absorption spectra of graphite, PSSA-g-PANI and PSSA-g-PANI/graphene solutions.....	136
Figure 3.50	AFM image and height profile of exfoliated graphene .....	137
Figure 3.51	Cyclic voltammograms of PSSA-g-PANI/graphene composites: (a) COMP#1-1; (b) COMP#1-2; (c) COMP#2-1; (d) COMP#2-2; (e) COMP#3-1; (d) COMP#3-2 .....	139
Figure 3.52	Specific capacitance with scan rate.....	140
Figure 3.53	Cyclic performance of COMP#2-2 .....	142

# Chapter 1. Introduction

## 1.1 Carbon nanomaterials

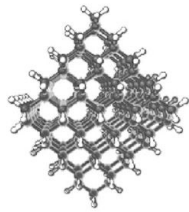
Recently, the emerging need for high-speed electronics and renewable energy has motivated researchers to discover, develop, and assemble new classes of nanomaterials in unconventional device architectures. Among these materials, carbon-based nanomaterials have attracted particular attention due to their unique structural and physical properties. Carbon nanomaterials, composed of  $sp^2$  bonded graphitic carbon, are found in all reduced dimensionalities including zero-dimensional fullerenes, one-dimensional carbon nanotubes (CNTs), and two-dimensional graphene. With nanometer-scale dimensions, the properties of carbon nanomaterials are strongly dependent on their atomic structures and interactions with other materials. Zero-dimensional, one-dimensional, and two-dimensional carbon nanomaterials have attracted significant attention from the scientific community due to their unique electronic, optical, thermal, mechanical, and chemical properties. Base on the remarkable properties, many applications for carbon nanomaterials, including composites, sensors, electronic devices, optoelectronic devices and photovoltaic devices, have been reported. Consequently, significant recent effort has been devoted to the mass production of structurally homogeneous samples and their large-scale assembly into device architectures with well controlled surfaces and

interfaces. Thus, carbon nanomaterials opening up a new era in materials science and nanotechnology been considered as the core material in the field of materials science in 21st century.

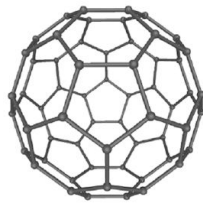
### **1.1.1 Carbon allotropes**

Carbon is well known to form distinct solid state allotropes with diverse structures and properties ranging from  $sp^3$  hybridized diamond to  $sp^2$  hybridized graphite. The physical, chemical, and electronic properties of carbon nanomaterials are strongly coupled to carbon's structural conformation and, thus, its hybridization state.<sup>1</sup> The ground-state orbital configuration of carbon's six electrons is  $1s^2, 2s^2, 2p^2$ . The narrow energy gap between the 2s and 2p electron shells facilitates the promotion of one s orbital electron to the higher energy p orbital that is empty in the ground state. Depending on bonding relationships with the neighboring atoms, this promotion allows carbon to hybridize into a  $sp$ ,  $sp^2$ , or  $sp^3$  configuration. The energy gained from covalent bonding with adjacent atoms compensates for the higher energy state of the electronic configuration. This compensation is nearly equal for the  $sp^2$  and  $sp^3$  hybridization states after the out-of-plane bonding due to  $\pi$  bonds among unhybridized p orbitals is considered. These mutable hybridization states account for the diversity of organic compounds as well as the considerable differences among carbon's bulk configuration, as shown in Figure 1.1.

Diamond is a metastable form of carbon that possesses a three-



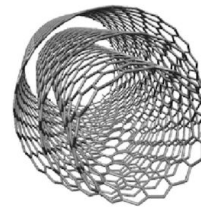
**Diamond**



**Fullerene**



**SWCNT**



**MWCNT**



**Graphene**

**Figure 1.1.** Carbon-based nanomaterials

dimensional cubic lattice with a lattice constant of 3.57 Å and C–C bond length of 1.54 Å. In contrast, graphite is the most thermodynamically stable form of carbon at room temperature and consists of a layered two-dimensional structure where each layer possesses a hexagonal honeycomb structure of sp<sup>2</sup> bonded carbon atoms with a C–C bond length of 1.42 Å. These single atom thick layers (i.e., graphene layers) interact via noncovalent van der Waals forces with an interlayer spacing of 3.35 Å. The weak interlayer bonding in graphite implies that single graphene layers can be exfoliated via mechanical or chemical methods as will be outlined in detail below. Graphene is often viewed as the two-dimensional building block of other sp<sup>2</sup> hybridized carbon nanomaterials in that it can be conceptually rolled or distorted to form carbon nanotubes and fullerenes.

Fullerenes are the zero-dimensional form of graphitic carbon that can be visualized as an irregular sheet of graphene being curled up into a sphere by incorporating pentagons in its structure. Fullerenes come in various forms and sizes ranging from 30 to 3000 carbon atoms. As a fullerene is elongated in one dimension, it approaches the structure of a CNT. Conceptually, CNTs are seamless cylinders of single or few layered graphene with a high aspect ratio (i.e. length to diameter ratio) that ranges from 10<sup>2</sup> to 10<sup>7</sup>. The structure, diameter, and electronic type of a single-walled carbon nanotube (SWCNT) are determined by the chiral vector (i.e., roll-up vector) that defines the circumference of the SWCNT with respect to the graphene lattice. Multi-walled carbon nanotubes (MWCNTs) consist of nested, concentric shells of SWCNTs with a spacing between individual walls of 3.4 Å.

### 1.1.2 Fullerene

The electronic structure of fullerenes determines their unique chemical, optical, and structural properties. In defect-free form, fullerenes are enclosed cage-like structures comprised of twelve 5-member rings and an unspecified number of 6-member rings. Structures with fewer hexagons exhibit greater  $sp^3$  bonding character, higher strain energies, and more reactive carbon sites. Isomers with adjacent pentagons also display lower stability and relative abundance than isomers with isolated pentagons in which resonance structures delocalize  $\pi$  bonds over the fullerene structure.<sup>2,3</sup> While the extent of charge delocalization is debated, the chemical behavior of C60 lies between an aromatic molecule and a straight chained alkene.<sup>4</sup>

This balance between stability and reactivity distinguishes Buckminsterfullerene, C60, from the degenerate C20 fullerenes and planar graphite. C60 is a symmetric fullerene<sup>5</sup> stabilized by resonance structures supporting an equivalent electronic state and bonding geometry for each carbon atom.<sup>6</sup> The relative stability imparted by this symmetry has redefined C60 as a starting material for chemical reactions in its own right. Though C60 is highly resistant to oxidation, up to six electrons can be accommodated in the lowest unoccupied molecular orbital (LUMO). This opens the route to covalent chemistry and the exploitation of fullerenes as structural scaffolding for reactive adducts.

The electric and conductive properties of fullerenes and other carbonaceous nanomaterials form the basis for many of their unique

characteristics on the nanoscale. Thus, modification of these electric properties via single substitution or endohedral doping has generated significant research attention. Single atom substitutions in a fullerene structure have ramifications for the photosensitivity and binding energies of the fullerene molecule. With an internal diameter of 0.7 nm,<sup>7</sup> the C60 fullerene cage may also be endohedrally doped for electronic modification, transport of interstitial atoms, or dissolution and vaporization processes of otherwise refractory metals.<sup>8</sup> Select endohedral dopants induce rehybridization of the fullerene molecule via ionic interactions and charge transfer,<sup>9</sup> whereas others exhibit little effect on the basic properties of the fullerene molecule. Carbon nanomaterial research has also characterized other fullerene conformations including a group of very large spherical fullerenes<sup>10</sup> and a class of concentric fullerenes titled carbon onions.<sup>11</sup>

An important physicochemical attribute of fullerenes is their tendency to form stable crystalline nanoparticles (25-500 nm in diameter) in a variety of solutions, including water at environmentally relevant pH and electrolyte concentrations.<sup>12-14</sup> In the absence of humic acid, aggregation behavior of the fullerenes is consistent with the classic Derjaguin-Landau-Verwey-Overbeek (DLVO) theory of colloidal stability. Average aggregate diameter exhibits dependence on pH, ionic strength, mixing behavior, initial fullerene concentration, and time in solution.<sup>15-16</sup> In the presence of humic acid, however, absorption of macromolecules to the fullerene nanoparticles induces steric stabilization and sharply reduces aggregation rates.<sup>17</sup>

### 1.1.3 Carbon nanotube

CNTs can be constructed by wrapping up a single-layer graphene into a seamless cylinder (see Figure 1.2). In other words, they can be thought as hollow cylinder of a graphene sheet. CNTs, according to the number of the concentric graphene sheet, can be classified into two categories: SWCNT and MWCNT. SWCNT which is the fundamental form of CNTs consists of a single SWCNTs which are the fundamental form of CNTs consist of a single graphite sheet. Generally, the diameter of SWCNTs is very small ( $\sim 1$  nm) and its distribution is very narrow ( $0.7 \sim 2$  nm) Meanwhile, MWCNTs consist of several graphite sheets coaxially arranged around a central hollow core. Typically, its outer diameter ranges from 2 to 100 nm, while its inner diameter is about  $1 \sim 3$  nm. Although both types of CNTs have a diameter in nanometer range, their length ranges from several micrometers up to a few millimeters. In other words, they have a high aspect ratio, which leads individual CNTs to severely aggregate when they are synthesized.

There are many ways to roll a graphite sheet into a cylinder, resulting in different diameters and microscopic structures of the CNTs, as can be seen Figure 1.2A, the wrapping vector  $\mathbf{C}_h$ , which defines the relative location of the two sites of graphite sheet, is given by

$$\mathbf{C}_h = n\mathbf{a}_1 + m\mathbf{a}_2$$

where  $n$  and  $m$  a pair of integers and  $\mathbf{a}_1$  and  $\mathbf{a}_2$  are two unit vectors. Based on their hexagonal lattice structure, CNTs are classified as armchair, zigzag, and chiral. As can be seen in Figure 1.2B, CNTs are called ‘armchair’ type if  $n$

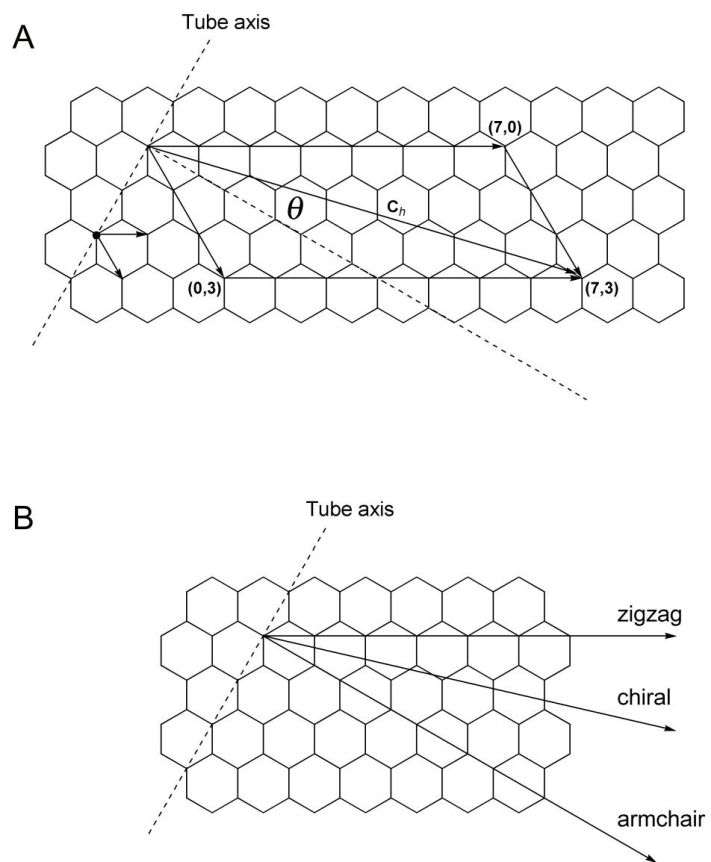


**Figure 1.2.** Schematic representation of a single graphite sheet with hexagonal carbon lattice and wrapping vector  $C_h$  (A) and chirality of CNTs (B)

equals  $m$ , and ‘zigzag’ type in the case  $m = 0$ . All other CNTs are of the ‘chiral’ type and have a finite wrapping angle  $\theta$  with  $0^\circ < \theta < 30^\circ$ . All armchair type CNTs are electrically conductive (metallic character), while the zigzag and chiral CNTs can be either metallic or semiconducting.

The first observations of CNTs and their subsequent large-scale synthesis using arc discharge techniques were reported by Iijima and coworkers.<sup>18-19</sup> Laser ablation was later demonstrated as an alternative method for growing CNTs by Smalley group.<sup>20-21</sup> Since it was observed that transition metals embedded in graphite electrodes/targets produced carbon nanotubes with higher yield and reproducibility,<sup>22</sup> chemical vapor deposition (CVD) using transition metal nanoparticle catalysts was then developed to produce high quality single-walled and multi-walled CNTs in vertically aligned arrays.<sup>23-24</sup> Vertically aligned arrays can also be grown on metallic<sup>25</sup> and quasicrystalline substrates. Extending the metal nanoparticle catalyst concept, CNTs were later synthesized by pyrolysing metal carbonyls in the presence of other hydrocarbons.<sup>26-27</sup> When optimized in a high pressure carbon monoxide (HiPco) environment, the carbonyl pyrolysis process led to high yield production of SWCNTs.<sup>28</sup> CNTs synthesized by arc discharge, HiPco, and CVD (using Co-Mo catalysts) are now commercially available in kilogram quantities.

#### **1.1.4 Graphene**

Graphene is the name given to a two-dimensional sheet of sp<sup>2</sup>-hybridized

carbon. Its extended honeycomb network is the basic building block of other important allotropes; it can be stacked to form 3D graphite, rolled to form 1D nanotubes, and wrapped to form 0D fullerenes. Long-range  $\pi$ -conjugation in graphene yields extraordinary thermal, mechanical, and electrical properties, which have long been the interest of many theoretical studies and more recently became an exciting area for experimentalists. While studies of graphite have included those utilizing fewer and fewer layers for some time, the field was delivered a jolt in 2004, when Geim and co-workers first isolated single-layer samples from graphite.<sup>29</sup> This led to an explosion of interest, in part because two-dimensional crystals were thought to be thermodynamically unstable at finite temperatures. Quasi-two dimensional films grown by molecular beam epitaxy are stabilized by a supporting substrate, which often plays a significant role in growth and has an appreciable influence on electrical properties. In contrast, the mechanical exfoliation technique used by the Manchester group isolated the two-dimensional crystals from three-dimensional graphite.

The experimental isolation of single-layer graphene first and foremost yielded access to a large amount of interesting physics. Initial studies included observations of graphene's ambipolar field effect,<sup>29</sup> the quantum Hall effect at room temperature,<sup>30-31</sup> measurements of extremely high carrier mobility,<sup>32</sup> and even the first ever detection of single molecule adsorption events.<sup>33</sup> These properties generated huge interest in the possible implementation of graphene in a myriad of devices. These include future generations of high-speed and radio frequency logic devices, thermally and electrically conductive

reinforced composites, sensors, and transparent electrodes for displays and solar cells.

Despite intense interest and continuing experimental success by device physicists, widespread implementation of graphene has yet to occur. This is primarily due to the difficulty of reliably producing high quality samples, especially in any scalable fashion. The challenge is really 2-fold because performance depends on both the number of layers present and the overall quality of the crystal lattice. So far, the original top-down approach of mechanical exfoliation has produced the highest quality samples, but the method is neither high throughput nor high-yield. In order to exfoliate a single sheet, van der Waals attraction between exactly the first and second layers must be overcome without disturbing any subsequent sheets. Therefore, a number of alternative approaches to obtaining single layers have been explored, a few of which have led to promising proof-of-concept devices.

Alternatives to mechanical exfoliation include primarily three general approaches: chemical efforts to exfoliate and stabilize individual sheets in solution,<sup>34-36</sup> bottom-up methods to grow graphene directly from organic precursors,<sup>37,38</sup> and attempts to catalyze growth in situ on a substrate.<sup>39-42</sup> Each of these approaches has its drawbacks. For chemically derived graphene, complete exfoliation in solution so far requires extensive modification of the 2D crystal lattice, which degrades device performance.<sup>43</sup> Alternatively, bottom-up techniques have yet to produce large and uniform because macromolecules become insoluble and the occurrence of side reactions increases with molecular weight.<sup>44</sup> Substrate-based growth of single layers by

CVD or the reduction of silicon carbide relies on the ability to walk a narrow thermodynamic tightrope. After nucleating a sheet, conditions must be carefully controlled to promote crystal growth without seeding additional second layers or forming grain boundaries.

Despite tremendous progress with alternatives, mechanical exfoliation with cellophane tape still produces the highest quality graphene flakes available. This fact should not, however, dampen any interest from chemists. On the contrary, the recent transition from the consideration of graphene as a “physics toy” to its treatment as a large carbon macromolecule offers new promise. Years of carbon nanotube, fullerene, and graphite research have produced a myriad of chemical pathways for modifying sp<sup>2</sup> carbon structures,<sup>45-48</sup> which will undoubtedly be adapted to functionalize both the basal plane of graphene and its reactive edges. This not only promises to deliver handles for exploiting graphene’s intrinsic properties but also should lead to new properties altogether.

## 1.2 Polymer/CNT composite

Among the potential applications of CNTs, the first realized one is to use them as filler for polymer composites due to their remarkable physical properties as listed in Table 1.1.<sup>49-53</sup> The extremely small size of CNTs, together with remarkable mechanical properties, also make them ideal filler for polymer composites. In fact, CNTs can be regarded as the ideal carbon fiber which has been widely used in industry for several decades. However, the most obvious difference between CNTs and carbon fiber arises from the small diameter of CNTs, which offers a number of advantages. For instance, CNTs incorporated into matrix polymer create exceptionally large interfacial area in the composites, indicating that it is possible to improve various physical properties of matrix polymer by only small amount of CNTs loading. Owing to the superior electrical conductivity,<sup>54-56</sup> the potential of them as conducting filler for polymer composites has been proposed. The polymer materials which are intrinsic insulator become electrically conductive when the content of CNTs exceeds a critical value, known as a percolation threshold. In particular, CNTs are more favorable to decrease the percolation threshold concentration when compared to the conventional conductive filler such as carbon black due to their high aspect ratio.

In spite of the aforementioned remarkable properties of CNTs, there are some critical problems on the use of CNTs as filler for polymer composites. The most critical problem arises from the fact that CNTs in polymer matrix are aggregated by strong van der Waals force. Therefore, a number of studies

**Table 1.1** Theoretical and experimentally measured properties of CNTs.

Property	SWNCT	MWCNT
Specific gravity ( $\text{g}/\text{cm}^3$ )		0.8 ~ 1.8
Young's modulus (TPa)	~1	~0.3-1
Strength (GPa)	50-500	10-60
Electrical resistivity ( $\mu\Omega$ )		~5-50
Thermal conductivity ( $\text{W}\cdot\text{m}^{-1}\cdot\text{K}^{-1}$ )		3000 (theoretical)
Thermal expansion		Negligible (theoretical)
Oxidation in air ( $^{\circ}\text{C}$ )		> 700

on the preparation of polymer/CNTs composites have focused on how to achieve the homogeneous dispersion of CNTs throughout polymer matrix. Until now, several methods for the preparation of polymer/CNT composites have been developed, most of them can be classified as the following: solution blending, bulk mixing, melt blending, and grafting methods.

### **1.2.1 Solution blending**

The most common method for preparing polymer/CNT composites has been to mix both components into a suitable solvent and evaporate the latter to form a composite film. The general protocol for all solution processing methods includes the dispersion of CNTs in a liquid by vigorous stirring and/or sonication, mixing the CNT dispersion with a polymer solution and controlled evaporation of the solvent. Regarding thermosetting epoxy matrices, an early example of solution-based composite formation was described by Ajayan group.<sup>57</sup> In this work, MWCNTs produced by arc discharge were dispersed in ethanol by sonication and mechanically mixed with a mixture of epoxy monomer and curing agent. The epoxy/CNT mixture was poured into capsular molds and then cured. Electron microscopy images showed that slicing the composite material caused partial alignment of the CNTs on the cut surface. Concerning the fabrication of CNT-based composites with thermoplastic matrices, Jin et al.<sup>58</sup> have reported a similar method consisting of solution mixing, casting and drying. The chosen polymer, polyhydroxyaminoether (PHAE) was dissolved in the arc discharge-grown

CNTs in chloroform under sonication. The suspension was then poured into a Teflon mold and dried under ambient conditions for a certain time. Mechanical stretching of thin strips of the composite at 100 °C was found to cause orientation of CNTs in the axis of tension. Slight processing variations were used in most subsequent studies. Shaffer and Windle<sup>59</sup> dispersed chemically oxidized catalytic MWCNTs in water. The material was carefully blended with solutions of polyvinylalcohol in water to give composite dispersions which could be drop cast to form films with up to 60 wt% CNTs. In an alternative processing method, Zhou and coworkers<sup>60</sup> utilized a roll-casting technique to prepare composite films of poly(ethylenoxide) embedded with fluorinated CNTs.

### **1.2.2 Bulk mixing**

Milling is a mechanical process that leads to local generation of high pressure as a result of collisions throughout the grinding media. Concerning applications in CNT nanotechnology, this method has been used to shorten the lengths of carbon nanostructures.<sup>61</sup> A solid state mechanochemical pulverization process, namely pan milling, was used to prepare a polypropylene/CNT composite powder.<sup>62</sup> This powder was subsequently melt-mixed with a twin-roll masticator to obtain a homogeneous composite. The length of the CNTs was reduced from a few micrometers to ~500 nm. Similarly, high energy ball milling was utilized to incorporate CNTs into polymer matrices.<sup>63</sup> In this way, a satisfactory level of dispersion of CNTs into

the polymer matrix was obtained, resulting in an improvement of the physical properties of the samples. In addition, a mechanical–chemical high-speed vibration milling technique was applied for solubilizing CNTs in various media due to the formation of non-covalent-type complexes with species, such as cyclodextrins.<sup>64</sup>

### **1.2.3 Melt blending**

Due to the fact that thermoplastic semicrystalline polymers soften when heated above their melting point, melt processing has been a very valuable technique for the fabrication of CNT-based composites. In addition, the method is suitable for polymers that cannot be processed with solution techniques due to their insolubility in common solvents. In general, melt processing involves the blending of polymer melt with CNT material by application of intense shear forces. Depending on the final morphology/shape of the composites, the bulk samples can then be processed by several techniques, such as extrusion.<sup>65</sup> An early study on the melt mixing of SWCNTs and polymethyl methacrylate (PMMA) matrix was carried out by Winey and co-workers.<sup>66</sup> CNTs and PMMA were first blended in dimethylformamide and the resulting suspension was casted onto Teflon dishes and dried. The resultant films were broken up in small pieces and hot pressed to form a new film. This was then broken up and hot pressed, a process that was repeated as many as 25 times. The authors observed that the CNT dispersion improved with each melting step. Using a different protocol

for bulk composites, Goh and co-workers<sup>67</sup> have melt-blended MWCNTs and PMMA in a laboratory mixing molder at a speed of 120rpm (blending temperature  $\sim 200$  °C). The mixed samples were then compressed under pressure at 210 °C using a hydraulic press to yield composite films. Electron microscopy images showed that the nanotubes are well dispersed in the polymer matrix.

#### **1.2.4 Method ‘grafting to’**

In general, the ‘grafting to’ approach involves preformed polymer chains reacting with the surface of either pristine and oxidized or pre-functionalized CNTs. The main approaches exploited in this functionalization strategy are radical or carbanion additions as well as cycloaddition reactions to the CNT double bonds. Since the curvature of the carbon nanostructures imparts a significant strain upon the  $sp^2$  hybridized carbon atoms that make up their framework, the energy barrier required to convert these atoms to  $sp^3$  hybridization is lower than that of the flat graphene sheets, making them susceptible to various addition reactions. Therefore, to exploit this chemistry, it is only necessary to produce a polymer-centered transient in the presence of CNT material. Alternatively, defect sites on the surface of oxidized CNTs, as open-ended nanostructures with terminal carboxylic acid groups, allow covalent linkages of oligomer or polymer chains. The “grafting to” method onto CNT defect sites means that the readymade polymers with reactive end groups can react with the functional groups on the nanotube surfaces. In most

cases, polymer chains terminated with amino or hydroxyl moieties are attached by amidation or esterification reactions with the nanotube surface-bound carboxylic acid groups.<sup>68-70</sup>

An advantage of the “grafting to” method is that pre-formed commercial polymers of controlled molecular weight and polydispersity can be used. The main limitation of the technique is that initial binding of polymer chains sterically hinders diffusion of additional macromolecules to the CNT surface, leading to a low grafting density. Also, only polymers containing reactive functional groups can be used.

### **1.2.5 Method ‘grafting from’**

The ‘grafting from’ approach, in general, involves the polymerization of monomers from surface-derived initiators on either MWCNTs or SWCNTs. These initiators are covalently attached using the various functionalization reactions developed for small molecules, including acid defect group chemistry and sidewall functionalization of CNTs. The advantage of ‘grafting from’ approach is that the polymer growth is not limited by steric hindrance, allowing high molecular weight polymers to be efficiently grafted. In addition, polymer/CNT composites with quite high grafting density can be prepared. However, this method requires strict control of the amounts of initiator and substrate as well as accurate control of conditions required for the polymerization reaction. To demonstrate this approach, the well known living polymerization approaches have been employed in recent years because of

their tolerance to a wide variety of functional groups in the monomer units.<sup>71-</sup>

77

### 1.3 Graphene nanoribbon

Since graphene itself is a zero-bandgap semimetal, several methods have been reported to open bandgap of graphene. In several methods, graphene nanoribbon (GNR) with a width smaller than 10 nm show semiconducting behavior that renders them suitable active materials for electronic devices. When a 2D graphene sheet is cut into 1D GNRs, depending on the orientation of cutting, GNRs with various edge structures can be obtained, namely, armchair- or zigzag-edged GNRs (denoted aGNRs or zGNRs, respectively; Figure 1.3) and chiral ones. The bandgap of a GNR is essentially governed by the ribbon width and the edge configuration.<sup>78,79</sup> Besides, the carrier mobility and magnetic properties of edge atoms also depend on the specific edge configuration. By employing quantum approaches, Louie and co-workers demonstrated that all GNRs have energy gaps which decrease nearly linearly with increasing GNR width.<sup>78</sup>

A tunable bandgap is highly desirable for designing and fabricating electronic devices. The presence of edges and the finite widths of GNRs provides additional degrees of freedom to control the electronic properties of GNRs, for example, by tailoring the ribbon width<sup>80,81</sup> or edge functionalization.<sup>82</sup> Moreover, applying external electric fields,<sup>83</sup> doping,<sup>84-86</sup> functionalization,<sup>87-88</sup> and edge modification<sup>89-90</sup> can even turn zGNRs into half-metallic ferromagnets, in which the density of state of one spin orientation is metallic and that of another spin orientation is semiconducting. Therefore, application of zGNRs in spintronics, such as spin filters or spin

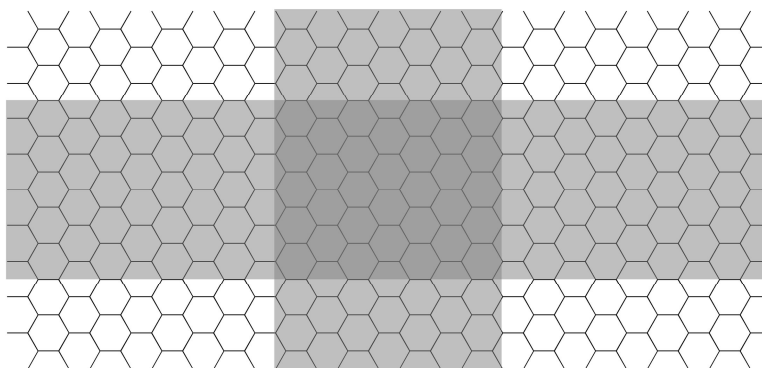


**Figure 1.3.** Graphene and GNRs with armchair (transverse strip) and zigzag edges (longitudinal strip).

logic gates, can be anticipated.

The predicated bandgap opening and the relationship between gap and ribbon width were confirmed experimentally.<sup>81,91,92</sup> The on/off ratio of sub-10 nm GNR FETs reached  $10^7$ .<sup>81,91</sup> In agreement with theoretical predictions, low-temperature ( $\approx 1.6$  K) electrical transport measurements on GNR-based FETs showed that the bandgap is indeed inversely proportional to the width of the GNR.<sup>93</sup> However, no obvious dependence of the electronic transport properties of the GNRs on orientation was observed experimentally. Some theoretical simulations on nonideal GNRs revealed that this inconsistency is mainly attributable to the enhanced localization induced by the edge roughness or reconstruction in real GNR-based devices.<sup>94-97</sup> This demonstrates the importance of controlling edge smoothness in the fabrication of high-performance GNR devices. Besides, experimental studies also indicated that impurities, doping, and gate material exert important influences on the transport performance of GNR FETs.<sup>78,98</sup>

Synthesis of high-quality GNRs with smooth edges and narrow and well-defined widths is crucial and a prerequisite for the development of GNR-based electronic and spintronic applications. Many methods, including lithographic patterning followed by plasma etching, sonochemical breaking of chemically derived graphene, metal-catalyzed or oxidation cutting of graphene, CVD, direct chemical synthesis, and unzipping of carbon nanotubes, have been developed.

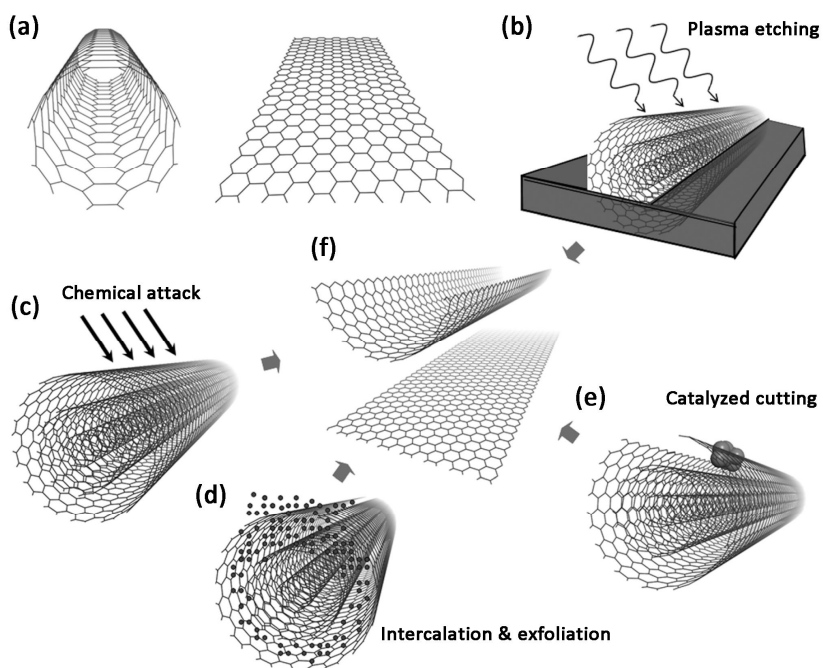


**Figure 1.4.** (a) SWCNT and GNR. Different techniques for unzipping of CNTs: (b) plasma etching of partially embedded CNTs; (c) longitudinal cutting of CNTs by chemical attack; (d) intercalation of alkali metal atoms followed by exfoliation of CNTs; and (e) metal particle catalyzed cutting of CNTs. (f) Final GNRs.

### 1.3.1 Unzipping CNTs

In principle, a single-walled carbon nanotube (SWCNT) can be viewed as a folded or zipped GNR (Figure 1.4). It is thus natural to seek the reverse process, that is, unzipping SWCNTs to synthesize GNRs. Many attempts have been dedicated to synthesizing GNRs experimentally (Figure 1.4), including plasma etching,<sup>99</sup> chemical attack,<sup>100</sup> intercalation and exfoliation,<sup>101,102</sup> sonochemical unzipping,<sup>103</sup> laser irradiation,<sup>104</sup> electrochemical unzipping,<sup>105</sup> catalytic cutting under microwave radiation<sup>106</sup> or by transition metal particles (e.g. Co, Ni, or Fe),<sup>107</sup> hydrogen treatment,<sup>108</sup> in situ STM manipulation<sup>109</sup> and electrical unwrapping of CNTs.<sup>110</sup>

### 1.3.2 Patterning and plasma etching of graphene

Kim and co-workers synthesized GNRs by employing the electron-beam lithography and etching technique.<sup>93</sup> Bulk graphene flakes were deposited onto Si/SiO<sub>2</sub> substrates and patterned, and then GNRs with various widths were obtained after removing the unprotected graphene area by oxygen plasma treatment. By employing silicon nanowires as etching masks in the lithography process, Huang et al. produced GNRs with controllable widths down to 6 nm. An 8 nm GNR FET showed a dramatically improved on/off ratio of about 160.<sup>111</sup> Other lithography methods like scan tunneling microscopy (STM) lithography were also successfully used to produce GNRs with well-defined armchair edges.<sup>112</sup> Nevertheless, the widths of GNRs

obtained by this technique were scattered over a broad range, and most of the edges were extremely rough. Hence, fabricated devices showed unpredictable performance.

### **1.3.3 Chemical oxidation cutting of graphene**

The chemical oxidation method is another feasible route for graphene cutting in large quantities because of its low cost and feasibility. Aksay et al. employed oxidation and thermal expansion methods on graphite to produce graphene sheet.<sup>113</sup> Graphite oxide (GO) was prepared by treating graphite with concentrated nitric and sulfuric acids, and gradually adding potassium chlorate to the mixture. Then the GO slurry was spray-dried (300 °C) and thermally exfoliated at high temperature (1050 °C) in a quartz tube. Fujii et al. used a scanning probe microscopic technique to cut oxidized graphene into nanosized islands.<sup>114</sup> The cutting procedure was triggered by the local mechanical stress caused by a point contact between the preoxidized graphene sheet and the AFM probe, leading to rupture of the sheet. However, in most of these experiments, only graphene quantum dots were produced due to the high symmetry of the honeycomb lattice of graphene.

### **1.3.4 Bottom-up methods**

The processes mentioned above are all top-down methods. Some bottom-up

strategies were also exploited to synthesis GNRs, such as CVD<sup>115,116</sup> and chemical synthesis.<sup>117,118</sup> The great advantage of the CVD method is bulk production (grams per day) of GNRs. The synthesized ribbons (< 20–30  $\mu\text{m}$  in length) have widths of 20–300 nm and thicknesses of 2–40 layers. The on/off ratio and mobilities can reach 10 at low temperature (4 K) and 2700  $\text{cm}^2/\text{V}\cdot\text{s}$  at room temperature, respectively. At present, the template CVD method is viewed as the most promising way to achieve mass production of GNRs, although the widths of GNRs should be narrowed and controlled in a small range in future development. On the other hand, self-assembly of planar graphene-like hydrocarbon molecules in one dimension led to successful synthesis of narrow GNRs with lengths of up to 12 nm. The advantage of this approach is precise control of composition and structure.

## 1.4 Graphene electrode for supercapacitor

Supercapacitors are supposed to be a promising candidate for alternative energy storage devices as a result of their high rate capability, pulse power supply, long cycle life, simple principles, high dynamics of charge propagation, and low maintenance cost.<sup>119,120</sup> Supercapacitors store significantly higher amounts of energy density than the conventional capacitor, but they have a similar cell construction as traditional capacitors except for the fact that the metal electrodes are replaced by highly porous electrodes.<sup>121</sup> Furthermore, the shortage of other power sources, such as batteries and fuel cells, could be complemented by supercapacitors, because of their long cycle life and rapid charging and discharging rate at high power densities, as shown in Figure 1.5.

Depending on their energy storage mechanisms as well as electrode materials used, ECs can be divided into two categories: (i) electrical double-layer capacitors (EDLCs), in which the capacitance arises from a build-up field of electrostatic charges gathering at the interface between the electrode surface and the electrolyte (non-Faradaic charge storage). Thus, the surface area of the electrodes is a crucial factor for the capacitor. As a result, porous carbon materials with a large specific surface area (SSA) and mechanical properties have been frequently employed in electrode materials,<sup>122,123</sup> such as activated carbon,<sup>124</sup> xerogels,<sup>125</sup> CNTs,<sup>126</sup> carbon fibers (CFs, including carbon microfibers-CMFs and carbon nanofibers-CNFs),<sup>127</sup> graphene,<sup>128</sup> mesoporous carbon,<sup>129</sup> and carbide-derived carbon.<sup>130</sup> demonstrated that the

EDLCs can deliver rather high power densities, charge–discharge rates, and excellent cycling stabilities owing to a fast physical reversible adsorption/disadsorption of ions from the electrolyte onto the two porous electrodes (without any chemical reactions). However, their energy densities (typically ~5 Wh/kg) are often greatly limited by the electroactive surface area and the pore size distribution of carbon electrode materials.

Thus, to increase the energy densities, the second type of ECs come into being: (ii) pseudocapacitors based on a Faradic process, which involves fast and reversible redox reactions between the electrolyte and electroactive materials on the electrodes' surface.<sup>131</sup> The most widely explored electroactive materials include transition metal oxides (TMOs) or hydroxides such as RuO<sub>2</sub>, Fe<sub>3</sub>O<sub>4</sub>, NiO, MnO<sub>2</sub>, Co<sub>3</sub>O<sub>4</sub>, and Ni(OH)<sub>2</sub>,<sup>132,133</sup> conducting redox polymers (CRPs) such as polyaniline, polyurethane, polypyrrole, and polythiophene,<sup>134</sup> and other materials possessing oxygen/nitrogen surface functional groups.<sup>135</sup> Compared to EDLCs, pseudocapacitors can achieve much higher pseudo-capacitance and energy densities. However, for TMOs, their poor electrical conductivities (restricting fast electron transport) and intrinsic rigidity usually result in a low power density and poor flexibility. As for CRPs, their easily damaged structure during the redox process usually lead to a low cycling stability.

Hence, to resolve these problems, carbon-based materials with high electrical conductivity and large SSA are usually used as the backbone materials to combine with these active materials for pseudo-capacitor electrodes. Given the many excellent properties of graphene, such as high

electrical conductivity and high mechanical strength, graphene is considered as one of the most suitable substrate materials for preparing pseudocapacitor electrodes.

## 1.5 Objectives of this study

The very purpose of this thesis is to develop solution processable carbon nanomaterials for efficient and easy application of carbon-based nanomaterials since their unique structure and outstanding mechanical, electrical and thermal properties. For this purpose, two carbon nanomaterials, in particular CNT and graphene, were synthesized and functionalized for solution process.

First, MWCNTs is non-covalently functionalized for polymer/MWCNT composite. One of the most widely used approaches for effective dispersion of CNTs in polymer matrix is to modify the surface of CNTs by introducing functional groups covalently on the surface of CNTs. Although this approach is very effective to improve the compatibility between modified CNTs and matrix polymer, the introduction of covalent bonds inevitably disrupts the long range  $\pi$  conjugation of CNTs, leading to a detrimental effect on electrical and mechanical properties of the resulting polymer/CNT composites. Consequently, the non-covalent functionalization of CNTs by using compatibilizer has recently been developed by several research groups. Non-covalent functionalization avoids the destruction of the chemical structure of CNTs and thus improves the interfacial property between CNTs and polymer matrix without sacrifice of excellent mechanical and electrical properties of CNTs. Among various types of compatibilizer using non-covalent functionalization, block or graft copolymers have been used as effective compatibilizers for polymer/CNT composites.<sup>136,137</sup> If the main

chain in graft copolymer can interact with CNTs by  $\pi$ - $\pi$  interactions while the graft chain is miscible with matrix polymer, it is expected that CNTs are well dispersed in polymer matrix without sacrifice of excellent properties of CNTs.

With keeping this in mind, our group previously synthesized poly(3-hexylthiophene) (P3HT) grafted with designed polymers, where P3HT can interact non-covalently with CNTs and the designed polymer is miscible with the matrix polymer, and found that the compatibilizers were very effective to homogeneously disperse multi-walled carbon nanotubes (MWCNTs) in polymer matrix such as poly(styrene-co-acrylonitrile) (SAN),<sup>138</sup> polycarbonate,<sup>139</sup> and Nylon 66 (N66).<sup>140</sup> Although the P3HT main chain effectively interacts with MWCNTs, the use of those compatibilizers has several disadvantages: (i) high cost of 3-hexylthiophene, (ii) long reaction time for synthesis particularly due to removal of metal catalyst and (iii) difficulty to control the chain length of P3HT. Hence, for practical reasons it is demanded to synthesize cheaper and simpler compatibilizers which can interact non-covalently with both CNTs and matrix polymer.

To overcome these limitation, in this study, two graft-type compatibilizers containing naphthalene units, poly(vinyl benzyloxy ethyl naphthalate)-*g*-poly(methyl methacrylate) (PVBEN-*g*-PMMA) and poly(vinyl benzyloxy methyl naphthalene)-*g*-poly(*t*-butyl methacrylate-*co*-methacrylic acid) (PVBMN-*g*-P(*t*BMA-*co*-MAA)), are synthesized for SAN/MWCNT and N66/MWCNT composites, respectively. It has been known that naphthalene unit in the main chain of graft copolymer interacts

with the surface of MWCNTs by  $\pi$ - $\pi$  interaction and that PMMA and carboxylic acid group in the graft chain of two compatibilizers interacts with SAN and N66, respectively. Therefore, it is easily expected that (PVBEN-*g*-PMMA) and PVBMN-*g*-P(*t*BMA-*co*-MAA) can be used as an effective compatibilizer for dispersing MWCNTs in polymer matrices. The effectiveness of these new compatibilizers for SAN/MWCNT and N66/MWCNT composites is examined in terms of the dispersion of MWCNTs in polymer matrices and the mechanical and electrical properties of composites. Also, to investigate the effect of the number of carboxylic acid groups in the graft chain of compatibilizer on physical properties of N66/MWCNT composites, three PVBMN-*g*-P(*t*BMA-*co*-MAA)s with different number of carboxylic acids in the graft chain are synthesized and their effects on mechanical properties and electrical conductivity of composites are examined.

Second, GNRs were fabricated by bottom-up organic synthesis for semiconducting material of thin-film transistor. Graphene has remarkable electronic properties, i.e., extremely high charge carrier mobility, and the tunable charge carrier type and density. However, the fact that graphene is a zero-bandgap semi-metal limits its practical applications to high-performance TFTs. Although graphene itself is a zero-band-gap semi-metal, GNRs with a widths smaller than 10 nm exhibits semiconducting behavior that allows us to use them for active materials of electronic devices. Several methods have been reported to produce GNRs, such as reduction of graphite oxide, lithography, unzipping of CNTs, mechanical exfoliation and chemical

vapor deposition. However, the uncontrollable character of these methods or in some case the harsh conditions restrict severely the quality of the resulting GNRs and consequently limit their applications. Hence, a new synthetic strategy is strongly desired for well-defined GNRs.

Bottom-up organic synthesis of carbon nanomaterial is expected to control its structure on the atomic scale and thus enables chemists to reach their goal of synthesizing well-defined carbon nanomaterials. The fabrication of GNRs by organic synthesis has been attempted by a few research groups. Müllen and his co-workers originally synthesized GNRs by cyclodehydrogenation of polymer precursors and investigated their electronic properties.<sup>117,118</sup> However, they did not investigate the charge transport behavior of the GNRs. Ueda and his co-workers demonstrated the intramolecular oxidative coupling of poly(3-hexylthiophene)-*b*-poly(3-(4'-(3'',7''-dimethyloctoxy)phenyl)thiophene) (P3HT-*b*-P3PhT) to synthesize a block copolymer bearing polythiophene with graphene-like structure (P3HT-*b*-GPT) and investigated the charge transport behavior.<sup>141</sup> However, P3HT-*b*-GPT did not show an inherent property of graphene, because the GPT block length in P3HT-*b*-GPT was very short. Furthermore, the width of GNR in the block copolymer was very narrow, because they used phenylene as a precursor for GPT block.

Another advantage of the bottom-up approach is easy to control electronic properties of GNRs. One of the most feasible approaches to control the electronic properties of graphene is chemical doping by incorporation of heteroatoms (e.g., boron, nitrogen) into graphitic framework.

This method can not only alter the band structure but also generate specific charge carrier (hole or electron). For instance, nitrogen-doped graphene shows some unique properties including improved conductivity, excellent catalytic activity and n-type behavior. Although n-type semiconducting graphene is imperative for fabrication of complementary circuit, development of n-type semiconducting graphene is not satisfactory while a p-type graphene channel can be easily prepared under air and oxygen atmospheres. Nitrogen has been known as an effective atom for producing n-type semiconducting graphene channels by donating its lone pair electrons to the graphene network.

For synthesis of GNRs, the polymer precursors including phenylene, naphthalene and anthracene units first synthesized by the Suzuki coupling reaction between dibrominated monomer and diboronic ester monomer. The polymer precursors were then converted into the corresponding GNRs by the intramolecular cyclodehydrogenation reaction with  $\text{FeCl}_3$  as an oxidant. The cyclodehydrogenation were identified quantitatively by  $^1\text{H}$  nuclear magnetic resonance (NMR). The crystal structure and TFT characteristics of GNRs were analyzed as a function of the width of GNRs.

Also, in order to examine the effect of nitrogen doping on GNRs, nitrogen-doped graphene nanoribbons (GNR-Ns) with different amounts of nitrogen doping were synthesized by a bottom-up method. The degree of nitrogen doping was controlled by changing the monomer feed ratio of pyrazine to benzene. The the content of nitrogen in GNR-Ns were identified quantitatively by  $^1\text{H}$  NMR. The TFT characteristics of GNR-Ns were

investigated as a function of the amount of nitrogen doping in GNR-Ns.

Finally, graphene are directly exfoliated from graphite by water-soluble conducting polymer for supercapacitor electrode material. Due to their unique 2D structure and outstanding intrinsic physical properties, such as extraordinarily high electrical conductivity and large surface area, graphene-based materials exhibit great potential for application in supercapacitors. Compared with traditional electrode materials, graphene-based materials show some novel characteristics and mechanisms in the process of energy storage and release. Depending on their energy storage mechanisms as well as electrode materials used, ECs can be divided into two categories: (i) electrical double-layer capacitors (EDLCs), in which the capacitance arises from a build-up field of electrostatic charges gathering at the interface between the electrode surface and the electrolyte (non-Faradaic charge storage). Thus, the surface area of the electrodes is a crucial factor for the capacitor. However, their energy densities (typically  $\sim 5$  Wh/kg) are often greatly limited by the electroactive surface area and the pore size distribution of carbon electrode materials.

Thus, to increase the energy densities, the second type of supercapacitors come into being: (ii) pseudocapacitors based on a Faradic process, which involves fast and reversible redox reactions between the electrolyte and electroactive materials on the electrodes' surface. However, poor electrical conductivities (restricting fast electron transport) and intrinsic rigidity usually result in a low power density and poor flexibility. Also active materials were easily damaged structure by the redox reaction usually lead to

a low cycling stability.

Also, development the solution processable electrode material for high performance and various shape supercapacitor was highly demanded since supercapacitor application area expand from memory devices to electric vehicles. Hence, to develop the high performance and solution processable graphene-based supercapacitor electrode, carbon-based materials with high electrical conductivity and large SSA are usually used as the backbone materials to combine with these active materials for pseudo-capacitor electrodes. For this purpose, in this these, graphenes are directly exfoliated from graphite by polystyrenesulfonic acid-g-polyaniline (PSSA-g-PANI). The effectiveness of PSSA-g-PANI for direct exfoliation of graphene was evaluated by examining the quality of the dispersion of graphene in water. The capacitances of PSSA-g-PANI/graphene composites were examined with different ratio PANI to PSSA.

## Chapter 2. Experimental

### 2.1 Synthesis of compatibilizers

#### 2.1.1 Materials

All reagents were purchased from Sigma-Aldrich otherwise noted. 1-Naphthaleneethanol (95%), triethylamine (TEA) (99%), copper(I) bromide (CuBr) (99.999%), *N,N,N',N'',N''*-pentamethyldiethylenetriamine (PMDETA) (99%) and toluene (99.8%) were purchased and used as received.  $\alpha,\alpha'$ -Azobis(isobutyronitrile) (AIBN) (Junsei Chemical) was recrystallized in chloroform/ethanol solution prior to use. Potassium hydride (KH) and trifluoroacetic acid were purchased from Alfa Aesar and Acros Organics, respectively, and used as received. 4-Chloromethylstyrene (CMS) (90%), methyl methacrylate (MMA) (99.8%) and *t*-butyl methacrylate (*t*BMA) (98%) were purchased from Tokyo Chemical Industry and were washed with 5 % NaOH aqueous solution and subsequently with distilled water to remove stabilizers. Then, CMS, MMA and *t*BMA were dried by distillation over CaH<sub>2</sub>. Tetrahydrofuran (THF) (Daejung Chemicals & Metals) was dried by distillation over CaH<sub>2</sub>. MWCNTs (carbonaceous purity >95%, the diameter = 25–70 nm, the length = 1–5  $\mu$ m) and SAN ( $M_w$  = 130,000 g/mol, PDI = 2.23, the AN content = 24 wt%) were supplied from Cheil Industries and LG Chem, respectively, and were used as received, The chemical structure, <sup>1</sup>H

NMR spectrum and GPC trace of SAN were appeared in Figure 2.1. Nylon 66 (N66) was purchased from Solutia.

### **2.1.2 Synthesis of compatibilizer for SAN/MWCNT composite**

**Synthesis of poly(4-chloromethylstyrene) (PCMS):** PCMS was synthesized by free radical polymerization of CMS (15 mL, 0.165 mol) using AIBN (252 mg, 1.5 mmol) and THF (30 mL) as an initiator and solvent, respectively. After the solution was stirred at 90 °C for 24 h for polymerization, the solution was precipitated into excess methanol, and the precipitate (polymer) was collected by filtration and then washed with methanol. The product was dried at 30 °C under vacuum.

**Synthesis of Poly(4-chloromethylstyrene-*co*-vinyl benzyloxy ethyl naphthalene) (P(CMS-*co*-VBEN)):** P(CMS-*co*-VBEN) was synthesized by the substitution reaction. A part of chlorides in PCMS were substituted by 1-naphthaleneethanol (NE). KH (0.85 g, 0.021 mol) and NE (3.67 g, 0.021 mol) were dissolved in THF (10 mL), and the solution was cooled to 0 °C in an ice bath. A solution of TEA (2.97 mL) and PCMS (1 g) in THF (10 mL) was separately prepared and then added to the NE solution. The mixture solution was stirred for the substitution reaction at 40 °C for 24 h. The resulting solution was precipitated into methanol, and the product was collected by filtration and dried at vacuum oven.

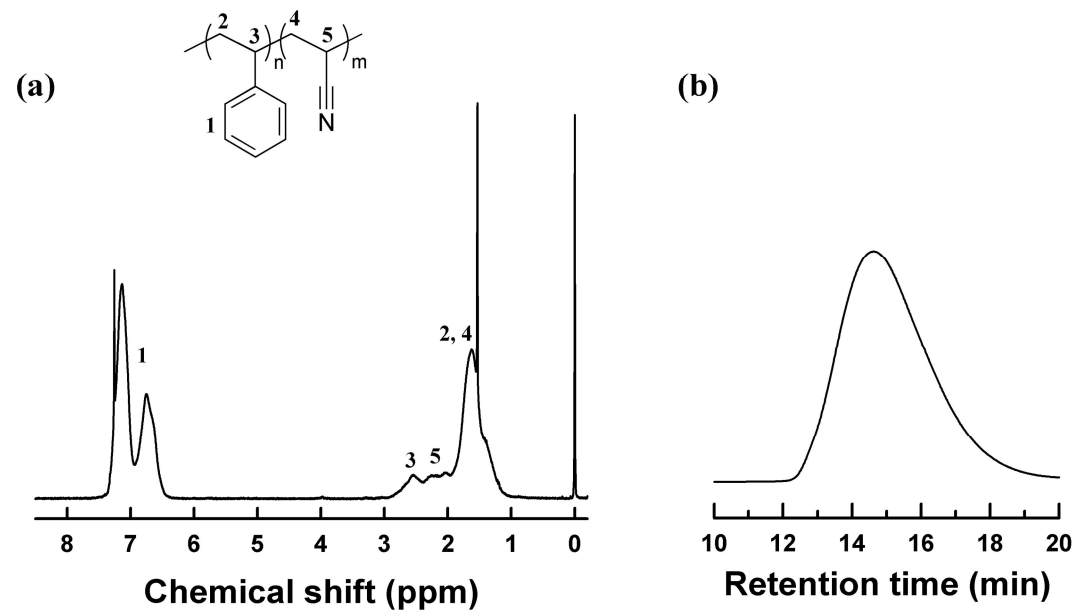


**Figure 2.1.** Chemical structure,  $^1\text{H}$  NMR spectrum (a) and GPC trace (b) of poly(styrene-*co*-acrylonitrile) (SAN)

**Synthesis of poly(vinyl benzyloxy ethyl naphthalate)-*g*-poly(methyl methacrylate) (PVBEN-*g*-PMMA):** PVBEN-*g*-PMMA was synthesized by the atom transfer radical polymerization of MMA using P(CMS-*co*-VBEN) as a macroinitiator. MMA (2.32 mL, 0.022 mol), PMDETA (0.027 mL, 0.13 mmol) were dissolved in 5 mL of toluene, and the mixture solution was degassed by three freeze-and-thaw cycles. After a solution of P(CMS-*co*-VBEN) (0.3 g) and CuBr (18.7 mg, 0.13 mmol) in toluene (10 mL) were added to the above solution, the reaction mixture was allowed to stir at 90 °C for 24 h. The reaction product was diluted with chloroform, and passed through a column Al<sub>2</sub>O<sub>3</sub> to remove CuBr. The resulting solution was concentrated and then precipitated into excess methanol. The product was collected by vacuum filtration and dried at 30 °C under vacuum.

### 2.1.3 Synthesis of compatibilizer for N66/MWCNT composite

**Synthesis of poly(4-chloromethylstyrene) (PCMS):** PCMS was synthesized by free radical polymerization of CMS using AIBN and THF as an initiator and solvent, respectively. After the solution was stirred at 90 °C for 24 h for polymerization, the solution was precipitated into excess methanol, and the precipitate (polymer) was collected by filtration and then washed with methanol. The product was dried at 30 °C under vacuum.

**Synthesis of Poly(vinyl benzyloxy methyl naphthalene)-*g*-poly(*t*-butyl methacrylate) (PVBMN-*g*-PtBMA):** PVBMN-*g*-PtBMA was synthesized

by the substitution reaction, where most of chlorides in PCMS were substituted by 1-naphthalenemethanol (NM). KH and NM were dissolved in THF before the solution was cooled to 0 °C in an ice bath. A solution of TEA and PCMS in THF was separately prepared and then added to the NM solution. The reaction mixture was stirred for the substitution reaction at 40 °C for 24 h. The resulting solution was precipitated into methanol, and the product was collected by filtration and dried in a vacuum oven.

**Synthesis of Poly(vinyl benzyloxy methyl naphthalene)-g-poly(*t*-butyl methacrylate) (PVBMN-*g*-P*t*BMA):** PVBMN-*g*-P*t*BMA was synthesized by ATRP of *t*BMA using P(CMS-*co*-VBMN) as a macroinitiator. *t*BMA and PMDETA were dissolved in toluene, and the solution was degassed by three freeze-and-thaw cycles. A solution of P(CMS-*co*-VBMN) and CuBr in toluene was separately prepared and added to the *t*BMA/PMDETA solution. The reaction mixture was then stirred for ATRP at 90 °C for 24 h. The reaction product was diluted with chloroform, and passed through a column Al<sub>2</sub>O<sub>3</sub> to remove CuBr. The resulting solution was concentrated and then precipitated into excess methanol. The product was collected by vacuum filtration and dried at 30 °C under vacuum.

**Synthesis of Poly(vinyl benzyloxy methyl naphthalene)-g-poly(*t*-butyl methacrylate-*co*-metacrylic acid) (PVBMN-*g*-P(*t*BMA-*co*-MAA)):** PVBMN-*g*-P*t*BMA was partially hydrolyzed by trifluoroacetic acid to produce PVBMN-*g*-P(*t*BMA-*co*-MAA). PVBMN-*g*-P*t*BMA was dissolved in

THF at room temperature. As the solution was cooled to 0 °C in an ice bath, trifluoroacetic acid for hydrolysis of *t*-butyl methacrylate unit was dropwise added into the solution. The reaction mixture was stirred at 50 °C for 3 h and subsequently at 0 °C for 2 h under vacuum. The solution was precipitated into hexane to collect the final product. The collected precipitate was washed several times with hexane, and then dried at 30 °C under vacuum.

#### **2.1.4 Preparation of composite films**

All of polymer/MWCNT composites with different loadings of MWCNTs were prepared by the solution blending. A typical procedure of SAN/MWCNT/compatibilizer composite with 1 wt % of MWCNTs is as follows: A dispersed solution of 5 mg of compatibilizer and 5 mg of MWCNTs in 10 mL of chloroform was sonicated for 1 h. The dispersed solution was mixed with a solution containing 500 mg of SAN in 10 mL of chloroform. The mixture was sonicated for an additional 20 min and then precipitated in excess methanol. The precipitate was collected by filtration and washed with methanol. The filter cake (SAN/MWCNT/compatibilizer composite) was dried at 30 °C under vacuum for 24 h.

Films of SAN/MWCNT/compatibilizer composites were prepared by solution casting: A solution of SAN/MWCNT/compatibilizer in chloroform was poured onto a glass plate and then a doctor blade was used to prepare a solution film. The solvent was slowly evaporated at room temperature and the resulting film was thoroughly dried under high vacuum at 30 °C for 24 h. The

other film of polymer/MWCNT composites were also prepared by the same procedure.

## 2.2 Synthesis of GNRs

### 2.2.1 Materials

All starting materials were purchased from Sigma-Aldrich and Tokyo Chemical Industry and used as received without further purification. Dichloromethane (Daejung) was dried over calcium hydride, and freshly distilled prior to use. Anhydrous toluene, dimethylformamide, 1,4-dioxane, 1,4-benzenediboronic acid bis(pinacol) ester were purchased from Sigma-Aldrich, and used as received.

### 2.2.2 Synthesis of GNRs

**Synthesis of 1,2-dibromo-4,5-bis-hexyloxy-benzene and 1,2-dibromo-4,5-bis-dodecyloxy-benzene:** After 4,5-dibromo-1,2-benzenediol (2 g, 7.47 mmol) and potassium carbonate ( $K_2CO_3$ ) (2.06, 14.93 mmol) were dissolved in anhydrous dimethylformamide (30 mL), the solution was stirred at 90 °C for 4 h. 1-Bromohexane (1.6 mL, 11.20 mmol) was added to the mixed solution, and the solution was stirred at 90 °C for 24 h. The reaction mixture was quenched by adding water and then extracted with diethyl ether. After the organic phase was dried over magnesium sulfate ( $MgSO_4$ ), the solvent was evaporated under reduced pressure. The crude product was purified by column chromatography on silica gel (1:10 ethyl acetate/hexane as eluent) to afford the 1,2-dibromo-4,5-bis-hexyloxy-benzene as a colorless liquid (95%).  $^1H$  NMR (300 MHz,  $CDCl_3$ ):  $\delta$  (ppm) 0.90 (t, 6H), 1.45 (m, 8H), 1.55 (m,

4H), 1.79 (m, 4H), 3.94 (t, 4H), 7.06 (s, 2H).  $^{13}\text{C}$  NMR (125 MHz,  $\text{CDCl}_3$ ):  $\delta$  (ppm) 13.91, 22.51, 25.56, 29.01, 31.45, 69.60, 114.65, 118.10, 149.07.  $m/z$  (MS-EI) calcd: 436.0, found: 436. 1,2-Dibromo-4,5-bis-dodecyloxy-benzene was also synthesized using 1-bromo dodecane by the same procedure as 1,2-dibromo-4,5-bis-hexyloxy-benzene (93%).  $^1\text{H}$  NMR (300 MHz,  $\text{CDCl}_3$ ):  $\delta$  (ppm) 0.88 (t, 6H), 1.26 (m, 32H), 1.46 (m, 4H), 1.82 (m, 4H), 3.94 (t, 4H), 7.02 (s, 2H).  $^{13}\text{C}$  NMR (125 MHz,  $\text{CDCl}_3$ ):  $\delta$  (ppm) 13.98, 22.97, 23.85, 29.03, 30.49, 39.44, 71.86, 114.42, 117.72, 149.40.  $m/z$  (MS-EI) calcd: 604.2, found: 604.

**Synthesis of 2,6-bis(4,4,5,5-tetramethyl-1,3,2-dioxabrolan-2-yl)-naphthalene:** 2,6-Dibromo-naphthalene (2.73 g, 9.5 mmol), bis(pinacolato) diboron (5.34 g, 21.0 mmol),  $\text{PdCl}_2(\text{dppf})$  (0.72 g, 0.97 mmol), and potassium acetate (KOAc, 55.94 mmol) (5.49 g) were dissolved in anhydrous 1,4-dioxane (40 mL). The mixture was stirred at room temperature for 30 min before it was stirred at 80 °C for 20 h. The resulting mixture was then quenched by adding water and extracted with diethyl ether. After the organic extract was dried over  $\text{MgSO}_4$  and filtered, the solvent was evaporated under reduced pressure. The crude product was purified by silica gel chromatography by using 3% ethylacetate in hexane as an eluent to afford 2,6-bis(4,4,5,5-tetramethyl-1,3,2-dioxabrolan-2-yl)-naphthalene as a white solid (72%).  $^1\text{H}$  NMR (300 MHz,  $\text{CDCl}_3$ ):  $\delta$  (ppm) 1.39 (s, 24H), 7.84-7.85 (dd, 4H), 8.35 (s, 2H).  $^{13}\text{C}$  NMR (125 MHz,  $\text{CDCl}_3$ ):  $\delta$  (ppm) 24.92, 83.95, 127.67, 130.35, 134.34, 135.99.  $m/z$  (MS-EI) calcd: 380.2, found: 380.

**Synthesis of 2,6-bis(4,4,5,5-tetramethyl-1,3,2-dioxabrolan-2-yl)-anthracene:** 2,6-Dibromo-anthracene was synthesized by following the method reported in the literature.<sup>142,143</sup> The 2,6-bis(4,4,5,5-tetramethyl-1,3,2-dioxabrolan-2-yl)-anthracene was synthesized from 2,6-dibromo-anthracene by the same procedure as 2,6-bis(4,4,5,5-tetramethyl-1,3,2-dioxabrolan-2-yl)-naphthalene (69%). <sup>1</sup>H NMR (300 MHz, CDCl<sub>3</sub>):  $\delta$  (ppm) 1.39 (s, 24H), 7.69 (d, 2H), 8.21 (t, 4H), 8.61 (s, 2H). <sup>13</sup>C NMR (125 MHz, CDCl<sub>3</sub>):  $\delta$  (ppm) 24.92, 83.95, 126.17, 127.87, 129.95, 132.33, 133.34, 136.64. m/z (MS-EI) calcd: 430.2, found: 430.

**Polymerization:** A mixture of dibrominated monomer (1.15 mmol) and diboronic ester monomer (1.15 mmol), K<sub>2</sub>CO<sub>3</sub> (2 M/H<sub>2</sub>O, 11.5 mmol) and Aliquat 336 (5 drops) in toluene (12 mL) was flushed with an argon stream for 20 min. Pd(PPh<sub>3</sub>)<sub>4</sub> (0.0575 mmol) was added quickly in the reaction mixture and sealed. The mixture solution was heated to 140 °C in a microwave reactor with 400W for 10 h. The organic phase was then poured into a methanol (200 mL) and stirred. The precipitate was filtered through a Soxhlet thimble and subjected to Soxhlet extraction sequentially with methanol, hexane, acetone and chloroform. The polymer was recovered from the chloroform fraction by evaporating the solvent. Phenylene-based polymer (Poly-Ph): yield: 76%, M<sub>n</sub> = 16,100 g/mol, PDI = 1.36; <sup>1</sup>H NMR (300 MHz, CDCl<sub>3</sub>):  $\delta$  (ppm) 0.91 (br, 6H), 1.31 (br, 12H), 1.83 (br, 4H), 4.04 (br, 4H), 6.95 (br, 6H). Naphthalenebased polymer (Poly-Np): yield: 75%, M<sub>n</sub> = 14,300 g/mol, PDI = 1.33; <sup>1</sup>H NMR (300 MHz, CDCl<sub>3</sub>):  $\delta$  (ppm) 0.91 (br, 6H), 1.31

(br, 12H), 1.83 (br, 4H), 4.07 (br, 4H), 7.03 (br, 4H), 7.42 (br, 2H), 7.69 (br, 2H). Anthracene-based polymer (Poly-An): yield: 75%,  $M_n = 13,100$  g/mol, PDI = 1.41;  $^1\text{H}$  NMR (300 MHz,  $\text{CDCl}_3$ ):  $\delta$  (ppm) 0.91 (br, 6H), 1.31 (br, 36H), 1.83 (br, 4H), 4.10 (br, 4H), 7.03 (br, 4H), 7.67 (br, 2H), 8.11 (br, 2H), 8.43 (br, 2H).

**Cyclodehydrogenation:** 200 mg of precursor polymer was dissolved in 300 mL anhydrous dichloromethane to which a solution of 5 equiv.  $\text{FeCl}_3$  in nitromethane was added dropwise. The mixture solution was then stirred at 30 °C for 3 days. The solution was concentrated under reduced pressure, and the concentrated solution was precipitated into methanol (400 mL) to collect the final product (GNR). The precipitate was filtered through a Soxhlet thimble, and subjected to Soxhlet extraction with methanol, hexane, acetone and chloroform. The product was recovered from the chloroform fraction by evaporating the solvent. Phenylene-based GNR (GNR-Ph): yield: 83%,  $M_n = 18,500$  g/mol, PDI = 1.40. Naphthalene-based GNR (GNR-Np): yield: 42%,  $M_n = 17,800$  g/mol, PDI = 1.32. Anthracene-based GNR (GNR-An): yield: 20%,  $M_n = 17,300$  g/mol, PDI = 1.35.

### 2.2.3 Synthesis of GNR-Ns

**Synthesis of 2,3-bis-dodecyloxy-pyrazine:** In a dried 150 mL round bottom flask, 20 mL of DMF was added to a mixture of 2,3-dichloropyrazine (2 g,

13.42 mmol), 1-dodecanol (7.5 g, 40.27 mmol),  $K_2CO_3$  (3.72 g, 26.92 mmol) and benzyltriethylammonium chloride (BTEAC) (0.4 g, 1.76 mmol) and the solution was stirred at 90 °C for 24 h. The mixture was poured into 100 mL of water and the organic phase was extracted with diethyl ether and washed with brine. After the organic phase was dried over  $MgSO_4$ , the solvent was evaporated under reduced pressure. The crude product was purified by column chromatography on silica gel (1:9 ethyl acetate/hexane as eluent) to afford 2,3-bis-dodecyloxy-pyrazine as a white solid (90%).  $^1H$  NMR (300 MHz,  $CDCl_3$ ):  $\delta$  (ppm) 0.88 (t, 6H), 1.26 (m, 36H), 1.82 (m, 4H), 4.35 (t, 4H), 7.56 (s, 2H).  $m/z$  (MS-EI) calcd: 448.4, found: 448.

**Synthesis of 2,3-Dibromo-5,6-bis-dodecyloxy-pyrazine.** A mixture of 2,3-bis-dodecyloxy-pyrazine (2 g, 4.46 mmol) and sodium acetate (NaOAc) (1 g, 12.19 mmol) and acetic acid (80 mL) was heated to reflux with stirring. Bromine (2.85 g, 17.82 mmol) was added dropwise to the mixture, followed by stirring for 12 h. After the mixture was cooled, the reaction mixture was quenched by adding water (200 mL) and then extracted with diethyl ether. After the organic phase was dried over  $MgSO_4$ , the solvent was evaporated under reduced pressure. The crude product was purified by column chromatography on silica gel (3:7 ethyl acetate/hexane as eluent) to afford the compound 3 as a yellowish solid (35%).  $^1H$  NMR (300 MHz,  $CDCl_3$ ):  $\delta$  (ppm) 0.88 (t, 6H), 1.26 (m, 36H), 1.82 (m, 4H), 3.40 (t, 4H).  $m/z$  (MS-EI) calcd: 606.22, found: 606.

**Synthesis of 2,6-bis(4,4,5,5-tetramethyl-1,3,2-dioxabrolan-2-yl)-naphthalene:** 2,6-Dibromo-naphthalene (2.73 g, 9.5 mmol), bis(pinacolato)diboron (5.34 g, 21.0 mmol), PdCl<sub>2</sub>(dppf) (0.72 g, 0.97 mmol), and potassium acetate (KOAc) (5.49 g, 55.94 mmol) were dissolved in anhydrous 1,4-dioxane (40 mL). The mixture was stirred at room temperature for 30 min before it was stirred at 80 °C for 20 h. The resulting mixture was then quenched by adding water and extracted with diethyl ether. After the organic extract was dried over MgSO<sub>4</sub> and filtered, the solvent was evaporated under reduced pressure. The crude product was purified by silica gel chromatography by using 3% ethylacetate in hexane as an eluent to afford the compound 4 as a white solid (72%). <sup>1</sup>H NMR (300 MHz, CDCl<sub>3</sub>): δ (ppm) 1.39 (s, 24H), 7.84–7.85 (dd, 4H), 8.35 (s, 2H). <sup>13</sup>C NMR (125 MHz, CDCl<sub>3</sub>): δ (ppm) 24.92, 83.95, 127.67, 130.35, 134.34, 135.99. m/z (MS-EI) calcd: 380.2, found: 380.

**Polymerization:** After a mixture of dibrominated monomer (1.15 mmol) and diboronic ester monomer (1.15 mmol), K<sub>2</sub>CO<sub>3</sub> (2 M/H<sub>2</sub>O, 11.5 mmol) and Aliquat 336 (5 drops) in toluene (12 mL) was flushed with an argon stream for 20 min, Pd(PPh<sub>3</sub>)<sub>4</sub> (0.0575 mmol) was added quickly in the reaction mixture and sealed. The mixture solution was heated to 140 °C in a microwave reactor with 400 W for 16 h. The organic phase was then poured into a methanol (200 mL) and stirred. The precipitate was filtered through a Soxhlet thimble and subjected to Soxhlet extraction sequentially with methanol, hexane, acetone and chloroform. The polymer was recovered from

the chloroform fraction by evaporating the solvent. Benzene-based polymer (Poly-N0), yield: 76%,  $M_n=15100$  g/mol, PDI=1.36; benzene and pyrazene-based polymer (Poly-N50), yield: 42%,  $M_n=14400$  g/mol, PDI=1.33; pyrazine-based polymer (Poly-N100), yield: 38%,  $M_n=14700$  g/mol, PDI=1.41.

**Cyclodehydrogenation:** 200 mg of precursor polymer was dissolved in 300 mL anhydrous dichloromethane to which a solution of 10 eq  $FeCl_3$  in nitromethane was added dropwise. The mixture solution was then stirred at 40 °C for 3 days. The solution was concentrated under reduced pressure, and the concentrated solution was precipitated into methanol (400 mL) to collect the final product (GNR). The precipitate was filtered through a Soxhlet thimble, and subjected to Soxhlet extraction with methanol, hexane, acetone and chloroform. The product was recovered from the chloroform fraction by evaporating the solvent. Benzene-based GNR (GNR-N0), yield: 76%,  $M_n=16800$  g/mol, PDI=1.56; benzene and pyrazene-based GNR (GNR-N50), yield: 75%,  $M_n=16000$  g/mol, PDI=1.47; pyrazine-based GNR (GNR-N100), yield: 75%,  $M_n=16100$  g/mol, PDI=1.49.

#### 2.2.4 TFT fabrication

For measurement of charge transport properties of synthesized GNRs, TFTs with the configuration of bottom-gate and bottom-contact device were

fabricated using heavily n-doped conductive silicon wafer with a SiO<sub>2</sub> layer. The silicon wafer and the SiO<sub>2</sub> layer were used as the gate electrode and the gate dielectric (capacitance  $C_i = 10.8 \times 10^{-9} \text{ F}\cdot\text{cm}^{-2}$ ), respectively. The substrates were cleaned by stepwise sonication in acetone and isopropyl alcohol, followed by O<sub>2</sub> plasma treatment for 10 min. The SiO<sub>2</sub> dielectric was treated with HMDS prior to deposition of GNRs both to passivate the SiO<sub>2</sub> surface and to enhance the ordering of the GNRs at the dielectric interface. The GNRs were dissolved in anhydrous o-DCB (20 mg/mL), and spin-coated on the top of the HMDS layer at 1000 rpm for 60 s. The resulting films were dried at 190 °C for 10 min on a hot plate under nitrogen atmosphere inside the glove box. The top-contact source and drain electrodes were defined by a 50 nm thick Au layer through a shadow mask, and the channel length ( $L$ ) and width ( $W$ ) were 200 and 1500  $\mu\text{m}$ , respectively.

## **2.3 Preparation of PSSA-g-PANI/graphene composites**

The chemical structure of water soluble conducting polymer, polystyrene sulfonic acid-g-polyaniline (PSSA-g-PANI), for exfoliation of graphene from graphite is represented in Figure 2.2. PSSA-g-PANI was synthesized by following the method reported in the literature.<sup>144</sup> A typical fabrication procedure of PSSA-g-PANI/graphene composite is as follows: A solution of 200 mg of graphite and 50 mg of PSSA-g-PANI in 12.5 mL of ethanol was sonicated for 10 h. The dispersed solution was centrifugated at 2000 rpm for 1 h and the PSSA-g-PANI/graphene composite was obtained by evaporation of solvent in supernatant. The filter cake (PSSA-g-PANI/graphene composite) was dried at 30 °C under vacuum for 24 h.

## 2.4 Measurements

### 2.4.1 Characterization methods

The chemical structure of the synthesized materials was identified by a Bruker Avance (referenced to  $\text{CDCl}_3$ :  $^1\text{H}$  NMR at 300 MHz and  $^{13}\text{C}$  NMR at 100 MHz). The conversion of *t*-butyl group into carboxylic acid group and the interaction between N66 and compatibilizer were identified by a Fourier transform infrared spectrometer (FT-IR, JASCO FT/IR-660 plus). Molar masses of compounds were measured by mass spectroscopy (Jeol JMS600w) in electron-impact mode. Molecular weight of polymer and its distribution were measured by gel permeation chromatography (GPC) (Waters).

The optical absorption and fluorescence emission spectra were obtained by a UV-Vis spectrophotometer (Lambda 25, Perkin Elmer) and a fluorescence spectrometer (QM-4, Photon Technology International) at excitation wavelength of 270 nm, respectively. Raman spectra were obtained on the film sample using a Raman spectrometer (T64000, HORIABA Jobin Yvon and HR 800, LAMRAM) with Ar laser at excitation wavelength of 514 nm. Thermogravimetry analyses were carried out with a DuPont TGA 2590 at a heating rate of 10 °C/min under a nitrogen atmosphere. The thermal transition temperatures of GNRs were determined by a differential scanning calorimeter (DSC) (DSC 2920, TA instrument). An X-ray diffraction (XRD) pattern was obtained from an X-ray diffractometer (M18XHF-SRA, McScience) using Cu-K $\alpha$  radiation ( $\alpha=1.5418 \text{ \AA}$ ) at a scan rate of  $2^\circ \text{ min}^{-1}$ .

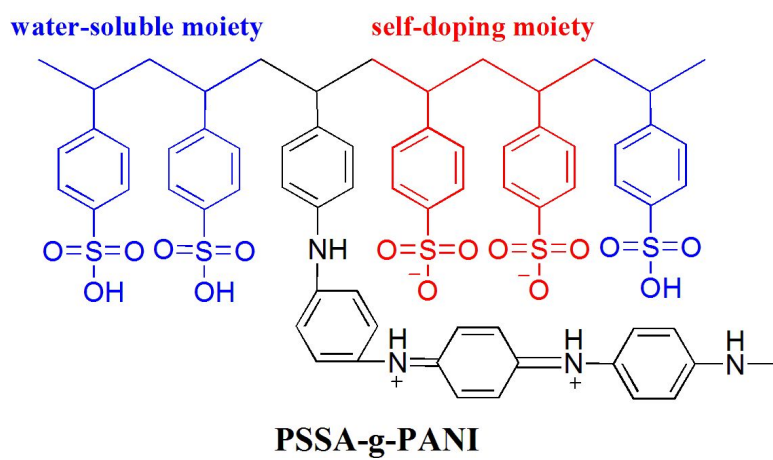


**Figure 2.2.** Chemical structure of PSSA-g-PANI.

## 2.4.2 Composite properties measurements

The morphologies of composite films were observed for examination of the dispersion of MWCNTs in composites using a transmission electron microscopy (TEM, JEM-1010, JEOL). The tensile properties of composite films were measured with a universal testing machine (Instron-5543, Instron) with a 1 kN load cell at a constant cross-head speed of 3mm/min. At least five specimens were tested for each sample, and the tensile properties are reported on average.

The resistivity of composite films was measured using a four-point probe system (CRESBOX, Napson) and converted to the electrical conductivity ( $\sigma$ ) using the relation,  $\sigma = 1/tR$ , where  $t$  and  $R$  are the thickness and the resistivity of sample films, respectively. The thickness of sample films was 0.12–0.15 mm. At least ten specimens were tested for each sample, and the average values are reported.

## 2.4.3 TFT performance measurement

Output and transfer characteristics of the devices were measured at room temperature in a  $N_2$ -atmosphere glove box by Keithley 4200 and MST5000A. The drain-source voltage for transfer characteristics was  $-60$  V and the field effect mobility ( $\mu$ ) was measured from the transfer curve in the saturation regime and estimated by the following equation:

$$I_{DS} = \frac{W\mu C_i}{2L} (V_G - V_T)^2$$

where  $I_{DS}$  is the source-drain current,  $C_i$  is the capacitance of gate dielectric layer, and  $V_T$  is the threshold voltage.

#### 2.4.4 Electrochemical measurement

The electrochemical properties of supercapacitor electrodes were measured in three-electrode system by cyclic voltammetry (CV) using a potentiostat/galvanostat (VMP 3, Biologic) from 0 to 0.8 V in an electrolyte solution of 0.1 M tetrabutylammonium hexafluorophosphate in acetonitrile. PSSA-g-PANI/ graphene composite, Pt wire and Ag/AgCl were used as the working electrode, counter electrode and reference electrode, respectively. The working electrode was fabricated by drop casting of PSSA-g-PANI/graphene in ethanol solution onto Pt rod and then dried in an air atmosphere. The CV was carried out at different scan rates ranging from 10 to 100 mV/s. The specific capacitance,  $C$  (F/g), was calculated from each cyclic voltammogram according to

$$C = \frac{A}{V f m}$$

where  $A$  is the area of cyclic voltammogram,  $V$  is working voltage range,  $f$  is scan rate, and  $m$  is mass of electrode material.

## Chapter 3. Results and Discussion

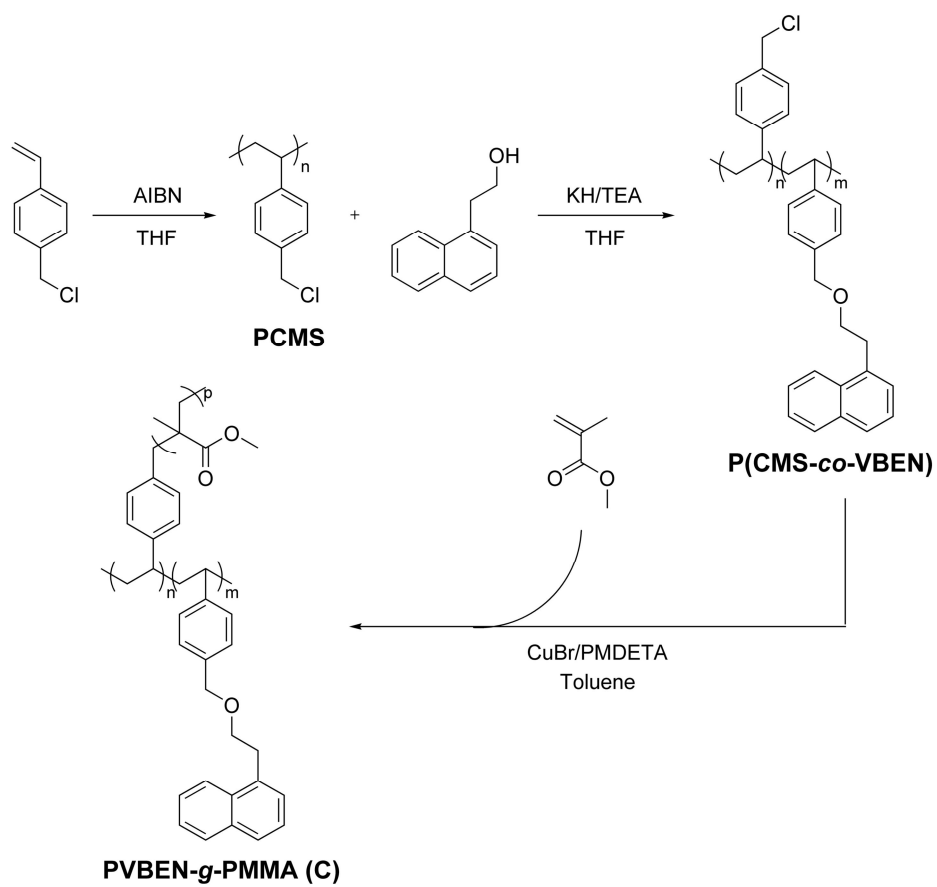
### 3.1 SAN/compatibilizer/MWCNT composites

#### 3.1.1 Synthesis and characterization

The overall synthesis route of PVBEN-*g*-PMMA (**C**) is represented in Scheme 3.1. The chemical structures of P(CMS-*co*-VBEN) and PVBEN-*g*-PMMA (**C**) are identified by <sup>1</sup>H NMR, as shown in Figure 3.1. The molecular weights and the polydispersity indices as measured by gel permeation chromatography are shown in Figure 3.2 and Table 3.1. The molar ratio of CMS to VBEN in **C** is 9 as determined by <sup>1</sup>H NMR (Figure 3.2(a)), indicating that an initiating site for ATRP is located at every 10 units of VBEN in the P(CMS-*co*-VBEN). Note that the unsubstituted CMS unit provides an initiating site for ATRP. Examination of the <sup>1</sup>H NMR spectrum of **C** (Figure 3.1(b)) reveals that the average degree of polymerization of PMMA in **C** is about 85.

#### 3.1.2 Identification of interaction

A specific interaction between compatibilizer and MWCNTs is one of the most important requirements for an effective compatibilizer. In order to examine the interaction, the  $\pi$ - $\pi$  interaction between naphthalene units of **C**



**Scheme 3.1.** The overall synthesis route of the compatibilizer, PVBEN-g-PMMA.

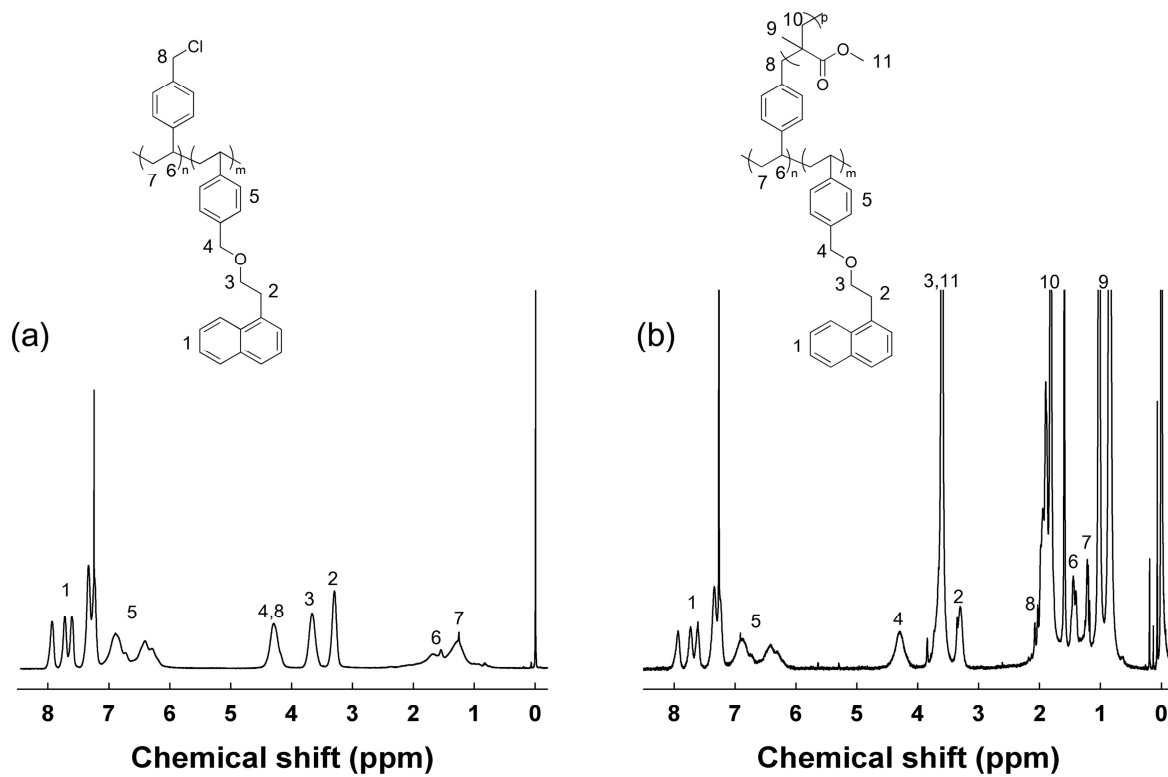


**Figure 3.1.** Chemical structures and  $^1\text{H}$  NMR spectra of  $\text{P}(\text{CMS-co-VBEN})$  (a) and  $\text{PVBEN-g-PMMA}$  (b).



and MWCNTs was evaluated by measuring the fluorescence quenching efficiency of MWCNTs. Figure 3.3(a) compares the fluorescence emission spectra of SAN/C and SAN/MWCNT/C in chloroform solution, where the emission spectra were obtained by irradiating at 270 nm corresponding to the absorption wavelength of naphthalene. The SAN/C exhibits strong fluorescence, as shown in Figure 3.3(a), whereas the fluorescence emitted from naphthalene is completely quenched in SANMWCNT/C in chloroform due to an effective energy transfer between naphthalene of C and MWCNTs,<sup>145,146</sup> indicating that there is strong  $\pi$ - $\pi$  interaction between MWCNTs and naphthalenes of C in solution. When the fluorescence emission spectrum of SAN/C in solid film is compared with that of SAN/MWCNT/C film, as shown in Figure 3.3(b), it is also observed that the strong fluorescence emission of SAN/C film is nearly quenched in SAN/MWCNT/C film, indicating that the strong  $\pi$ - $\pi$  interaction between naphthalene of C and MWCNTs is also available in solid state.

Also, the  $\pi$ - $\pi$  interaction between them is verified by Raman spectra, as shown in Figure 3.4. The peaks at around 1340 and 1580  $\text{cm}^{-1}$  correspond to the disorder-induced D-band and the tangential G-band of MWCNT, respectively. The G-band of MWCNT in SAN/MWCNT/C slightly shifts to higher wavenumber ( $\sim 7 \text{ cm}^{-1}$ ) as compared to that of pristine MWCNT, whereas the G-band of MWCNT in SAN/MWCNT remains unchanged. Since the strong attachment of polymer onto the surface of CNTs leads the shift of G-band toward higher frequency due to an increase in the elastic constant of the polymer-coated CNTs,<sup>147</sup> the upper shift of the G-band in

SAN/MWCNT/C is attributed to the  $\pi$ - $\pi$  interaction between MWCNTs and naphthalene of C.

For the compatibilizer C to be effective, it is required that the PMMA graft in C is miscible with the SAN matrix. To verify the miscibility between SAN and PMMA, the glass transition temperatures ( $T_g$ ) of C, SAN, and SAN/MWCNT/C are measured by DSC. As can be seen in Figure 3.5, a single  $T_g$  of SAN/MWCNT/C is observed at 120 °C instead of two  $T_g$ 's corresponding to  $T_g$ s of SAN and C, indicating that PMMA graft of C is miscible with SAN matrix. Also, the MWCNTs in SAN/MWCNT composite using P(CMS-*co*-VBEN) without PMMA graft chain are not dispersed in SAN matrix (Figure 3.6). From the results of fluorescence emission, DSC thermogram and FE-SEM images, it is concluded that the compatibilizer (C) synthesized in this study can play a role as an effective compatibilizer for SAN/MWCNT composites.

### **3.1.3 Dispersity of MWCNTs in SAN matrix**

Since pristine MWCNTs are aggregated by inter-tube interaction in polymer matrix, the homogeneous dispersion of MWCNTs in SAN matrix is a prerequisite for MWCNTs to effectively reinforce the SAN matrix. The dispersion state of MWCNTs in SAN/MWCNT and SAN/MWCNT/C composites is investigated by TEM. From the results of thermal gravimetric analysis, the content of MWCNT after film formation is nearly same with feed amount (see Figure 3.7). When TEM images of the composites (SAN/

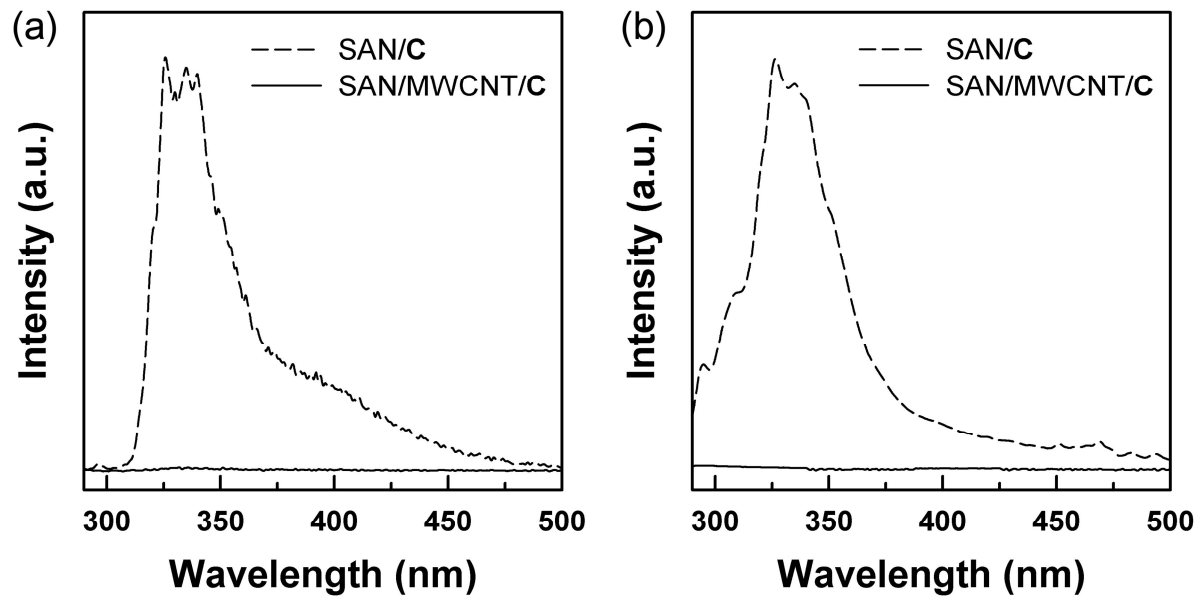


**Figure 3.3.** Fluorescence emission spectra of compatibilizer in chloroform solution (a) and in film (b).

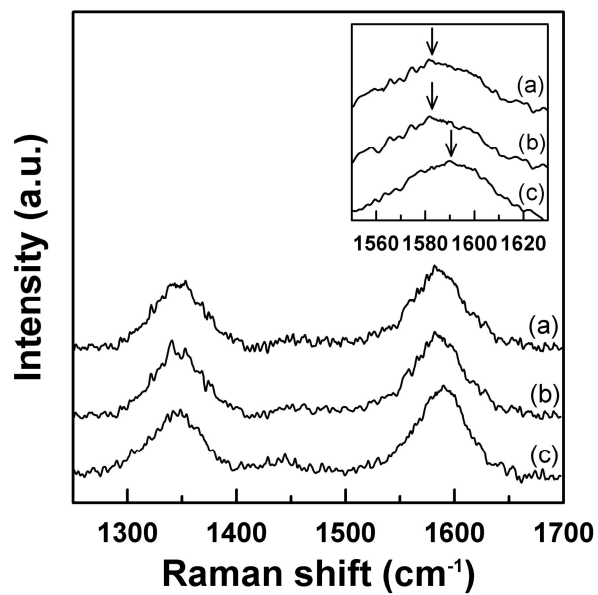


**Figure 3.4.** Raman spectra of the MWCNT (a), SAN/MWCNT (b), and SAN/MWCNT/C (c) with 1 wt.% MWCNTs.

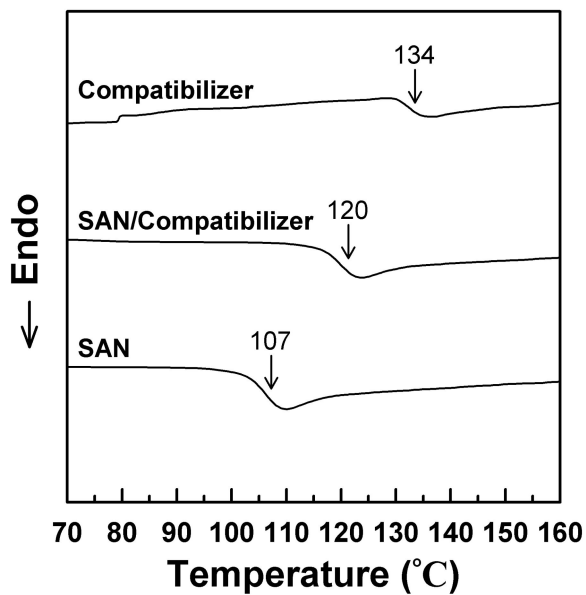


**Figure 3.5.** DSC thermograms of compatibilizer, SAN, SAN/compatibilizer with 10 wt.% compatibilizer

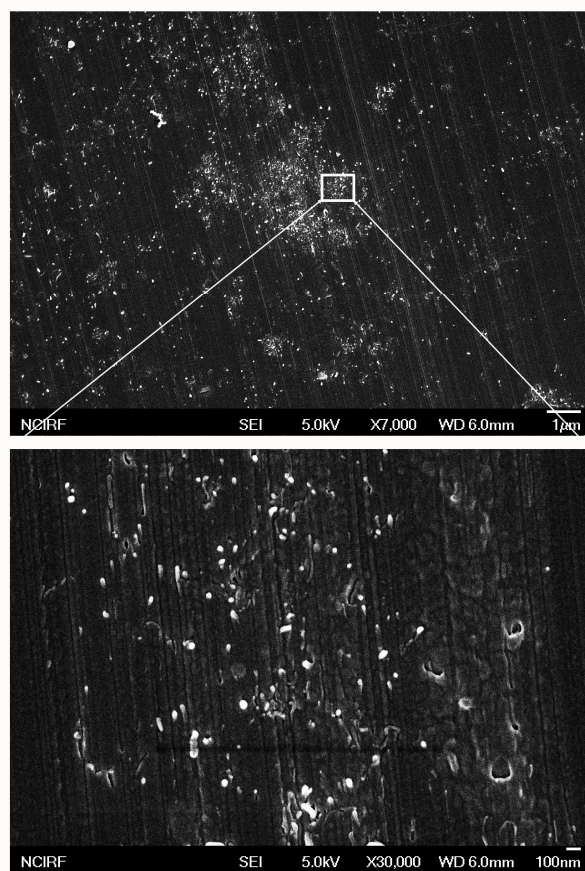


**Figure 3.6.** FE-SEM images of SAN/MWCNT composite using P(CMS-*co*-VBEN) without PMMA graft chain. The content of MWCNTs is 1 wt.%.

MWCNT) without compatibilizer are compared with those of composites (SAN/MWCNT/C) with compatibilizer, as shown in Figure 3.8, it is obvious that SAN/MWCNT exhibits severe aggregation of MWCNTs in the SAN matrix while MWCNTs functionalized with C are homogeneously dispersed in the SAN matrix, indicating that the compatibilizer C effectively disperses MWCNTs in the SAN matrix by reducing the interfacial tension between SAN and MWCNTs. Also, this result is identified by FE-SEM images, as shown in Figure 3.9.

### **3.1.4 Tensile properties of composites**

Figure 3.10 shows the representative stress-strain curves of neat SAN, SAN/MWCNT, and SAN/MWCNT/C with 0.5 wt.% loading of MWCNTs, and the tensile properties of neat SAN, SAN/MWCNT, and SAN/MWCNT/C are plotted as a function of the MWCNT loading in Figure 3.11. When the tensile properties of SAN/MWCNT composites are compared with those of the neat SAN, it is realized that the Young's modulus is increased until 1 wt.% addition of MWCNTs while both the tensile strength and the elongation at break are decreased considerably as compared with those of the neat SAN, as shown in Figure 3.10. This negative behavior is attributed to poor dispersion of MWCNTs in SAN matrix, as shown in Figure 3.8, and weak interfacial adhesion between SAN and MWCNTs. However, when a small amount (0.5 wt.%) of the compatibilizer C was added to the composite, both the tensile strength and Young's modulus were largely increased until

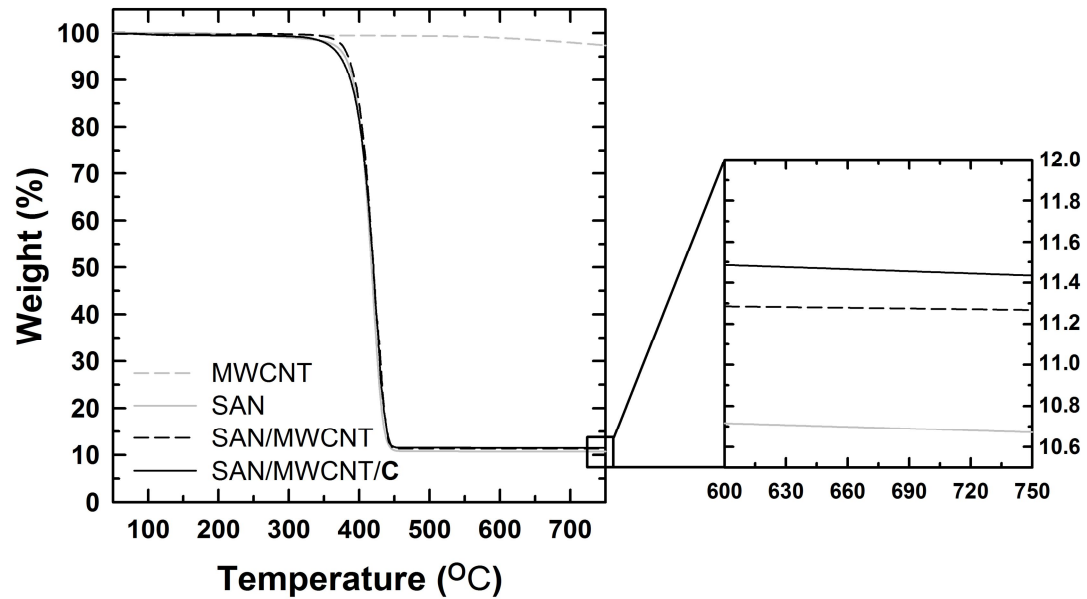


**Figure 3.7.** TGA traces of MWCNT, SAN, SAN/MWCNT, SAN/MWCNT/C with 1 wt.% MWCNTs.

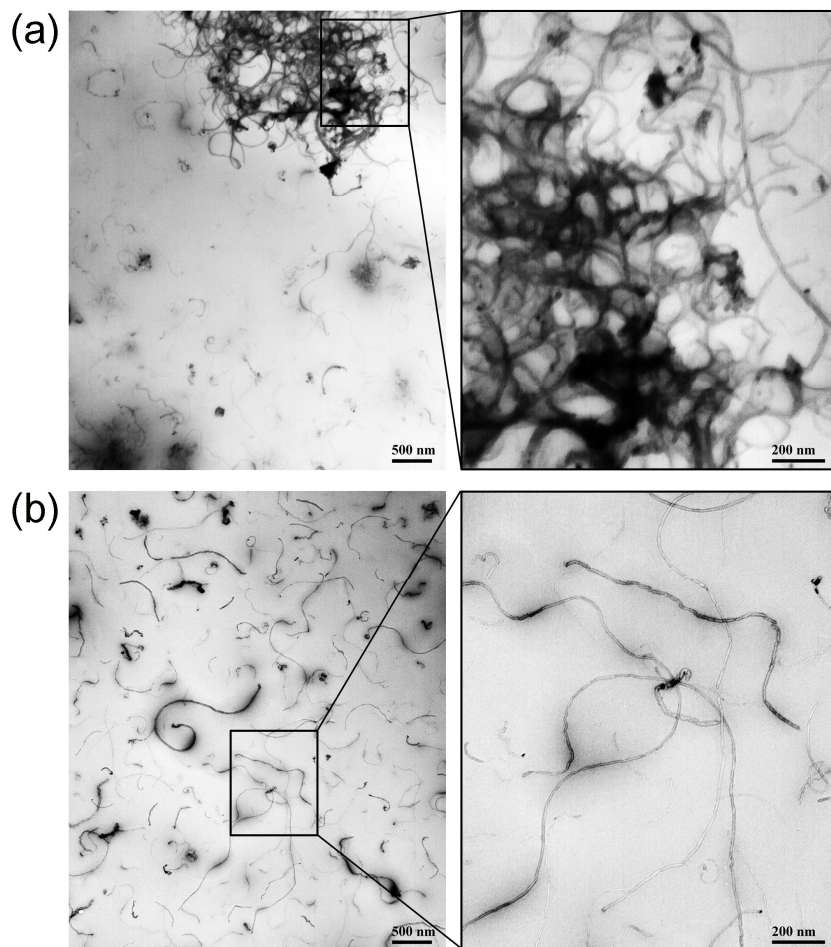


**Figure 3.8.** TEM images of (a) SAN/MWCNT and (b) SAN/MWCNT/C with 1 wt.% MWCNTs. Right side images are magnified ones.

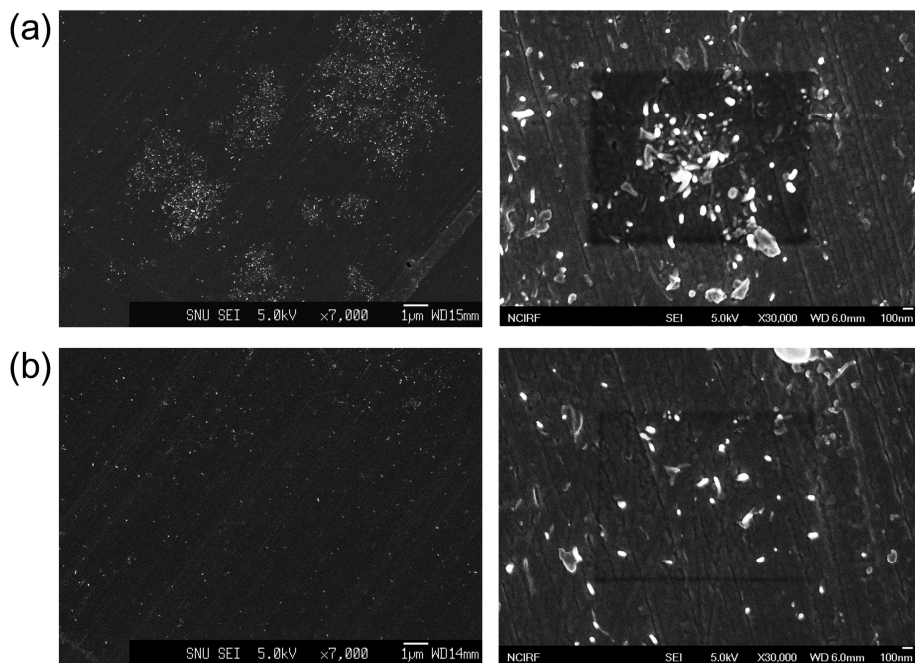


**Figure 3.9.** FE-SEM images of the fracture surface of (a) SAN/MWCNT and (b) SAN/MWCNT/C with 1 wt.% MWCNTs. Right side images are magnified ones.

wt.% addition of MWCNTs as compared with those of neat SAN, indicating that the compatibilizer C enhances the interfacial adhesion and reduces the interfacial tension between SAN and MWCNTs to disperse MWCNTs more homogeneously in the SAN matrix.

### **3.1.5 Electrical properties of composites**

When the electrical conductivity of SAN/MWCNT is compared with that of SAN/MWCNT/C, as shown in Figure 3.12, it reveals that the electrical conductivity of SAN/MWCNT starts to increase at 1 wt.% loading of MWCNTs, while the electrical conductivity of SAN/MWCNT/C starts to increase at 0.5 wt.% loading of MWCNTs, indicating that the formation of conducting network in SAN/MWCNT/C is achieved at lower MWCNT concentration than SAN/MWCNT. According to the classical percolation theory, the electrical conductivity of composite with conductive filler can be described by a scaling law,  $\sigma = \sigma_0(P-P_c)^t$ , where  $\sigma$  is the electrical conductivity of composite,  $\sigma_0$  is the electrical conductivity of the MWCNTs agglomerates,  $P$  is the content of MWCNTs in the composite,  $P_c$  is the percolation threshold concentration of the composite, and  $t$  is the critical exponent related to the system dimension. The theoretical value of  $t$  is in the range of 1.6-2.0 for three dimensional (3D) percolating system, while experimental values of 1.3-3.1 have been reported.<sup>148-150</sup> Since the percolation threshold has been used as an indicator of carbon nanotube dispersion in polymer matrix, the percolation threshold concentrations of

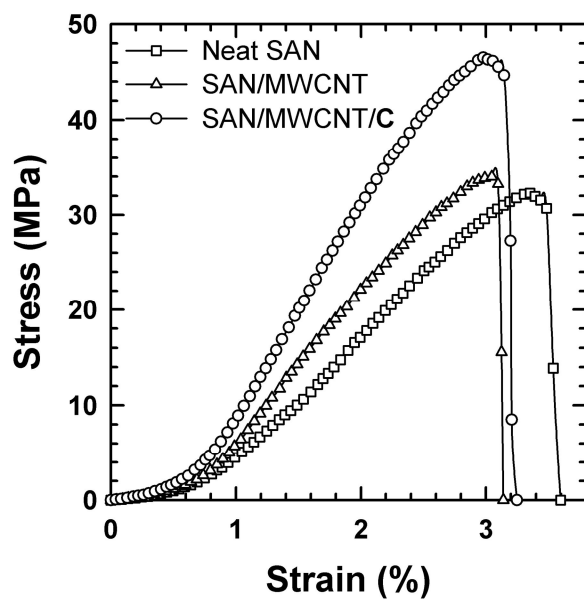


**Figure 3.10.** Stress-strain curves for the neat SAN, SAN/MWCNT, and SAN/MWCNT/C with 0.5 wt.% MWCNTs.

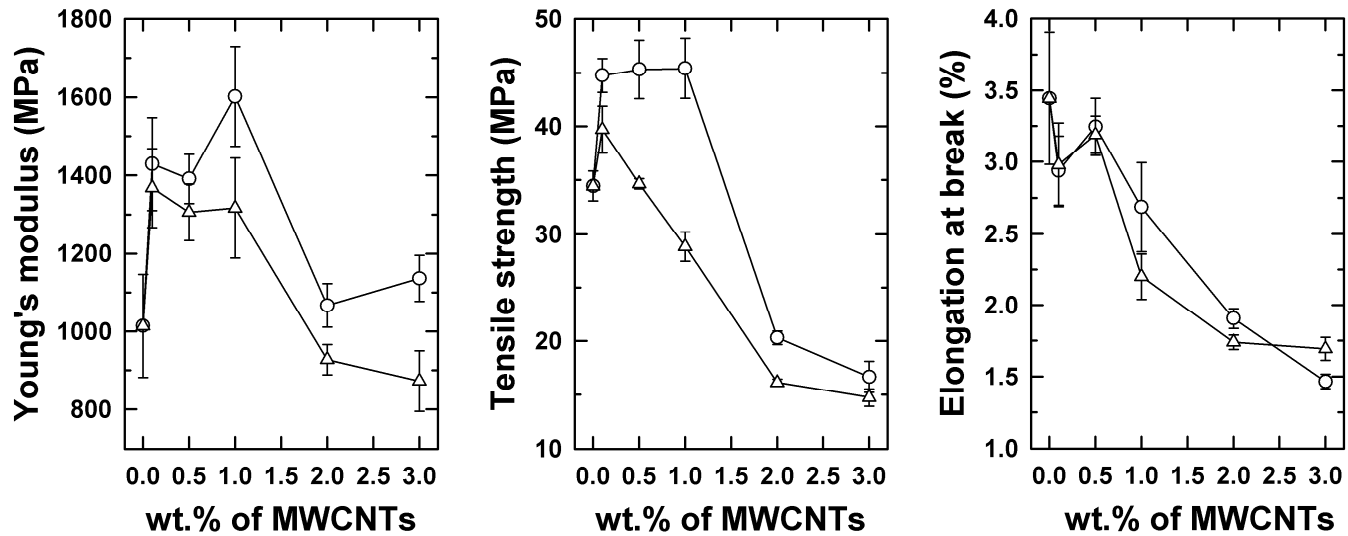


**Figure 3.11.** Tensile properties of SAN/MWCNT ( $\triangle$ ) and SAN/MWCNT/C ( $\circ$ ) composites as a function of the MWCNT content. The content of compatibilizer in composites is equal to that of MWCNT.

SAN/MWCNT and SAN/MWCNT/C are calculated using the scaling law, as shown in Figure 3.13. For SAN/MWCNT composites,  $P_c$  and  $t$  are calculated  $1.11 \pm 0.18$  wt.% and 2.01, whereas for the composite with the compatibilizer,  $P_c$  and  $t$  are calculated  $0.67 \pm 0.06$  wt.% and 2.18, respectively. The critical exponents of the composites are in accordance with theoretical expectation and experimental observation, indicating that 3D percolating network of MWCNT is formed in both SAN/MWCNT and SAN/MWCNT/C composites. Particularly, a decrease in the percolation threshold concentration in SAN/MWCNT/C is attributed to homogeneous dispersion of MWCNTs in SAN matrix.

### 3.1.6 Summary

A new compatibilizer, PVBEN-*g*-PMMA, that can effectively disperse MWCNTs in SAN matrix was synthesized. It was identified from the fluorescence quenching experiment that naphthalene unit in backbone interacts strongly with MWCNTs via  $\pi$ - $\pi$  interaction. When a small amount of the compatibilizer was added to SAN/MWCNT composites, the tensile strength and Young's modulus of the composites were largely increased as compared with those of the composites without compatibilizer. The percolation threshold concentration of electrical conductivity of the composites with the compatibilizer is lower than that of composite without compatibilizer. The improved mechanical properties and electrical

conductivity of SAN/MWCNT/PVBEN-*g*-PMMA are attributed to homogeneous dispersion of MWCNTs functionalized non-covalently with the compatibilizer in SAN matrix.

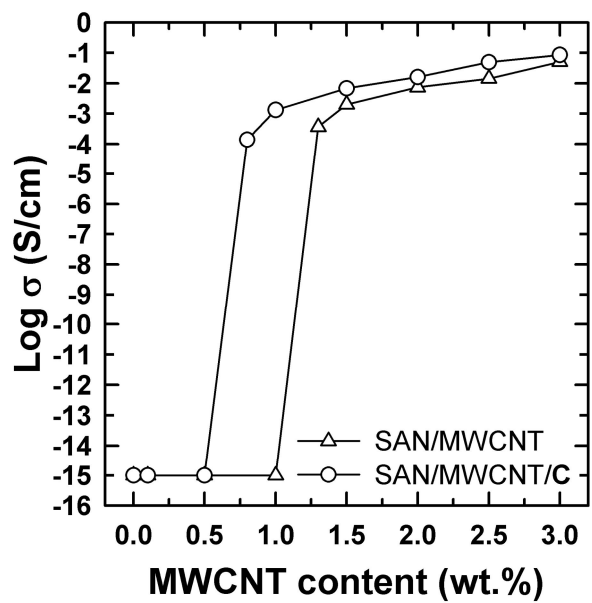


**Figure 3.12.** Electrical conductivity of SAN/MWCNT and SAN/MWCNT/C composite films as a function of MWCNT content.

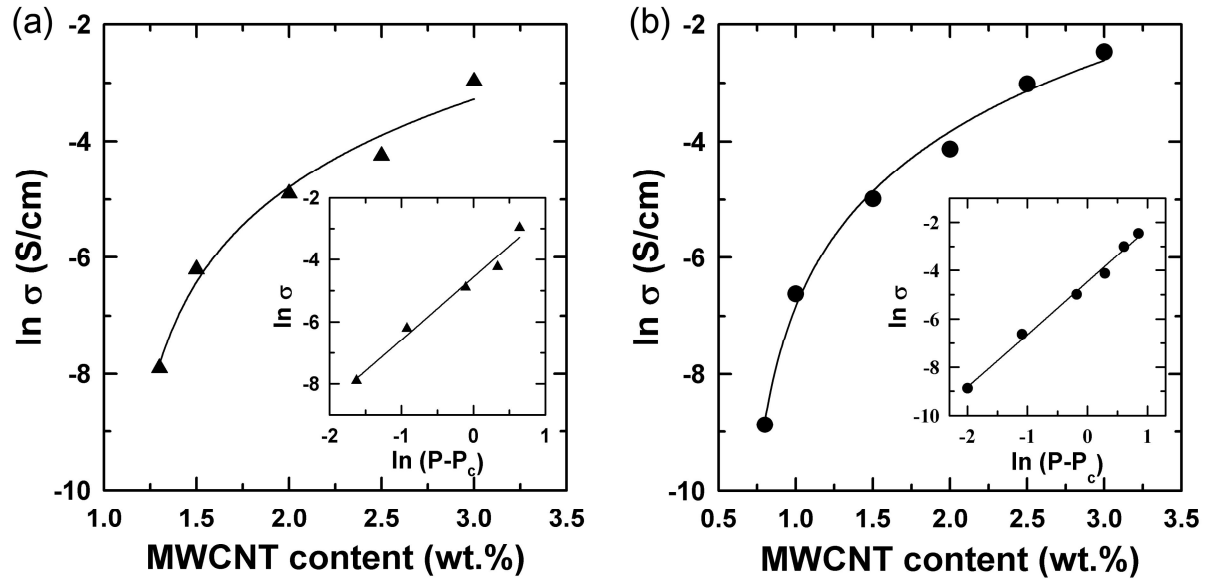


**Figure 3.13.** Determination of percolation threshold concentration of SAN/MWCNT (a) and SAN/MWCNT/C (b) composite films.

## 3.2 N66/compatibilizer/MWCNT composites

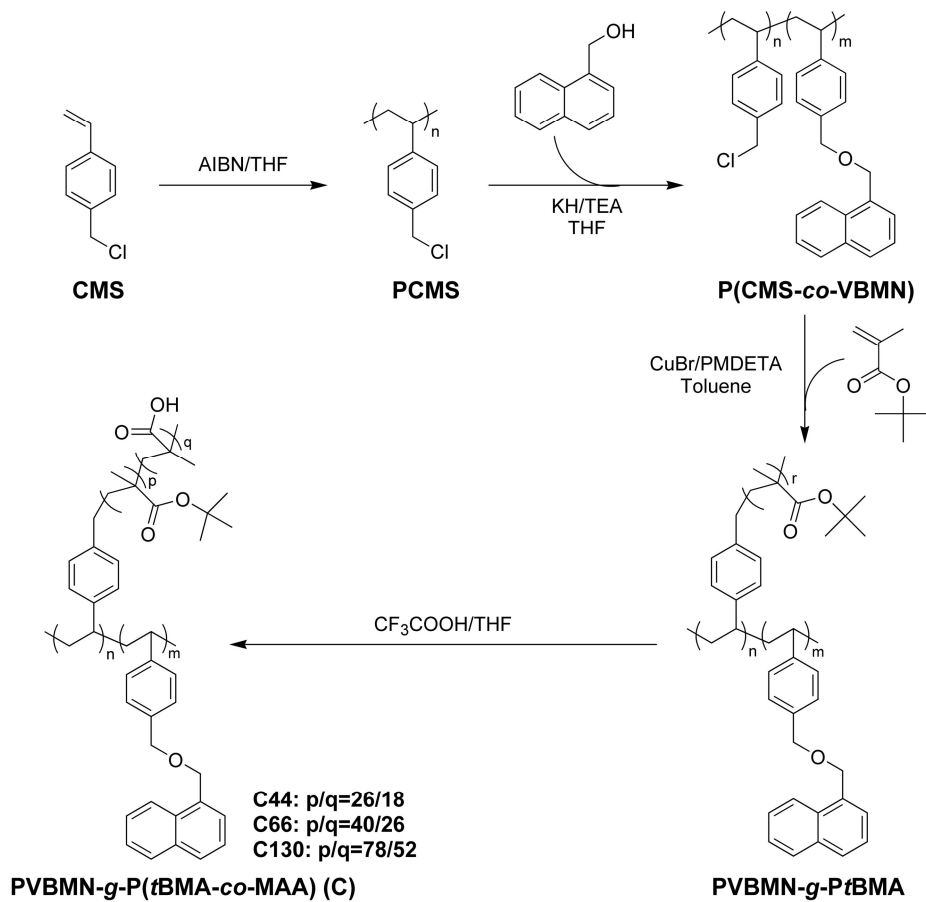
### 3.2.1 Synthesis and characterization

The overall synthesis route is represented in Scheme 3.2. A new compatibilizer, PVBMN-*g*-P(*t*BMA-*co*-MAA) (C in Scheme 3.2), was synthesized by four reaction steps. The chemical structures of P(CMS-*co*-VBMN), PVBMN-*g*-P*t*BMA, and PVBMN-*g*-P(*t*BMA-*co*-MAA) (C) are identified by <sup>1</sup>H NMR (Figure 3.14, 3.15 and 3.16). The molecular weight and polydispersity index as measured by gel permeation chromatography are listed in Table 3.2. In the substitution reaction of PCMS to P(CMS-*co*-VBMN), although most of CMS in PCMS were changed to VBMN, a small portion of CMS was not reacted and the chloride in CMS played a role as initiating site for ATRP reaction. The molar ratio of CMS to VBMN in P(CMS-*co*-VBMN) is about 1/20 as determined by <sup>1</sup>H NMR (Figure 3.14), indicating that an initiating site for ATRP is located at every 21 VBMN units in the copolymer. The average degree of polymerization (DP) of the graft chain (P*t*BMA) in PVBMN-*g*-P*t*BMA is estimated from <sup>1</sup>H NMR (Figure 3.15). Three PVBMN-*g*-P(*t*BMA-*co*-MAA)s with different graft lengths of P*t*BMA but the same backbone were synthesized (Scheme 3.2) in order to investigate the effect of the number of carboxylic acid groups in the graft chain of compatibilizer on both the dispersion of MWCNTs in N66 matrix and the mechanical and electrical properties of N66/MWCNT composites. The infrared absorption bands at 1700 cm<sup>-1</sup> and 3000 cm<sup>-1</sup>–3700 cm<sup>-1</sup>,

corresponding to the stretching of C=O of carboxylic acid and hydroxyl group, respectively, are observed when PVBMN-*g*-PtBMA is hydrolyzed (Figure 3.17), indicating clearly that some of *t*-butyl groups are converted into carboxylic acid group. When the average degree of hydrolysis was determined from the relative reduction of the peak intensity at  $\delta=1.35$  in  $^1\text{H}$  NMR spectrum corresponding to the chemical shift of proton in *t*-butyl group (Figure 3.15 and Figure 3.16), the degree of hydrolysis of *t*-butyl groups in all the compatibilizers (**C44**, **C66** and **C130**) was 40%.

### 3.2.2 Identification of interaction

Both the specific interaction between compatibilizer and MWCNTs and the hydrogen bonding between compatibilizer and N66 are the most important requirement to disperse MWCNTs in N66 matrix and thus to achieve improvement of mechanical and electrical properties of composites. First, the  $\pi$ - $\pi$  interaction between compatibilizer and MWCNTs was evaluated by using both the fluorescence emission spectroscopy and Raman spectroscopy. Figure 3.18 shows comparison of the fluorescence emission spectrum of N66/**C44** with that of N66/MWCNT/**C44**, where the emission spectra were obtained by irradiating the solution at 270 nm corresponding to the absorption wavelength of naphthalene units in **C44**. The N66/**C44** emits strongly fluorescence in solution, as shown in Figure 3.18(a), whereas the fluorescence emitted from naphthalene units is completely quenched in N66/MWCNT/**C44** due to an effective energy transfer between naphthalene



**Scheme 3.2.** Synthesis route of compatibilizers, PVBMN-g-P(*t*BMA-co-MAA)s.

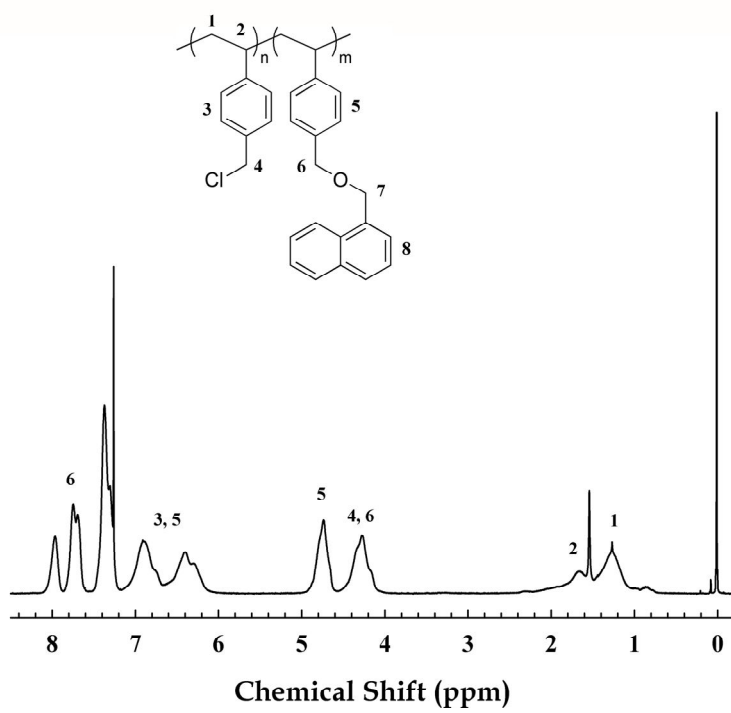


**Figure 3.14.** Chemical structure and <sup>1</sup>H NMR spectra of P(CMS-co-VBMN).

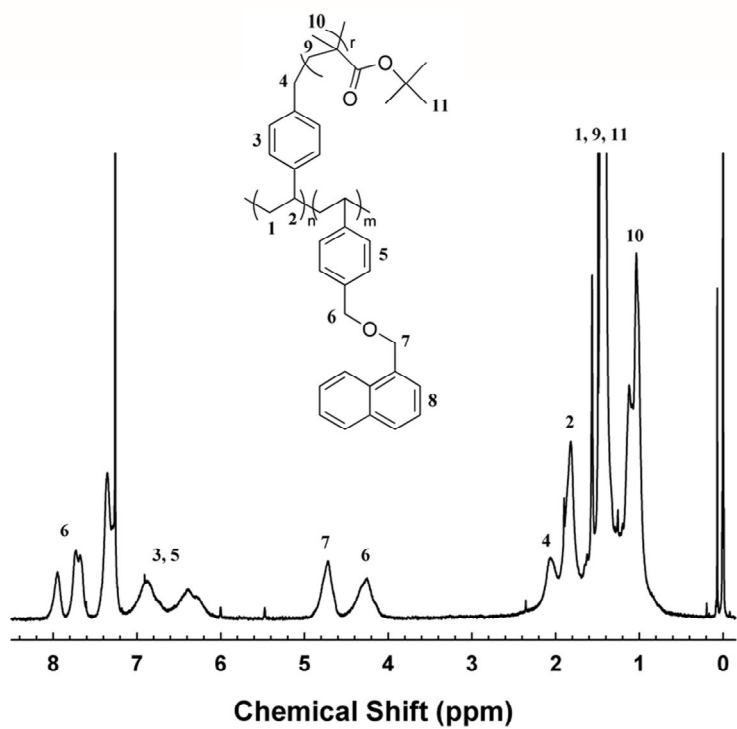


**Figure 3.15.** Chemical structure and  $^1\text{H}$  NMR spectra of PVBMN-g-PtBMA.

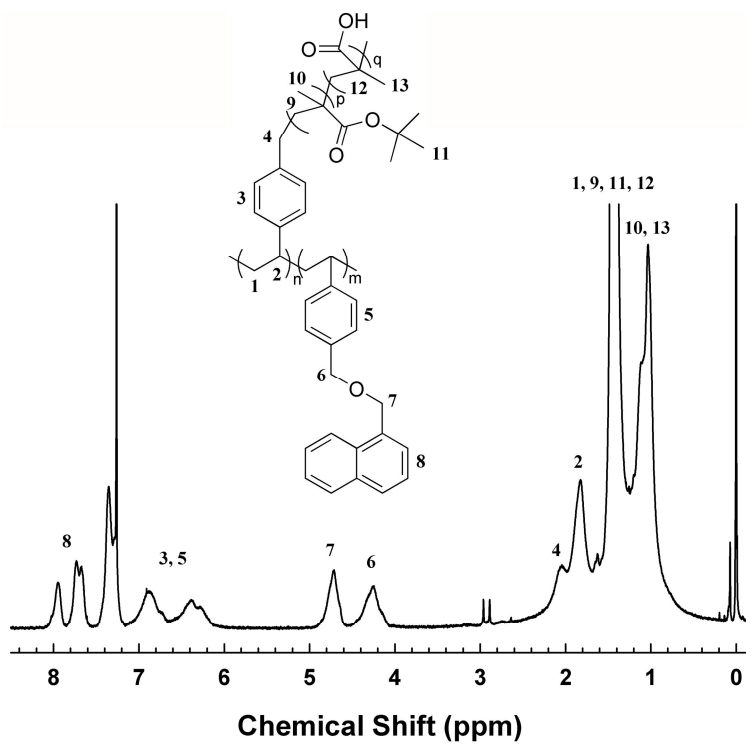


**Figure 3.16.** Chemical structure and <sup>1</sup>H NMR spectra of PVBMN-g-P(*t*BMA-co-MAA).

**Table 3.2.** Molecular characteristics of compatibilizers.

Sample	$M_n$ (g/mol) <sup>a</sup>	$M_w/M_n$ <sup>a</sup>	n:m <sup>b</sup>	DP of PtBMA <sup>c</sup>	p:q <sup>b</sup>
PCMS	16,700	1.61	-	-	-
P(CMS- <i>co</i> -VBMN)	20,000	1.58	1:20	-	-
	54,400	1.34	1:20	44	-
PVBMN- <i>g</i> -PtBMA	61,200	1.41	1:20	66	-
	98,000	1.58	1:20	130	-
<b>C44</b>	46,400	1.8	1:20	44	3:2
<b>C66</b>	53,100	1.50	1:20	66	3:2
<b>C130</b>	87,400	1.55	1:20	130	3:2

<sup>a</sup> Determined by gel permeation chromatography.

<sup>b</sup> The ratio of n:m and p:q are defined in Figure 3.15 and determined by <sup>1</sup>H NMR.

<sup>c</sup> Determined by <sup>1</sup>H NMR.

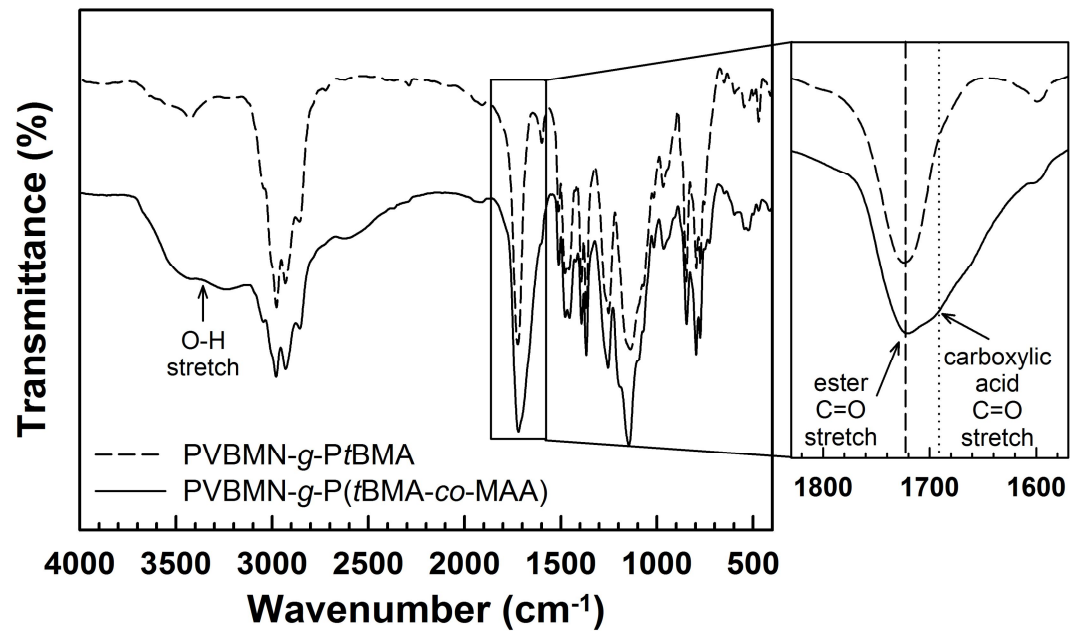


Figure 3.17. FT-IR spectra before and after hydrolysis of PVBMN-g-PtBMA.

unit of **C44** and MWCNTs, indicating that there exists the strong  $\pi$ - $\pi$  interaction between MWCNTs and naphthalene units of **C44** in solution. When the fluorescence emission spectrum of N66/**C44** film is compared with that of N66/MWCNT/**C44** film, as shown in Figure 3.18(b), it is also realized that the fluorescence emitted from N66/**C44** film is completely quenched in N66/MWCNT/**C44** film, indicating the strong  $\pi$ - $\pi$  interaction between naphthalene units of **C44** and MWCNTs is still available in solid state.

Raman spectroscopy can also be used for verifying the  $\pi$ - $\pi$  interaction between MWCNTs and compatibilizer by observing the shift of G-band of MWCNTs. It has been known that the strong attachment of polymer onto the surface of CNTs leads the shift of G-band toward higher frequency due to an increase in the elastic constant of the harmonic oscillator of polymer-coated CNTs. Since it has been observed that the G-band of MWCNTs in N66/MWCNT/**C44** slightly shifts to higher frequency ( $\sim 7 \text{ cm}^{-1}$ ) as compared to that of the pristine MWCNTs while the G-band of MWCNTs in N66/MWCNT remains unchanged, as shown in Figure 3.19, it is concluded that the main chain in **C44** strongly interacts with MWCNTs through  $\pi$ - $\pi$  interaction.

The interaction between compatibilizer **C44** and N66 matrix was identified by comparing FT-IR spectra of N66 and N66/**C44**, as shown in Figure 3.20. Since it is generally known that the N-H stretching band of hydrogen-bonded NH group appears at higher frequency than that of free NH group,<sup>151,152</sup> the absorption bands of  $3300 \text{ cm}^{-1}$  and  $3400 \text{ cm}^{-1}$  in N66

spectrum correspond to hydrogen-bonded N–H stretching and free N–H stretching, respectively. When the spectrum of N66/C44 is compared with that of N66, the absorption intensity of hydrogen-bonded N–H stretching in N66/C44 becomes stronger than that of free NH group, indicating that the number of hydrogen-bonded NH groups is increased due to hydrogen bonding between NH group in N66 and carboxylic acid group of C44, as shown in Fig. 3.20. This observation clearly demonstrates that the carboxylic acid group in C44 interacts with the amide group in N66 through hydrogen bonding.

### **3.2.3 Dispersity of MWCNTs in N66 matrix**

Figure 3.21 compares TEM images of N66/MWCNT and N66/MWCNT/C44 composites. The TEM image of N66/MWCNT without the compatibilizer shows severe aggregation of MWCNTs in N66 matrix, while the TEM image of N66/MWCNT/C44 exhibits homogeneous dispersion of MWCNTs in N66 matrix, indicating that the compatibilizer C44 can effectively disperse MWCNTs in N66 matrix by reducing the interfacial tension between N66 and MWCNTs. This result is further identified by FE-SEM images (Figure 3. 22).

### **3.2.4 Tensile properties of composites**

Figure 3.23 shows the variation of average tensile properties of neat N66,

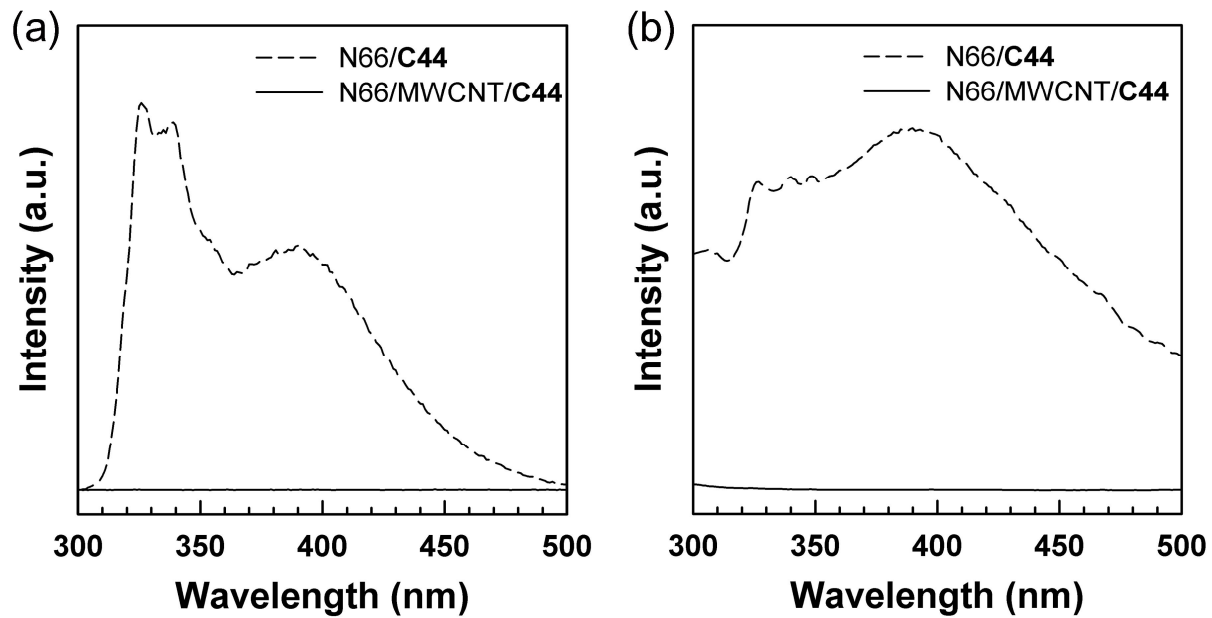


**Figure 3.18.** Fluorescence emission spectra of compatibilizer in solution (a) and in film (b).

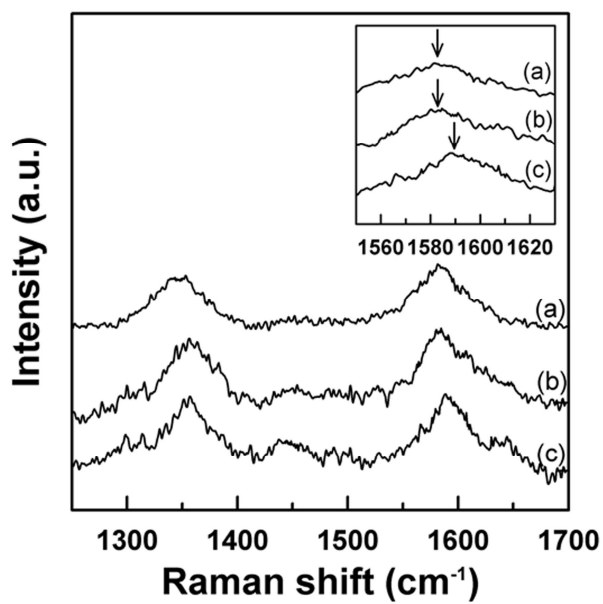


**Figure 3.19.** Raman spectra of the MWCNTs (a), N66/MWCNT (99/1 w/w) (b), and N66/MWCNT/C44 (99/1/1 w/w/w) (c) with 1 wt.% MWCNTs.

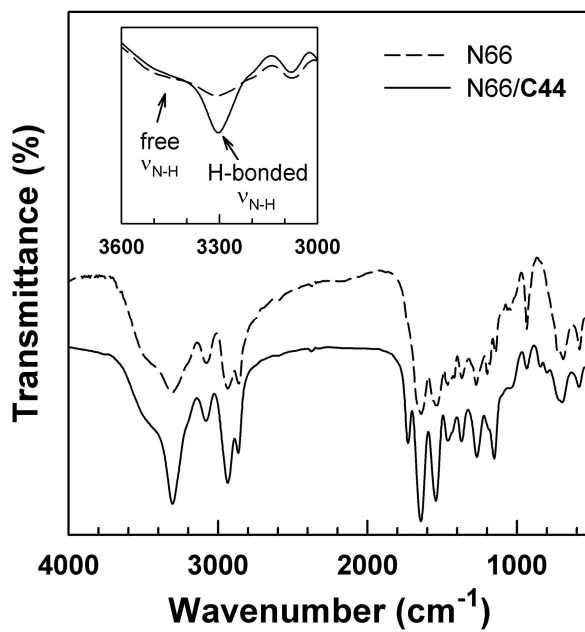


**Figure 3.20.** FT-IR spectra of N66 and N66/C44. Close examination reveals that the absorption band of hydrogen-bonded N–H stretching of N66/C44 at  $3300\text{ cm}^{-1}$  is stronger than that of N66.

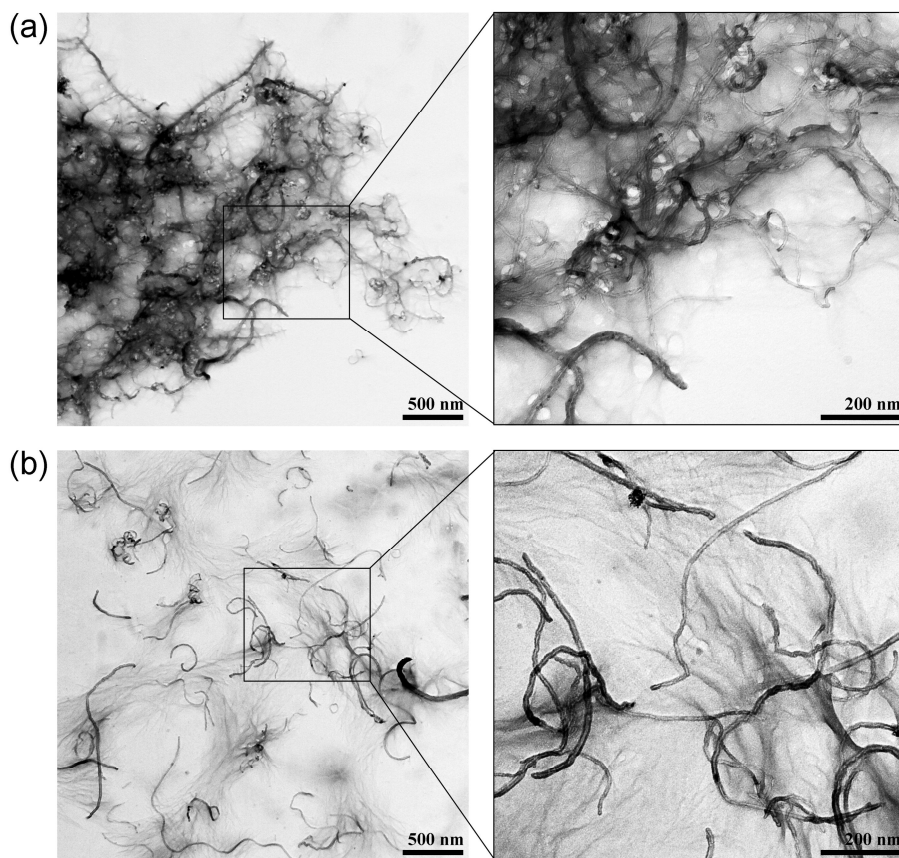


**Figure 3.21.** TEM images of N66/MWCNT (a) and N66/MWCNT/C44 (b).

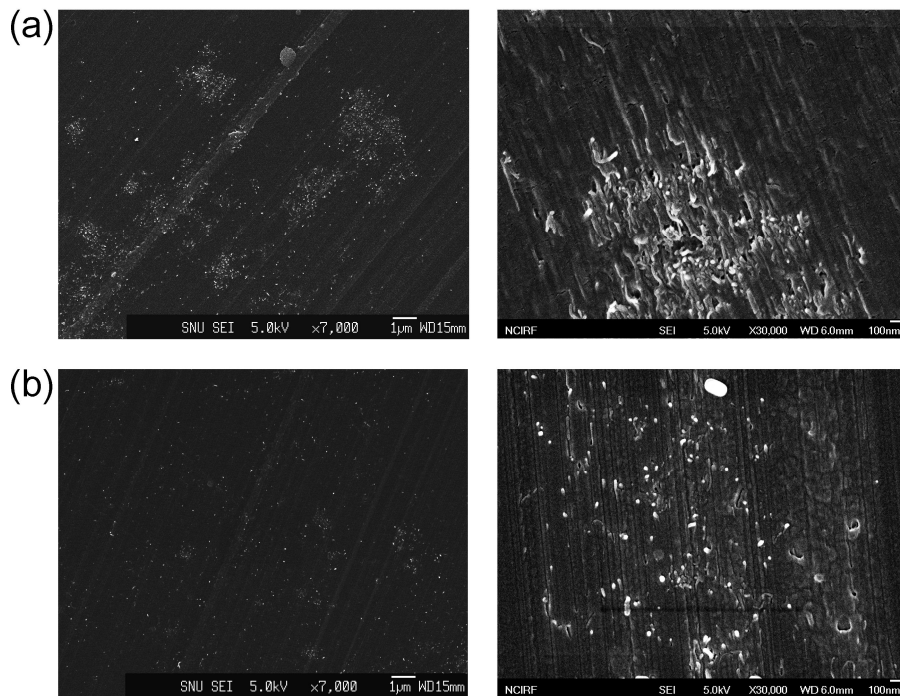


**Figure 3.22.** FE-SEM images of the fracture surface of N66/MWCNT (a) and N66/MWCNT/C44 (b) with 1 wt.% MWCNTs. Right side images are magnified ones.

N66/MWCNT, and N66/MWCNT/C44 with the MWCNT loading. When the tensile properties of N66/MWCNT composites are compared with those of the neat N66, it reveals that both tensile strength and Young's modulus are increased up to 0.1 wt.% addition of MWCNTs and then decreased considerably as compared with those of neat N66 as the addition of MWCNTs is further increased. This negative behavior is attributed mainly to poor dispersion of MWCNTs in N66 matrix, as shown in Figure 3.21 and Figure 3.22. However, when the compatibilizer C44 was added to N66/MWCNT composites, both tensile strength and Young's modulus of the composites were largely increased without large sacrifice of elongation-at-break. This improvement may arise from good interfacial dispersion between MWCNTs and N66 owing to the compatibilizer. It should be noted here that the improvement of mechanical properties of N66/MWCNT/C44 does not come from the change of crystallinity of N66 in composites (Figure 3.24). From the results of tensile test, TEM and DSC, it is concluded that the improvement of tensile properties of N66/MWCNT/C44 composite is attributed to the homogeneous dispersion of MWCNTs in matrix and good interfacial adhesion between N66 and MWCNTs in the presence of compatibilizer.

### **3.2.5 Electrical properties of composites**

Percolation threshold has been used as an indicator of CNT dispersion in polymer matrix.<sup>148-150</sup> When the electrical conductivity of N66/MWCNT is

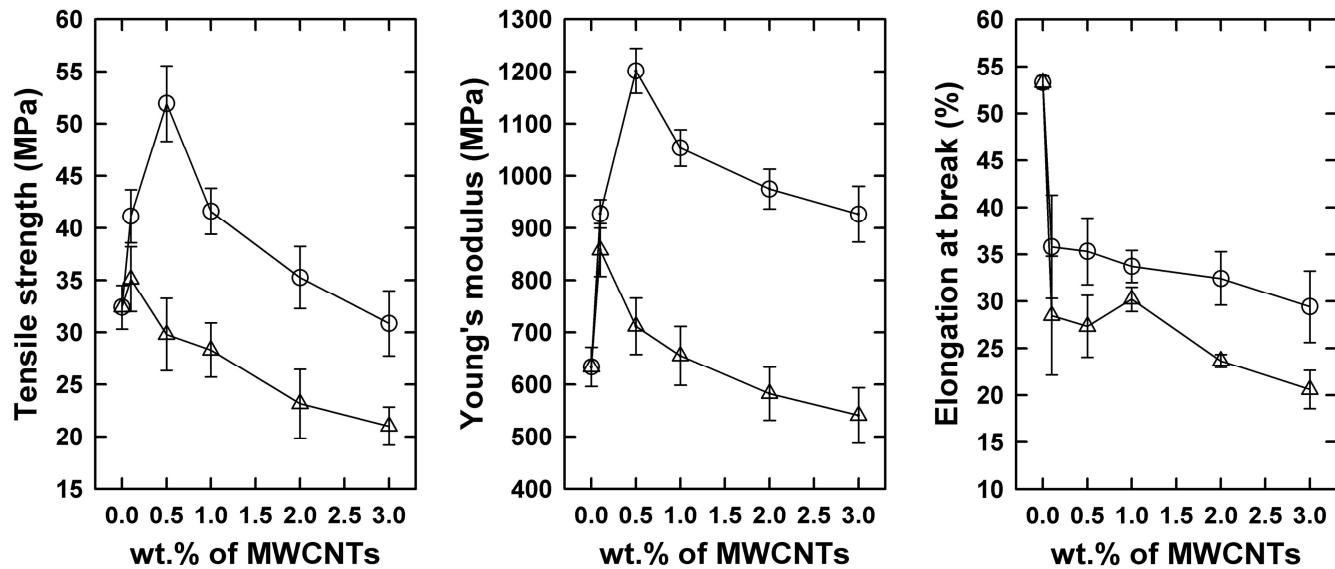


**Figure 3.23.** Tensile properties of N66/MWCNT ( $\Delta$ ) and N66/MWCNT/C44 ( $\circ$ ) composites as a function of the MWCNT content. The content of compatibilizer in composites is equal to that of MWCNT.

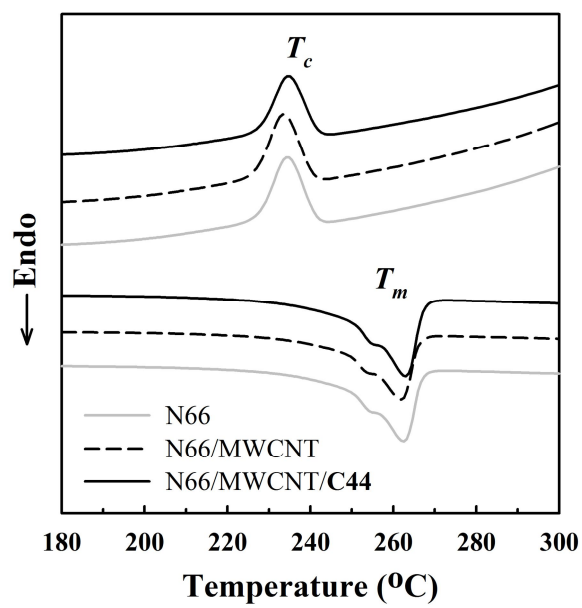


**Figure 3.24.** DSC thermograms of neat N66, N66/MWCNT, N66/MWCNT /C44 with 1 wt.% MWCNT.

compared with that of N66/MWCNT/C44, as shown in Figure 3.25, it reveals that the electrical conductivity of N66/MWCNT and N66/MWCNT/C44 start to increase at 1.5 wt.% and 0.9 wt.% loading of MWCNTs, respectively, indicating that the MWCNT network in N66 matrix of N66/MWCNT/C44 is formed at lower MWCNT concentration than N66/MWCNT. For determination of the percolation threshold concentration, a scaling law is used in the form of  $\sigma = \sigma_0(P-P_c)^t$  for  $P > P_c$ , where  $\sigma$  is the electrical conductivity of composite,  $\sigma_0$  is the electrical conductivity of MWCNT agglomerates,  $P$  is the concentration of MWNCTs in the composite,  $P_c$  is the percolation threshold concentration of the composite, and  $t$  is the critical exponent related to the system dimension. The values of  $P_c$  and  $t$  are determined by fitting the scaling law to the conductivity data, as shown in Figure 3.26.  $P_c$  and  $t$  for N66/MWCNT are 1.28 wt.% and 2.15, and  $P_c$  and  $t$  for N66/MWCNT/C44 are 0.87 wt.% and 2.24, respectively. The values of critical exponents are in accordance with theoretical expectation and other experimental observation, indicating that the 3D percolating network of MWNCTs is formed in both N66/MWCNT and N66/MWCNT/C44 composites. Particularly, a significant decrease in the percolation threshold concentration of N66/MWCNT/C44 is attributed to homogeneous dispersion of MWCNTs in N66 matrix.

### **3.2.6 Effect of the number of carboxylic acid groups**

Three different compatibilizers (Table 3.2) with different content of acrylic

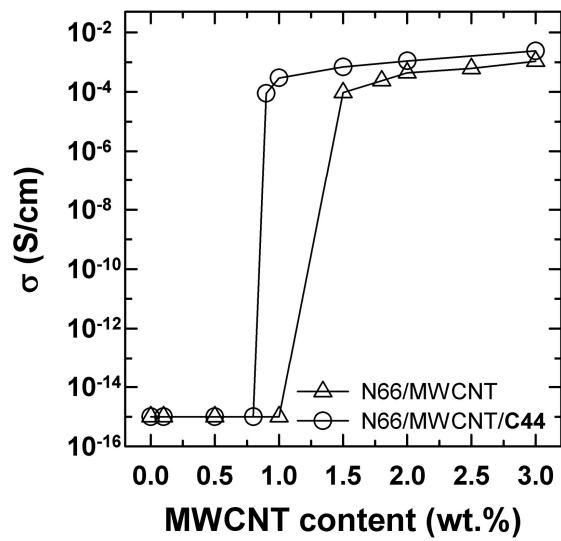


**Figure 3.25.** Electrical conductivity of N66/MWCNT and N66/MWCNT/C44 composites.

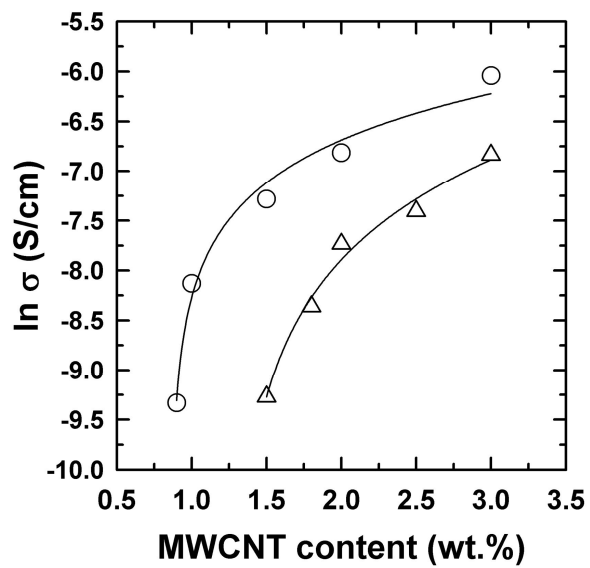


**Figure 3.26.** Percolation threshold concentration of N66/MWCNT ( $\triangle$ ) and N66/MWCNT/C44 ( $\circ$ ) composites.

acid unit were prepared in order to examine the effect of the number of carboxylic acid group on the dispersion of MWCNTs and physical properties of the composites. When the tensile properties and electrical conductivity of N66/MWCNT composites with three different compatibilizers are compared, as listed in Table 3.3, the tensile properties and electrical conductivity of N66/MWCNT/C44 composite are higher than the others, indicating that the compatibilizer with the least content of carboxylic acid groups (C44) is most effective for improving mechanical and electrical properties of the composites. To elucidate the reason for this, the degrees of  $\pi$ - $\pi$  interaction between three compatibilizers (C44, C66 and C130) and MWCNTs are evaluated by comparing the fluorescence emission spectra of composites, as shown in Figure 3.27. The fluorescence of naphthalene unit in C66 and C130 composite films is not completely quenched in composite film, while the fluorescence of naphthalene in C44 composite film is completely quenched. This result clearly indicates that C44 interacts stronger with MWCNTs than C66 and C130. This is probably because the compatibilizers (C66 and C130) with larger number of carboxylic acid group interact more favorably with N66 than with MWCNTs, which results in weaker interaction between the compatibilizers and MWCNTs. In short, the compatibilizer with the least number of carboxylic acid groups is the best compatibilizer among the compatibilizers synthesized in this study.

**Table 3.3.** Mechanical and electrical properties of composites with 1 wt.% MWCNTs.

Sample	Tensile strength (MPa)	Young's modulus (MPa)	Elongation at break (%)	Electrical conductivity (S/cm)
N66	32.4±2.1	633±38	53.3±0.7	10 <sup>-15</sup>
N66/MWCNT	28.3±2.6	654±56	30.2±1.2	10 <sup>-15</sup>
N66/MWCNT/C44	41.6±2.2	1053±35	33.7±1.3	2.94x10 <sup>-4</sup>
N66/MWCNT/C66	30.1±2.0	851±45	31.5±0.7	1.07x10 <sup>-4</sup>
N66/MWCNT/C130	28.8±3.4	792±39	32.1±1.1	1.22x10 <sup>-4</sup>

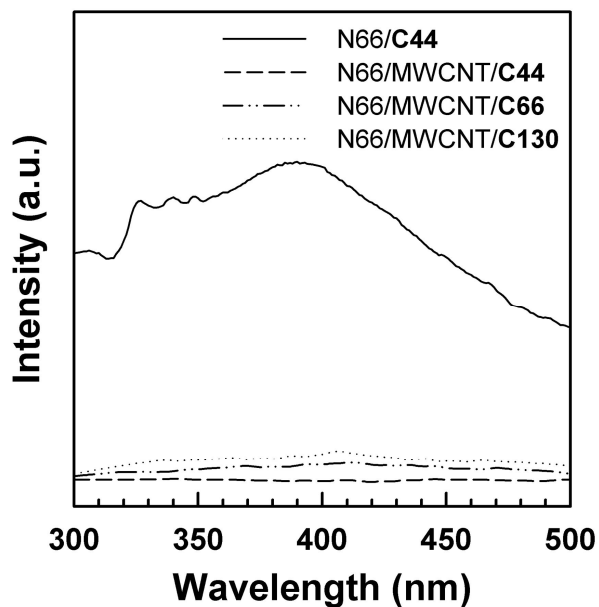


**Figure 3.27.** Fluorescence emission spectra of N66/MWCNT composites with different compatibilizers (C44, C66 and C130).

### 3.2.6 Summary

A new compatibilizer, PVBMN-*g*-P(*t*BMA-*co*-MAA), is synthesized for N66/MWCNT composites. The fluorescence emission spectra and FT-IR spectra verify that naphthalene and carboxylic acid units in the compatibilizer strongly interact with MWCNTs and N66, respectively. When a small amount of the compatibilizer is added to N66/MWCNT composite, MWCNTs are well dispersed in N66 matrix and as a result the mechanical and electrical properties of the composites are improved much larger than the simple mixture of N66/MWCNT. The compatibilizer with the least amount of carboxylic acid is most effective among the compatibilizers examined in this study, because the compatibilizer with the least carboxylic acid groups interact more strongly with MWCNTs by  $\pi$ - $\pi$  interaction as compared to the compatibilizers with higher amount of carboxylic acid groups, as evidenced by the fluorescence quenching.

## 3.3 Graphene nanoribbon (GNR)

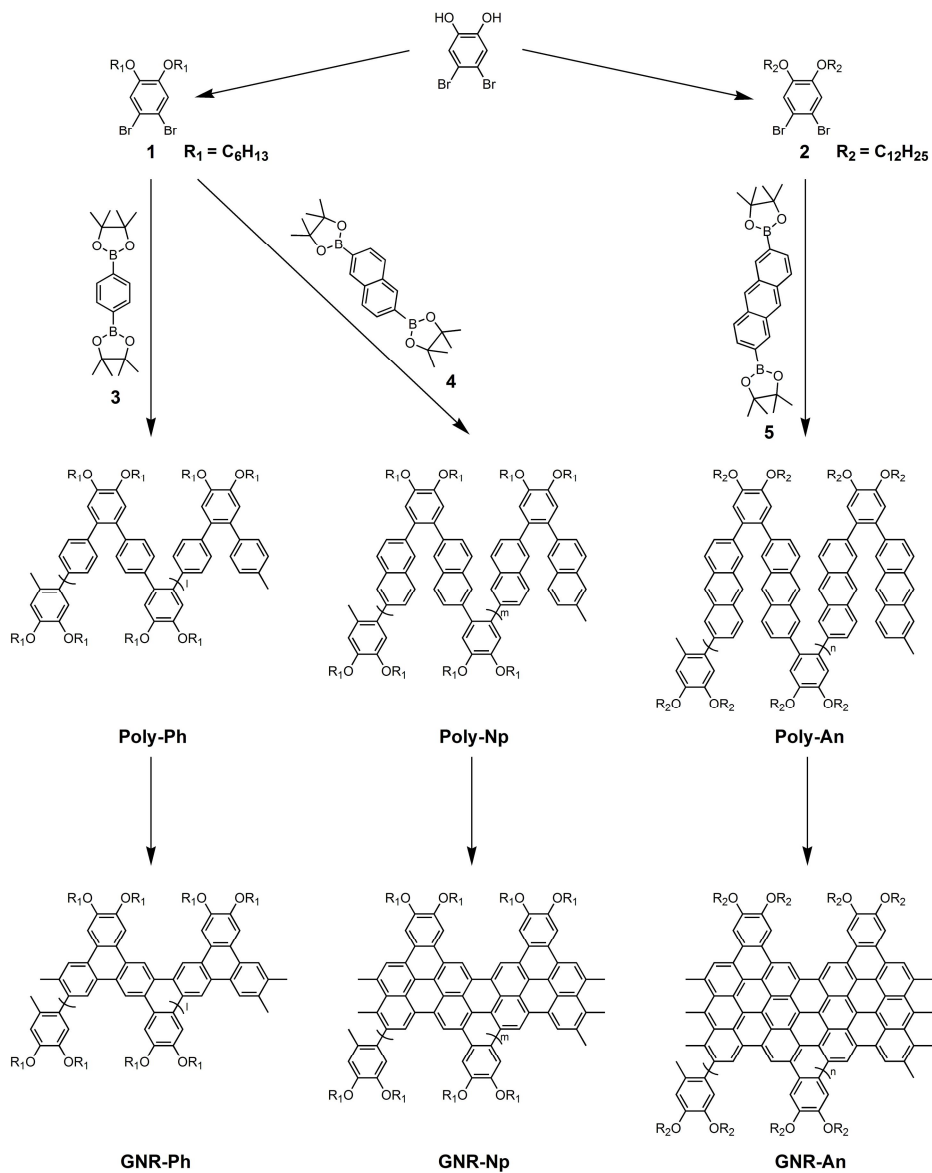
### 3.3.1 Synthesis and characterization

The general synthetic route for GNRs is outlined in Scheme 3.3. Three precursor polymers, Poly-Ph, Poly-Np and Poly-An, were synthesized by the Suzuki coupling reaction between the corresponding dibromo monomer and diboronic ester monomer. The precursor polymers were then converted into the corresponding GNRs (GNR-Ph, GNR-Np and GNR-An) through an intramolecular cyclodehydrogenation reaction in the presence of  $\text{FeCl}_3$  in dichloromethane as an oxidant at room temperature for 3 days. Since the precursor polymer prepared from dibromo-benzene with hexyloxy group and anthracene is insoluble in organic solvents after cyclodehydrogenation, dibromo-benzene with dodecyloxy group is used for synthesis of Poly-An. The cyclodehydrogenation of precursor polymer was identified by  $^1\text{H}$  NMR (Figure 3.28). The peaks of aromatic protons in Poly-An (Ar-H, marked with “1, 2, 3, 4, 5” in Fig. 3.28) are shifted downfield from 7.03, 7.67, 8.11 and 8.43 to 7.21, 7.91, 8.33 and 8.66 by cyclodehydrogenation, respectively. The average degree of cyclodehydrogenation was determined from the intensity reduction of peaks 3, 4, 5 in GNR-An relative to the intensity of the corresponding peaks in Poly-An. Comparing the relative intensities of aromatic proton peaks (marked by “3, 4 and 5” in Fig. 3.28(a)) of Poly-An to the intensity of methylene protons (marked by “a”) with those of GNR-An (Figure 3.28(b)) reveals that the conversion of the oxidative reaction is 75%.

When the degree of cyclodehydrogenations of GNR-Ph and GNR-Np were determined by the same method as above, the average degrees of GNR-Ph and GNR-Np were 100% and 78%, respectively (see Figure 3.29 and 3.30). It should be noted here that completely cyclodehydrogenated GNR-Np and GNR-An become insoluble in organic solvents while completely cyclodehydrogenated GNR-Ph is soluble in most of organic solvents. The cyclodehydrogenation was also identified by the chemical shift change of aromatic carbons in  $^{13}\text{C}$  NMR spectra (see Figure 3.30, 3.31 and 3.32).

### **3.3.2 Identification of cyclodehydrogenation**

When the UV-Vis spectrum of GNR-An is compared with that of Poly-An, as shown in Figure 3.34, GNR-An exhibits much broader absorption than Poly-An. This phenomenon is also observed for GNR-Ph and GNR-Np. Since the fusion of aromatic rings by oxidative reaction increases the conjugation length, it is easily expected that GNRs expand the absorption range to longer wavelength. When the Raman spectrum of GNR-An was compared with that of Poly-An, it reveals that GNR-An clearly shows the first-order D band (disorder band) and G band (graphite band) at  $\sim 1330$  and  $\sim 1600\text{ cm}^{-1}$ , respectively (Fig. 3.35), which is consistent with literature values for GNRs,<sup>153,154</sup> whereas Poly-An does not show the D and G bands. GNR-Ph and GNR-Np also exhibit clearly D and G bands. This provides a direct evidence for cyclodehydrogenation of the polymer precursors to form GNRs. It should be noted here that the 2D band cannot be seen from Raman



**Scheme 3.3.** Synthetic routes of GNRs.



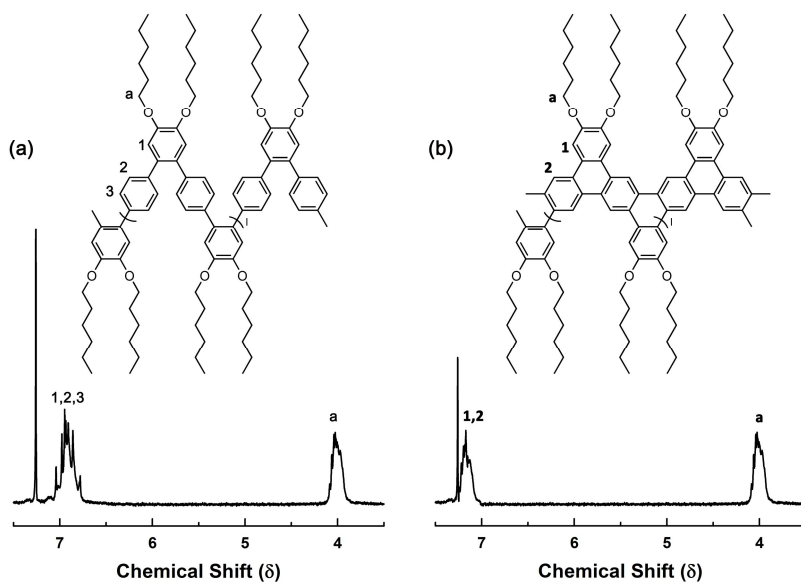


**Figure 3.29.** Chemical structures and  $^1\text{H}$  NMR spectra of (a) Poly-Ph and (b) GNR-Ph.

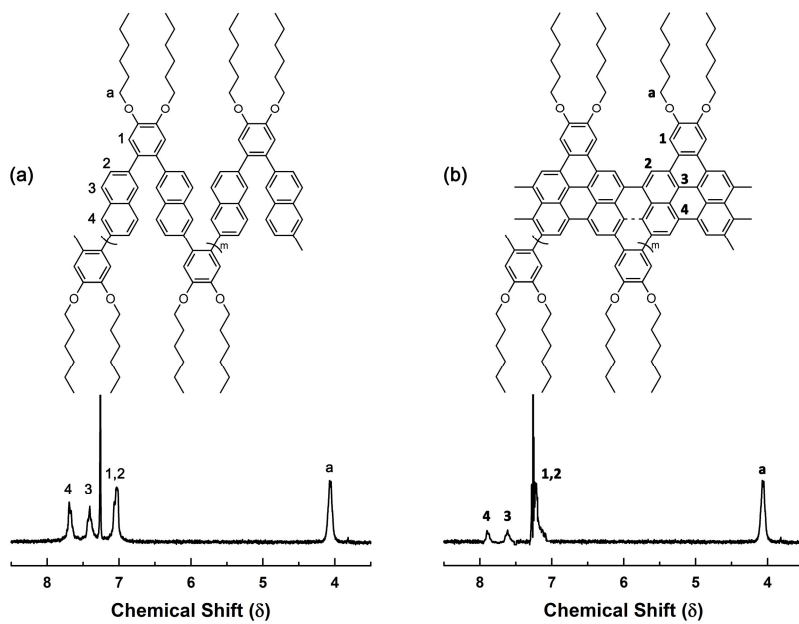


**Figure 3.30.** Chemical structures and  $^1\text{H}$  NMR spectra of (a) Poly-Np and (b) GNR-Np.

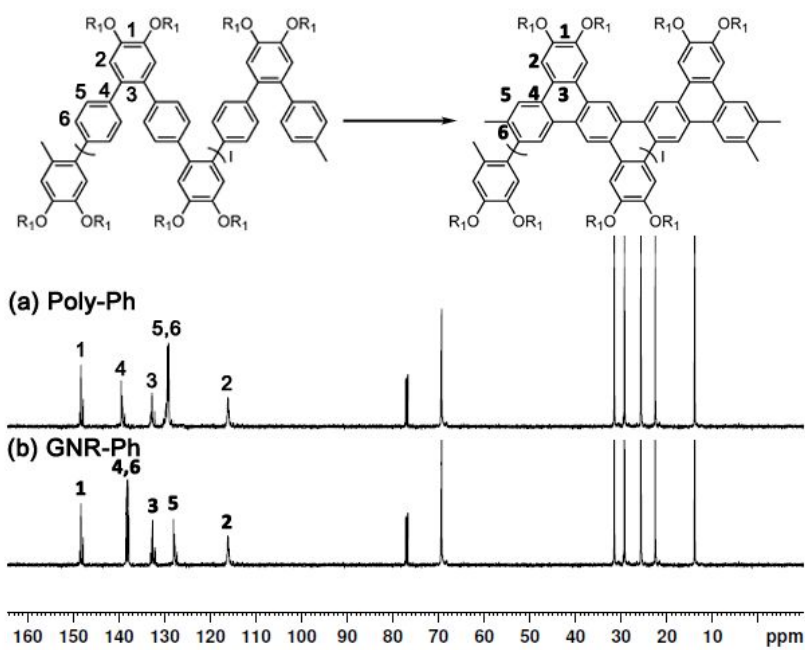


**Figure 3.31.** Chemical structures and  $^{13}\text{C}$  NMR spectra of (a) Poly-Ph and (b) GNR-Ph.

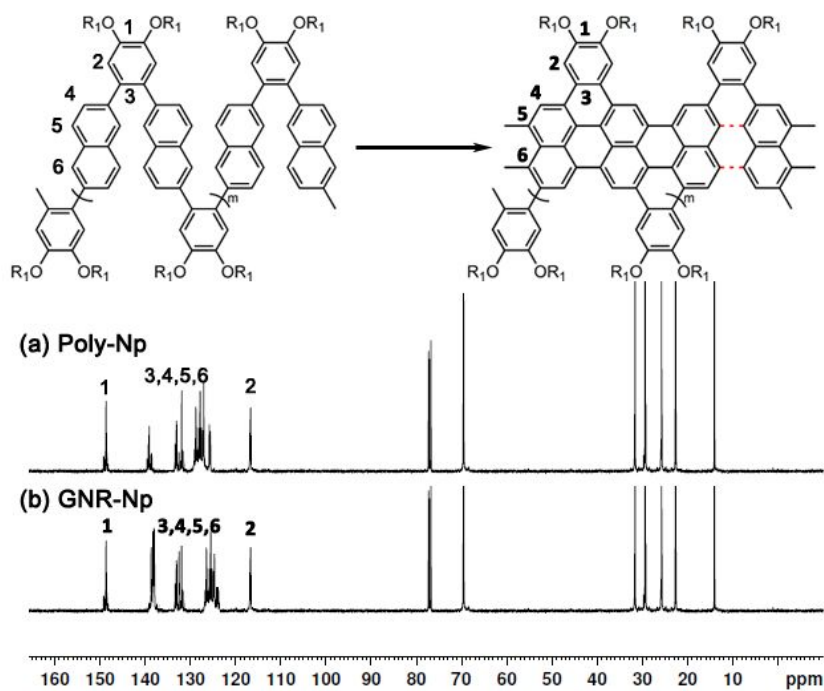


**Figure 3.32.** Chemical structures and  $^{13}\text{C}$  NMR spectra of (a) Poly-Np and (b) GNR-Np.

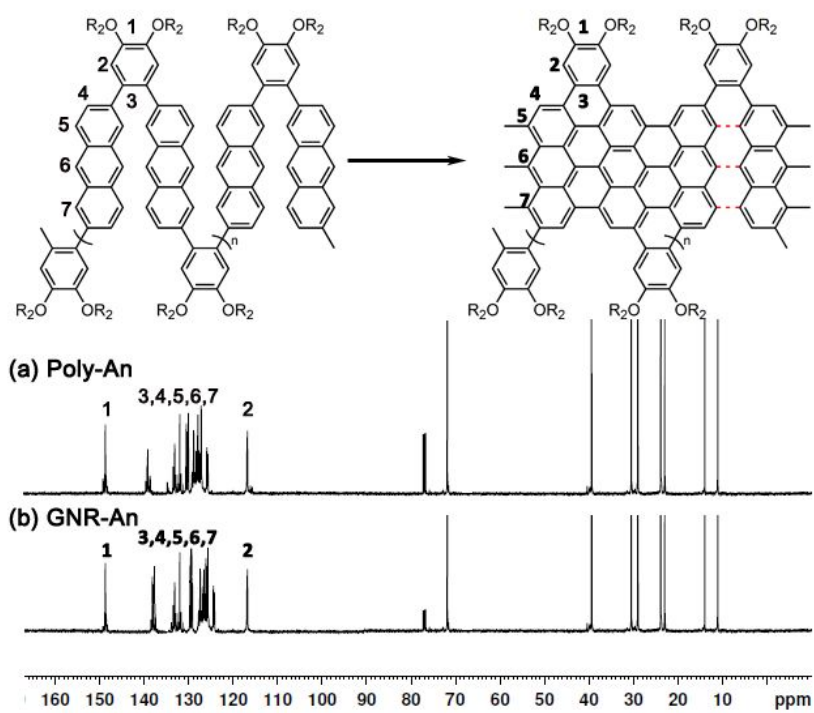


**Figure 3.33.** Chemical structures and  $^{13}\text{C}$  NMR spectra of (a) Poly-An and (b) GNR-An.

spectra of all GNRs, indicating that synthesized GRNs have disorder in c-axis to form turbostratic structures.<sup>155</sup> The decrease of retention time in GPC chromatogram of GNRs also supports the cyclodehydrogenation of polymers (see Figure 3.36).

### 3.3.3 TFT performance

Figure 3.37 compares the TFT performances of GNR-Ph, GNR-Np and GNR-An. The output characteristics of TFTs based on GNRs exhibit good current modulation and well-defined saturation regions (see Figure 3.38). The carrier mobility was evaluated from the transfer curve of source-drain current vs. gate voltage ( $I_{DS}$  vs.  $V_G$ ) in well-resolved saturation regime,<sup>156,157</sup> and listed in Table 3.4. The average value of TFT mobility was obtained from at least 5 measurements each device. All TFTs show an asymmetric ambipolar transport behavior, as shown in Figure 3.37. Comparison of the mobilities of three GNRs reveals that both the magnitude of hole and electron mobilities is in the order of GNR-An, GNR-Np and GNR-Ph, indicating that the TFT performance increases with increasing the width of nanoribbon.

### 3.3.4 Crystallinity of GNRs

To understand the reason for the width dependence of TFT property, the crystallization of GNRs was measured. The DSC thermogram of GNR-Ph

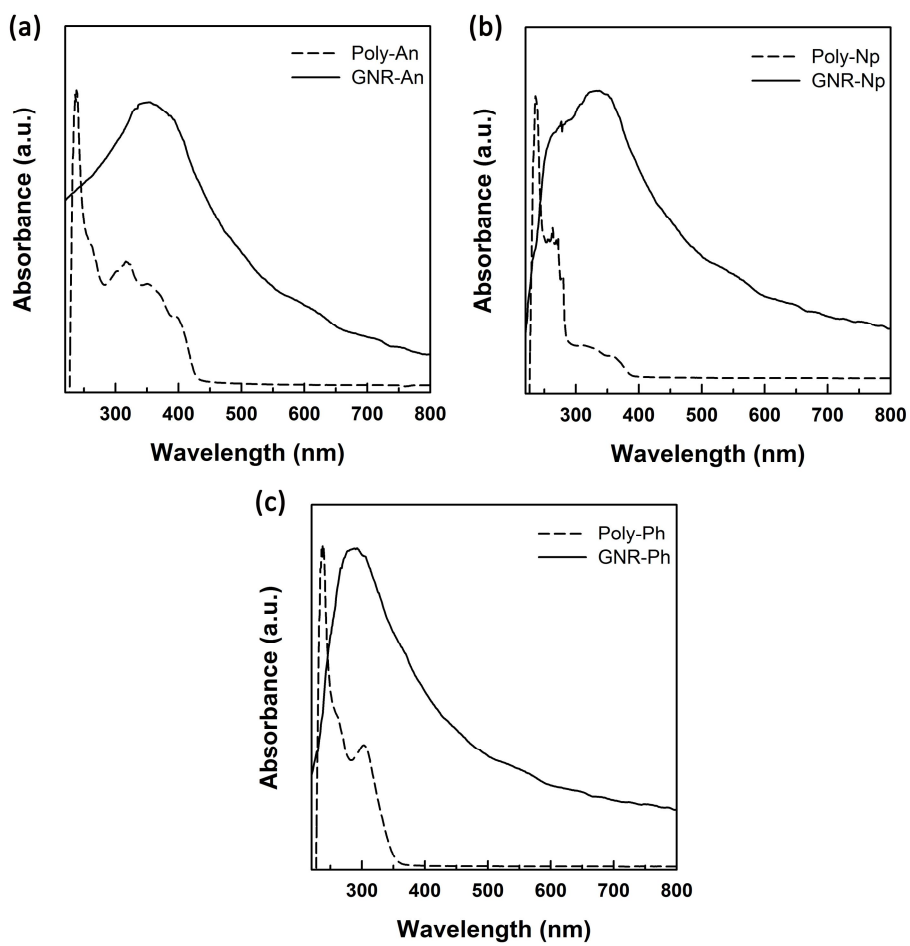


**Figure 3.34.** UV-Vis absorption spectra of (a) Poly-An and GNR-An, (b) Poly-Np and GNR-Np, and (c) Poly-Ph and GNR-Ph.

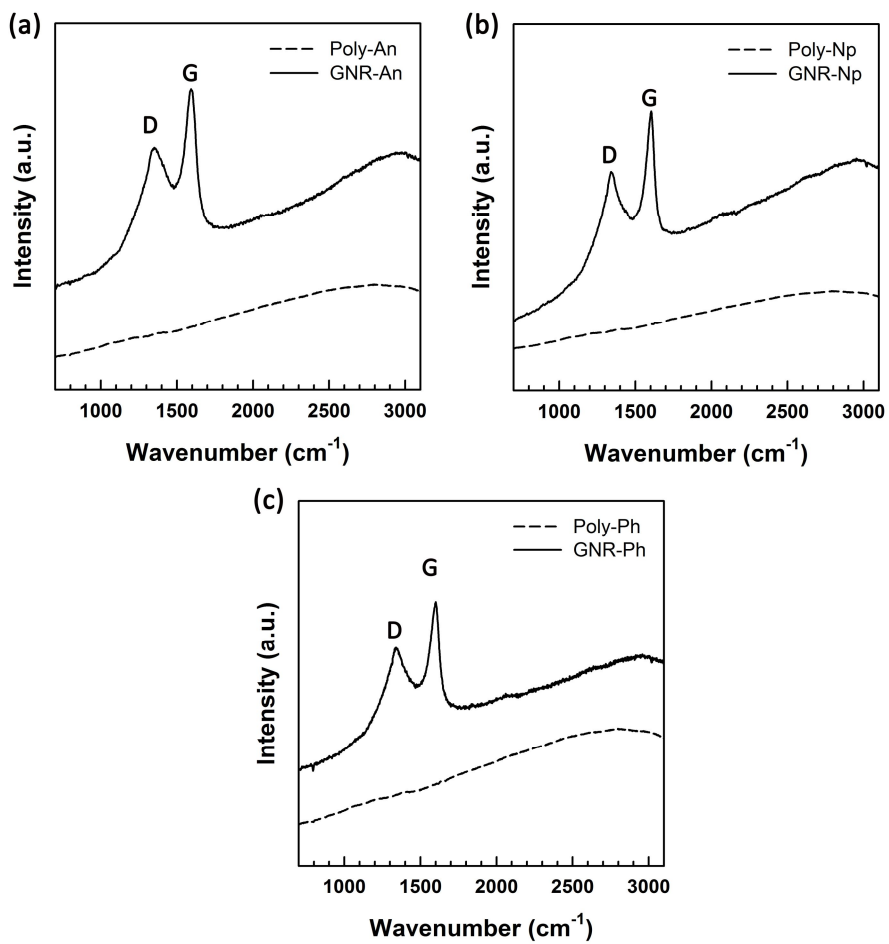


**Figure 3.35.** Raman spectra of (a) Poly-An and GNR-An, (b) Poly-Np and GNR-Np, and (c) Poly-Ph and GNR-Ph.

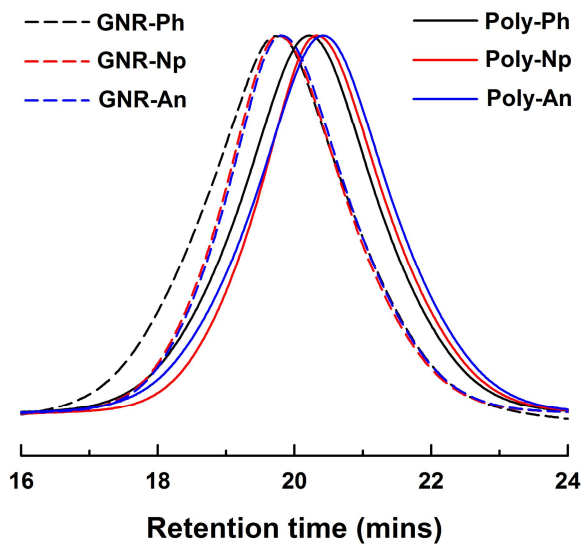


**Figure 3.36.** GPC chromatograms of precursor polymers and GNRs.

**Table 3.4.** Hole and electron mobility of GNRs.

Sample	Mobility ( $\text{cm}^2/\text{V}\cdot\text{s}$ )	
	Hole	Electron
GNR-Ph	$3.81 \times 10^{-3}$	$1.52 \times 10^{-3}$
GNR-Np	$1.83 \times 10^{-2}$	$4.57 \times 10^{-3}$
GNR-An	$3.25 \times 10^{-2}$	$7.11 \times 10^{-3}$

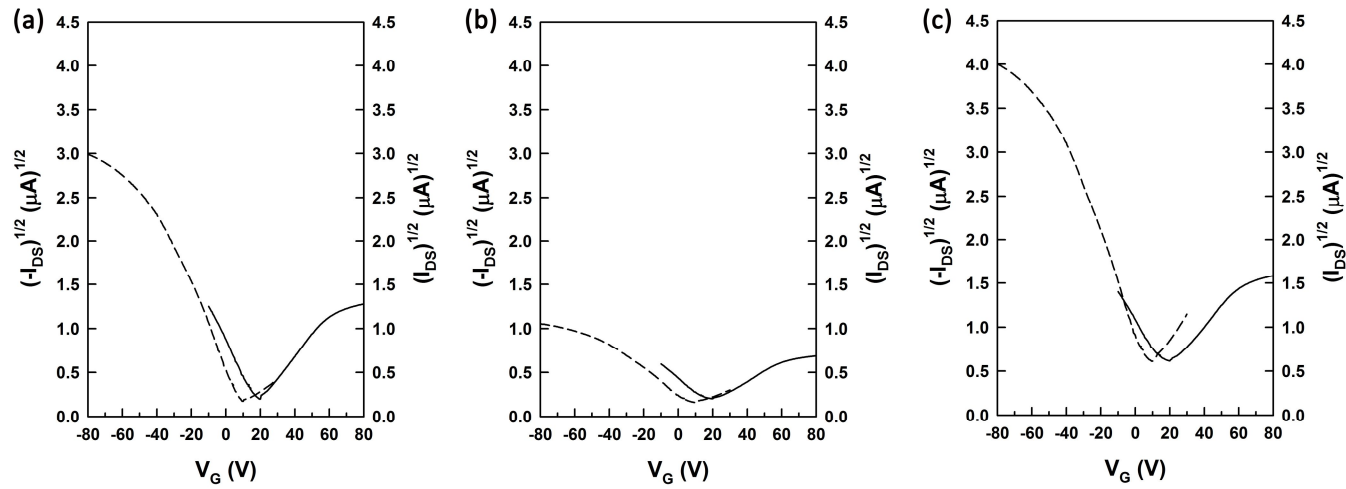


**Figure 3.37.** Transfer curves of field-effect transistor based on (a) GNR-Ph, (b) GNR-Np and (c) GNR-An. Dotted line: transfer curve of current versus gate voltage at positive source-drain bias (+60 V). Solid line: transfer curve of current versus gate voltage at negative source-drain bias (−60 V).

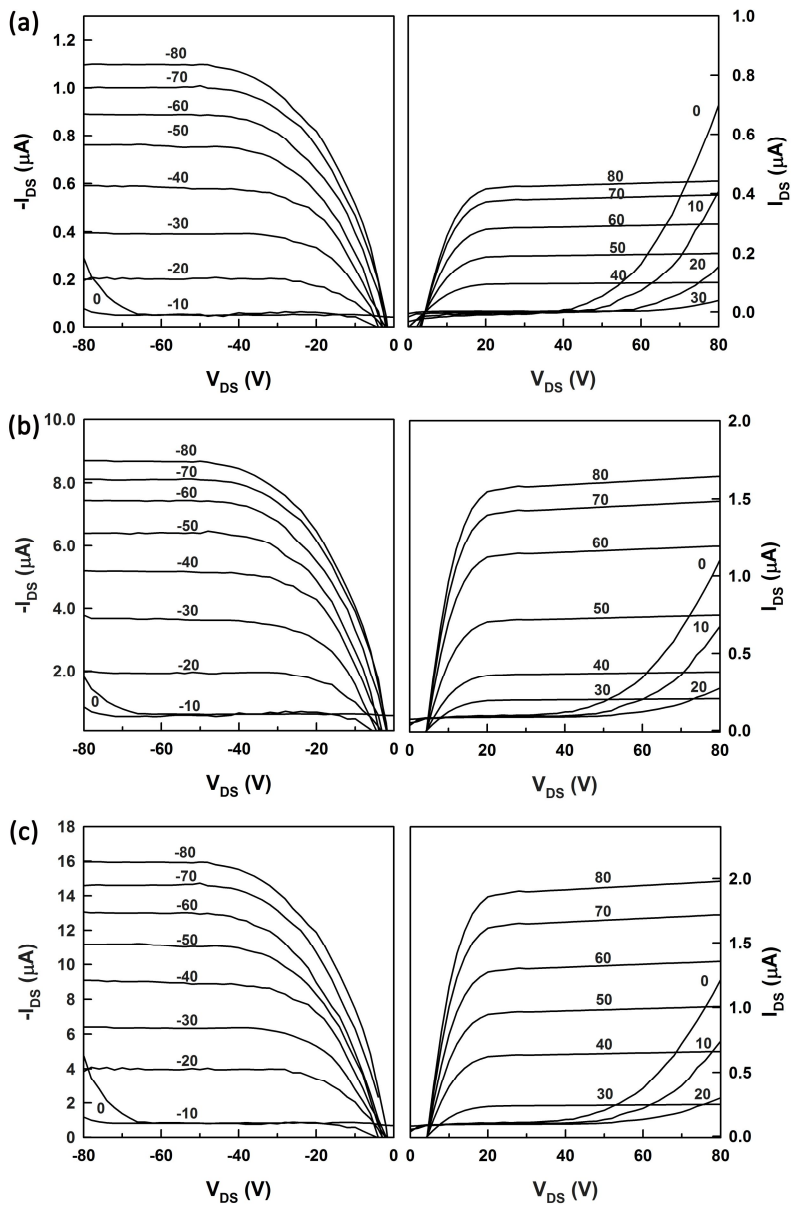


**Figure 3.38.** Output curves of field-effect transistor based on GNR-Ph (a), GNR-Np (b) and GNR-An (c). Left: output curve as a function of gate voltage at negative source-drain bias. Right: output curve as a function of gate voltage at positive source-drain bias.

does not exhibit the melting temperature and crystallization temperature while those of GNR-Np and GNR-An clearly show the melting and crystallization temperature, as shown in Figure 3.39. When the crystal structure was examined by XRD, all GNRs show two diffraction peaks at  $4^\circ$  and  $19^\circ$  corresponding to the (100) and (010) reflections, respectively, as shown in Figure 3.40. Hence, the diffraction peaks at  $4^\circ$  and  $19^\circ$  represent the interchain distance between GNR chains and the face-to-face ( $\pi$ - $\pi$  stacking) distance of aromatic rings in GNRs, respectively. Since XRD of GNR film was measured in out-of-plane direction, the observation of two peaks at  $4^\circ$  and  $19^\circ$  indicates that GNR crystals have both the edge-on and face-on orientation on the substrate, as schematically shown in Figure 3.41. Although it has generally been accepted that the edge-on molecular packing is beneficial for FETs, the previous studies have demonstrated that the face-on orientation also facilitates efficient carrier injection from electrode due to low contact resistance, and as a result exhibits high carrier mobility.<sup>158</sup> Since charge carriers not only travel through the chain axis but also hops through the lamella stacking direction in both the edge-on and face-on orientation, the transport of charge carriers is expected to increase with decrease of the stacking distance. Since the  $\pi$ - $\pi$  stacking distance between GNRs becomes shorter as the width of GNR increases (Table 3.5), indicating that GNR-An molecules are more effectively close-packed than GNR-Ph and GNR-Np, the charge carrier mobility of GNR-An is larger than GNR-Ph and GNR-Np (Table 3.4). But, the interchain distance of GNR-An is larger than those of GNR-Ph and GNR-Np, because the dodecyl group is used as a solubilizing

**Table 3.5.** Interchain and  $\pi$ - $\pi$  stacking distance of GNRs.

Sample	Interchain distance (Å)	$\pi$ - $\pi$ stacking distance (Å)
GNR-Ph	19.55	4.72
GNR-Np	19.55	4.53
GNR-An	21.76	4.38

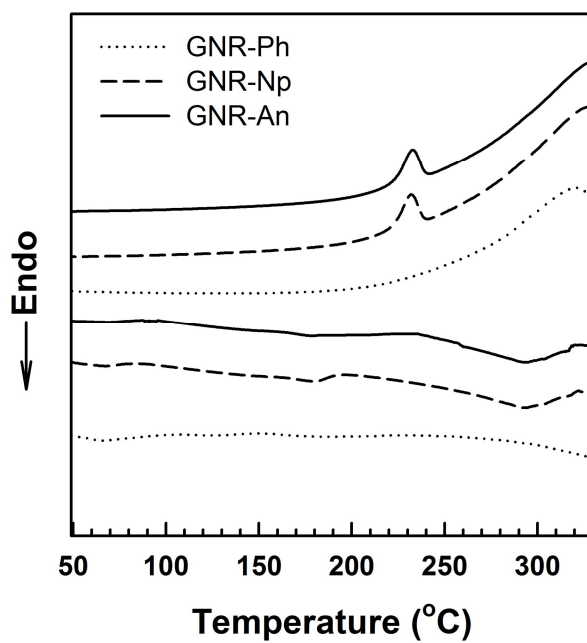


**Figure 3.39.** DSC thermograms of three GNRs.

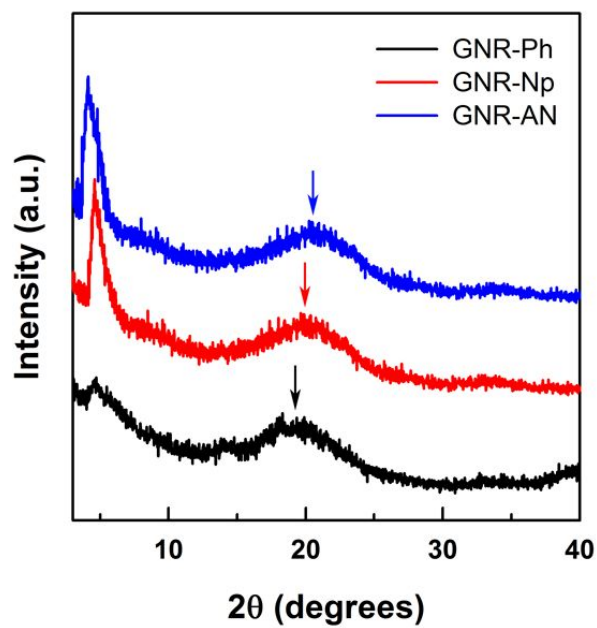


**Figure 3.40.** XRD spectra of three GNRs.

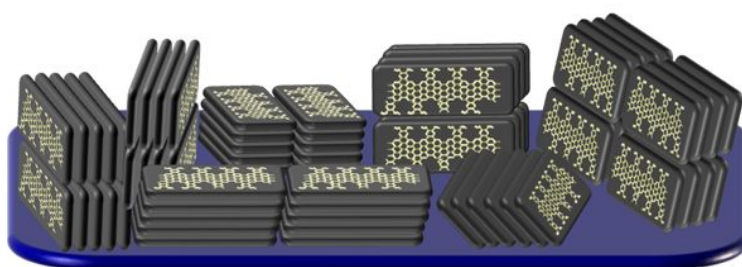


**Figure 3.41.** Schematic representation of GNR-An crystal orientation.

group for GNR-An while hexyl groups are used for GNR-Ph and GNR-Np.

### 3.3.5 Summary

The precursor polymers bearing phenylene, naphthalene and anthracene units synthesized for GNRs by the Suzuki coupling reaction. The polymers were converted into the GNRs through intramolecular cyclodehydrogenation reaction. The degree of conversion from precursor polymer to GNR was determined by NMR analysis. All GNR-based TFTs show ambipolar transport behavior. The GNR-An film exhibits the best TFT performance (a hole mobility of  $3.25 \times 10^{-2} \text{ cm}^2/\text{V}\cdot\text{s}$  and an electron mobility of  $7.11 \times 10^{-3} \text{ cm}^2/\text{V}\cdot\text{s}$ ) among three GNRs due to longer conjugated length, larger width of nanoribbon and better  $\pi$ -stacking structure as compared to GNR-Ph and GNR-Np.

## 3.4 Nitrogen-doped graphene nanoribbon (GNR-N)

### 3.4.1 Synthesis and characterization

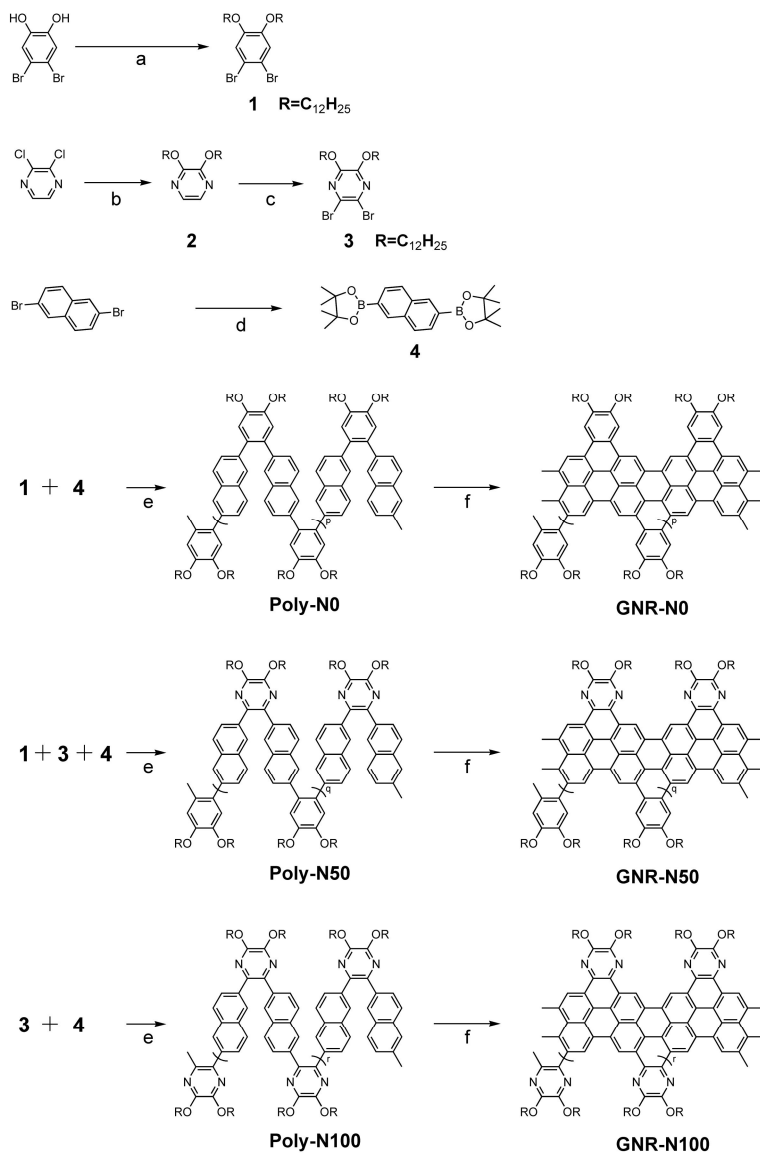
The synthetic routes of GNR-Ns are demonstrated in Scheme 3.4. Three precursor polymers, Poly-N0, Poly-N50 and Poly-N100, were synthesized by the Suzuki coupling between dibrominated pyrazine (or benzene) and diboronated naphthalene. The precursor polymers were then converted into the corresponding GNR-Ns (GNR-N0, GNR-N50 and GNR-N100) through intramolecular cyclodehydrogenation reaction in the presence of FeCl<sub>3</sub> in dichloromethane as an oxidant at room temperature for 3 days. Experimental details for synthesis are described in supporting information. GNR-Ns were very soluble in common solvents such as chloroform and dichlorobenzene owing to long alkoxy groups attached to GNR-N backbone.

The composition of pyrazine and benzene in GNR-N50 was identified by <sup>1</sup>H NMR. Comparing the intensity of pyrazine proton with that of benzene protons in GNR-N50 reveals that the composition ratio of pyrazine to benzene moiety in GNR-N50 is 44:56 (see Figure 3.42). The cyclodehydrogenation of precursor polymer (Poly-N100) was identified by <sup>1</sup>H NMR (Figure 3.43). The average degree of cyclodehydrogenation was determined from the intensity reduction of aromatic protons in GNR-N100 relative to the intensity of the corresponding peaks in Poly-N100 (Figure 3.43). Comparing the relative intensities of aromatic proton peaks of Poly-N100 to the intensity of methylene protons with those of GNR-N100 reveals

that the conversion of the oxidative reaction was 100%. When the degree of cyclodehydrogenations of GNR-N0 and GNR-N50 were determined by the same method as above, the average degrees of cyclodehydrogenation of GNR-N0 and GNR-N50 were also 100%.

### **3.4.2 Identification of cyclodehydrogenation**

When the UV-Vis spectra of GNR-Ns are compared with that of Poly-Ns, as shown in Figure 3.44, all of GNR-Ns exhibit much broader absorption than Poly-Ns. Since the fusion of aromatic rings formed by oxidative reaction increases the conjugation length, it is reasonable to observe that GNR-Ns expand the absorption range to longer wavelength. When the Raman spectra of Poly-Ns and GNR-Ns were measured at 633 nm with He-Ne laser, it reveals that all of GNR-Ns clearly show the first-order D band (disorder band) and G band (graphite band) at  $\sim 1330$  and  $\sim 1600\text{ cm}^{-1}$ , respectively (Figure 3.45), which are consistent with literature values for GNRs, while Poly-Ns do not exhibit the D and G bands. This provides a direct evidence for cyclodehydrogenation of the polymer precursors to form GNR-Ns. It should be noted here that the 2D band was not observed from the Raman spectra of all GNR-Ns, indicating that synthesized GNR-Ns have disorder in c-axis to form turbostratic structures.



**Scheme 3.4.** Synthetic routes of GNR-Ns. a: 1-bromododecane,  $\text{K}_2\text{CO}_3$ , DMF,  $90^\circ\text{C}$ , 24 h; b: 1-dodecanol,  $\text{K}_2\text{CO}_3$ , BTEAC, DMF,  $90^\circ\text{C}$ , 24 h; c:  $\text{Br}_2$ , NaOAc, acetic acid,  $120^\circ\text{C}$ , 12 h; d: bis(pinacolato)diboron,  $\text{PdCl}_2(\text{dppf})$ , KOAc, 1,4-dioxane,  $80^\circ\text{C}$ , 20 h; e:  $\text{K}_2\text{CO}_3$ , Aliquat 336,  $\text{Pd}(\text{PPh}_3)_4$ , toluene,  $\text{H}_2\text{O}$ ,  $160^\circ\text{C}$  (microwave), 12 h; f:  $\text{FeCl}_3$ ,  $\text{CH}_2\text{Cl}_2$ ,  $\text{CH}_3\text{NO}_2$ ,  $30^\circ\text{C}$ , 72 h.

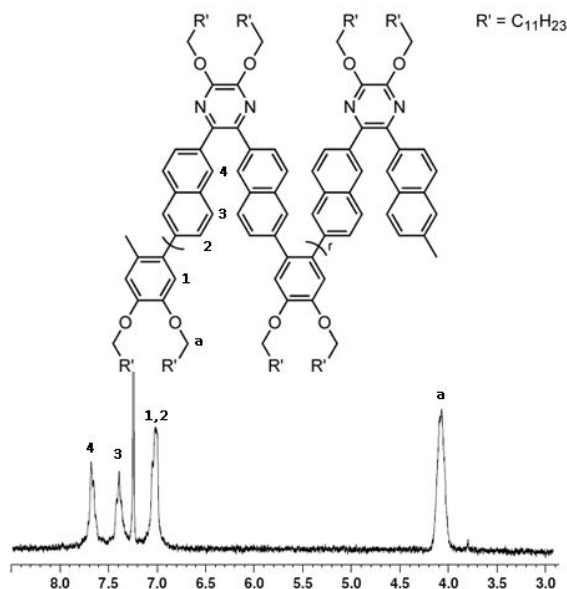


**Figure 3.42.** Chemical structure and <sup>1</sup>H NMR spectra of Poly-N50.

### Calculation of composition from NMR

$4(x+y)=I_a$ , where  $x$  and  $y$  are the number of pyrazine and benzene unit in GNR-Ns, respectively.

$$I_1 = I_{1,2} - I_2, \quad 2y = I_1$$

$$4(x+y) = 2.01, \quad I_1 = 1.56 - I_2 = 1.56 - 1.00 = 0.56, \quad \therefore 2y = 0.56$$

$$y = 0.28, \quad x = 0.22$$

$$\therefore x : y = 11 : 14 = 44 : 56$$

Note:  $I_a=2.01$ ,  $I_{1,2}=1.56$ ,  $I_2=I_3=I_4=1.00$

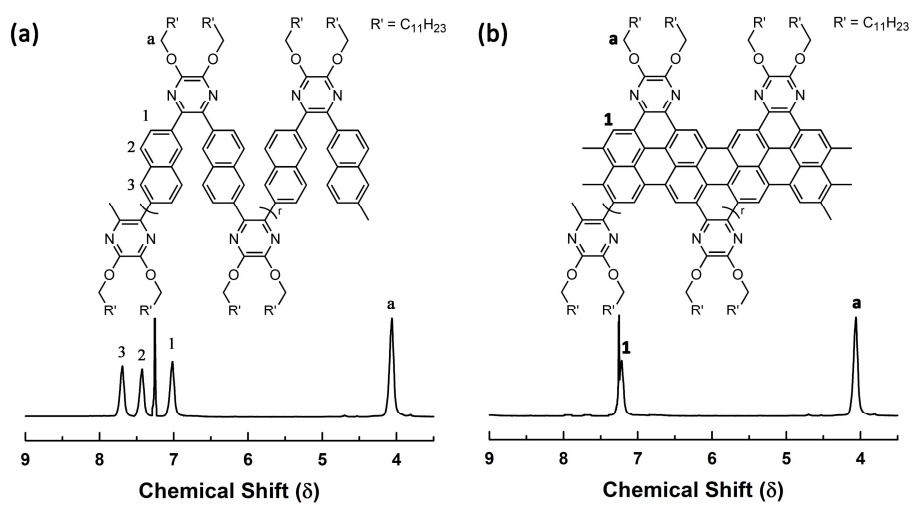


**Figure 3.43.** Chemical structure and  $^1\text{H}$  NMR spectra of (a) Poly-N100 (b) GNR-N100.

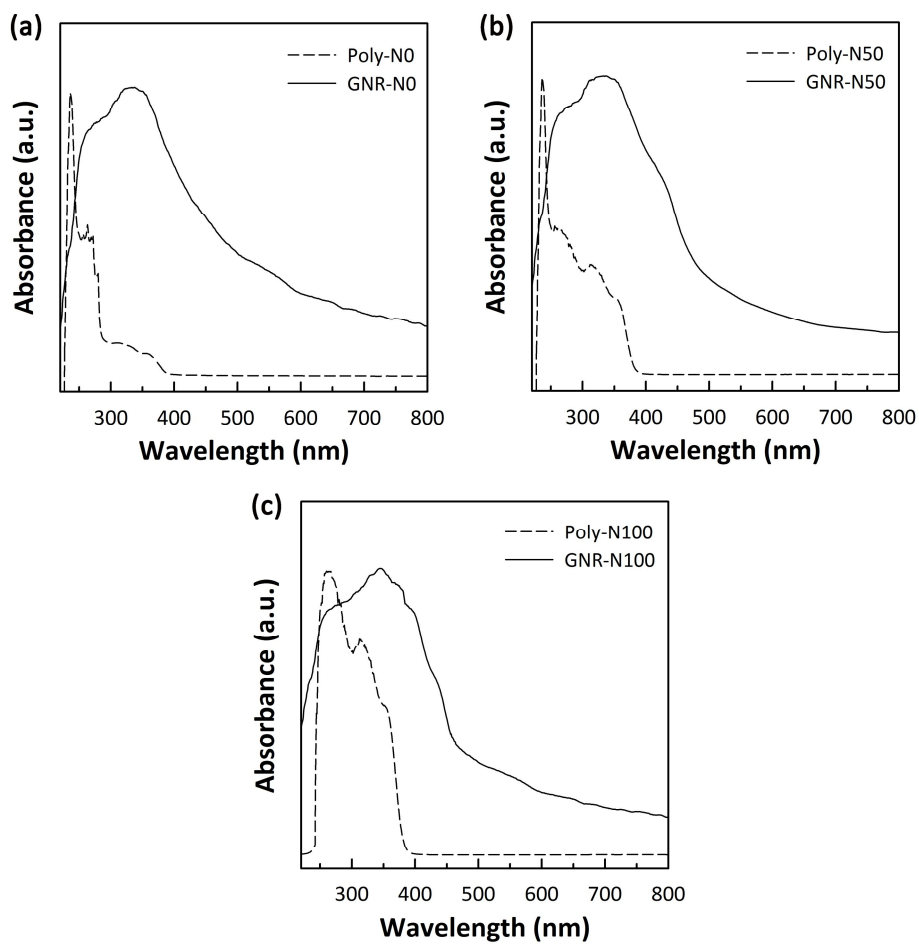


**Figure 3.44.** UV-Vis absorption spectra of (a) Poly-N0 and GNR-N0, (b) Poly-N50 and GNR-N50, and (c) Poly-N100 and GNR-N100.

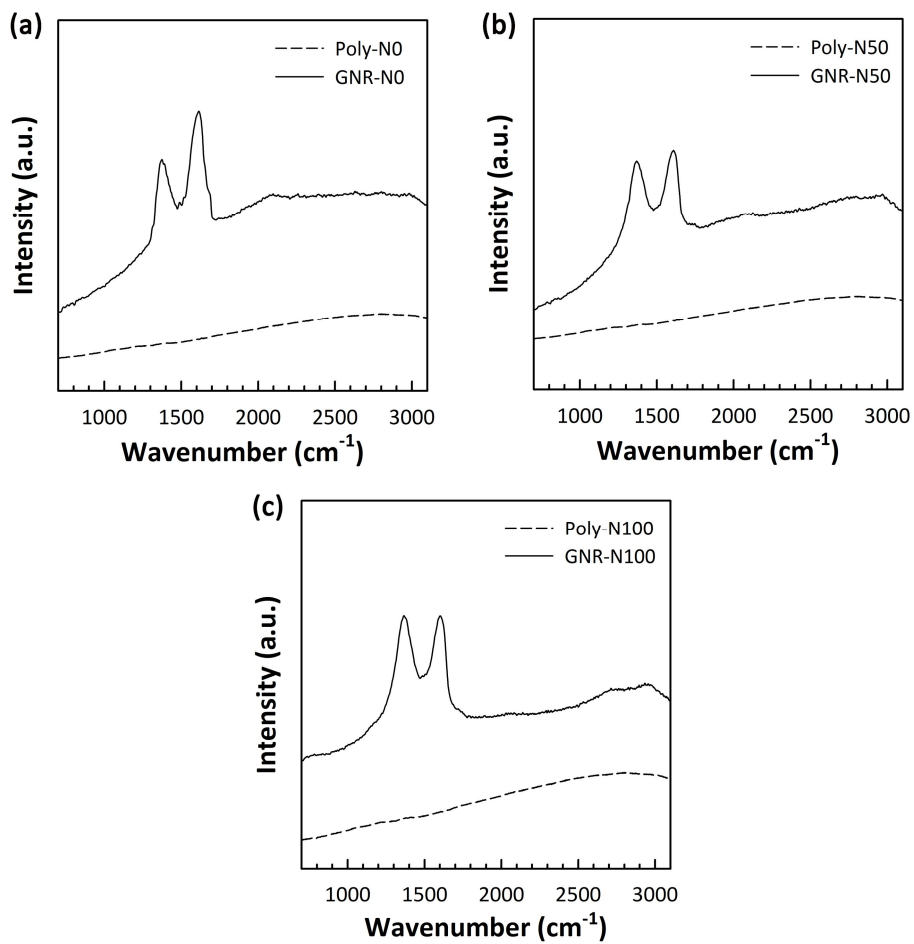


**Figure 3.45.** Raman spectra of (a) Poly-N0 and GNR-N0, (b) Poly-N50 and GNR-N50, and (c) Poly-N100 and GNR-N100.

### 3.4.3 Nitrogen-doping

Electrochemical properties of GNR-Ns are measured by cyclic voltammetry (CV) (Figure 3.46(a)). The HOMO and LUMO energy levels are determined from CV using the equation  $E_{\text{HOMO/LUMO}} = [-(E_{\text{onset}} - 0.38) - 4.8]$  eV, and the results are summarized in Table 3.6. Since nitrogen atom donates its lone pair electrons to the GNRs, the HOMO and LUMO energy levels are lowered as the nitrogen content in GNR-Ns increases. This lowering of the energy levels is in agreement with calculations and experiments on other GNR-Ns.<sup>159,160</sup> It is also observed that the G-band frequency of GNR-Ns in Raman spectrum shifts downwards as the amount of nitrogen doping increases (Figure 3.46(b)). The G band downshift caused by the n-type doping was previously reported in single walled carbon nanotubes and single layer graphene.<sup>160,161</sup> When the crystal structure was examined by XRD, all GNR-Ns show two diffraction peaks at  $4^\circ$  and  $20^\circ$  corresponding to the (100) and (010) reflections (see Figure 3.47), respectively, indicating that the stacking between GNR-Ns has not been interrupted by the substitutional nitrogen doping.

### 3.4.4 TFT performance

For measurement of TFT properties of GNR-Ns, TFT devices with Au source-drain electrode were fabricated. Experimental details for fabrication and characterization of TFT devices are described in experimental section.

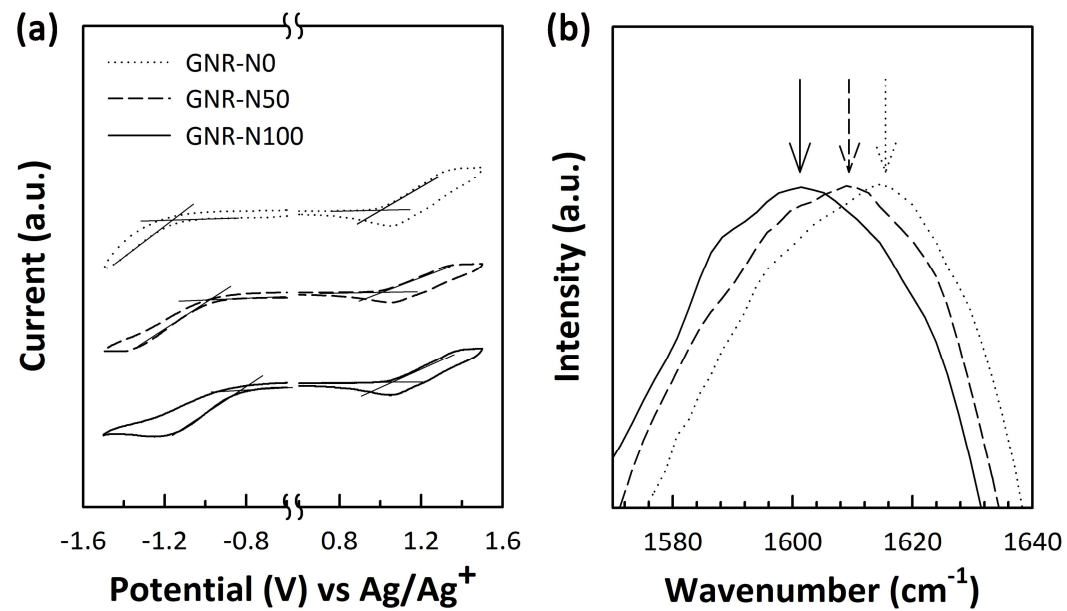


**Figure 3.46.** Cyclic voltammograms (a) and G-band frequency (b) of GNR-N0, GNR-N50 and GNR-N100.

**Table 3.6.** Electrochemical property and charge carrier mobility and threshold voltage of GNR-Ns.

Sample	$E_{\text{HOMO}}$ [eV]	$E_{\text{LUMO}}$ [eV]	Mobility [ $\text{cm}^2/\text{V}\cdot\text{s}$ ]		Threshold voltage [V]
			Hole	Electron	
GNR-N0	5.42	3.26	$2.92 \times 10^{-2}$	$4.94 \times 10^{-3}$	20
GNR-N50	5.46	3.43	$7.87 \times 10^{-3}$	$2.09 \times 10^{-2}$	7
GNR-N100	5.50	3.57	$3.12 \times 10^{-3}$	$1.02 \times 10^{-1}$	-6

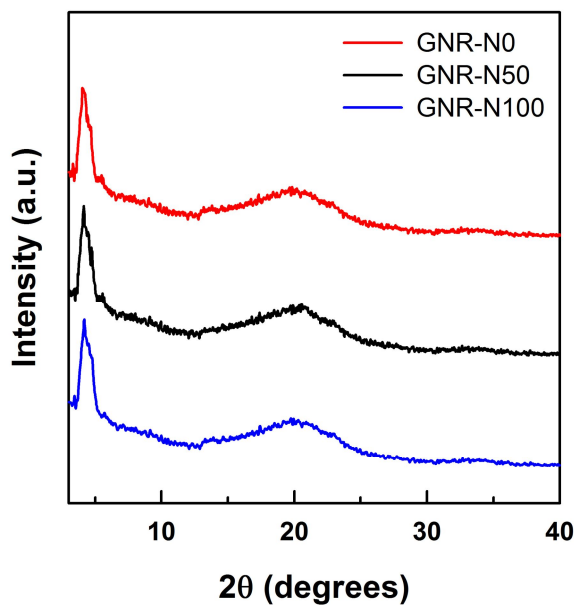


**Figure 3.47.** XRD spectra of three GNR-Ns.

Figure 3.48 compares the TFT performances of GNR-N0, GNR-N50 and GNR-N100. The carrier mobility was evaluated from the transfer curve of source-drain current *vs.* gate voltage ( $I_{DS}$  *vs.*  $V_G$ ) in well-resolved saturation regime, and listed in Table 3.6. The average value of TFT mobility was obtained from at least 10 measurements each device. The hole mobility of GNR-N decreases while the electron mobility increases, as the nitrogen content in GNR-Ns increases, indicating that the charge transport behavior of GNR-Ns is changed from ambipolar to *n*-type semiconductor. Particularly, the electron mobility of GNR-N100 is two orders of magnitude higher than that of GNR-N0. Furthermore, the threshold voltage of GNR-Ns is changed from +20 V to -6 V by nitrogen doping in GNR.

### 3.4.5 Summary

GNR-Ns with different amounts of nitrogen doping were successfully synthesized by a bottom-up method. The degree of nitrogen doping was controlled by changing the monomer feed ratio of pyrazine to benzene for polymerization. The degree of cyclodehydrogenation and the amount of nitrogen doping in GNR-Ns were identified quantitatively by NMR analysis. The electron mobility of GNR-N increases with increasing the amount of nitrogen doping in GNR-Ns and the threshold voltage of GNR-Ns shifts from +20 V to -6 V, indicating that the charge transport behavior of GNR-Ns is changed from ambipolar to *n*-type as the amount of nitrogen doping

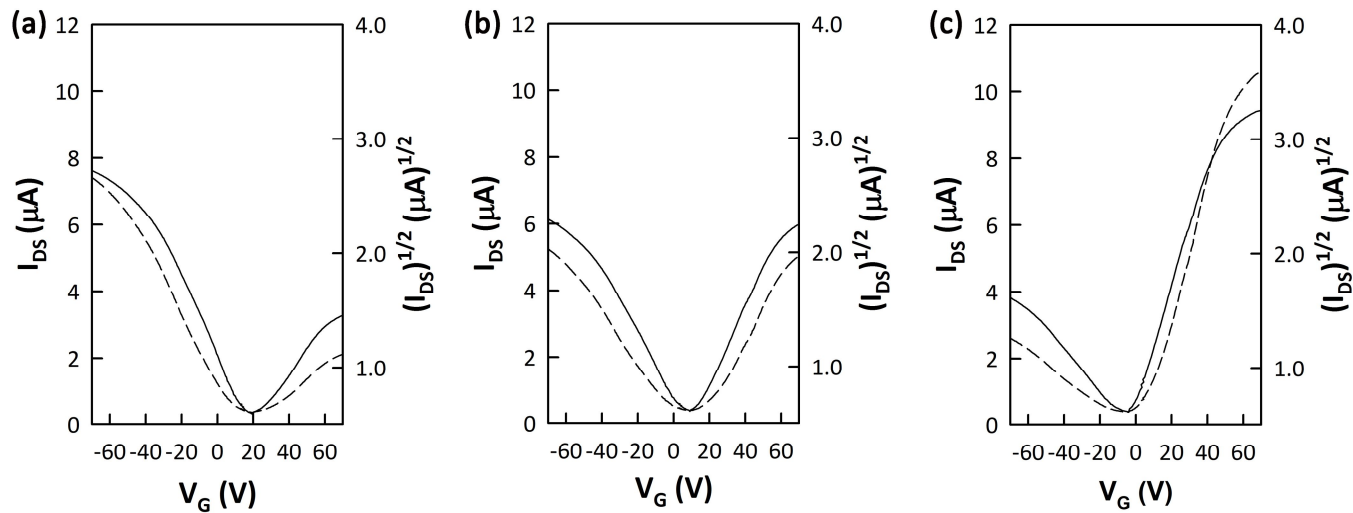


**Figure 3.48.** Transfer curves of field-effect transistor based on (a) GNR-N0, (b) GNR-N50 and (c) GNR-N100. The drain-source voltage for transfer characteristics was  $-60$  V and the field effect mobility ( $\mu$ ) was measured from the transfer curve in the saturation regime and calculated from the gradient of transfer curve.

increases in GNR-Ns. Particularly, the electron mobility of GNR-N100 ( $0.102 \text{ cm}^2/\text{V}\cdot\text{s}$ ) is two orders of magnitude higher than that of GNR-N0.

## **3.5 Graphene electrode for supercapacitor**

### **3.5.1 Exfoliation of graphene**

PANI strongly physisorb onto the graphene surface via strong  $\pi$ - $\pi$  interaction and store energy using redox reaction and PSSA enhance the solubility of graphene in water and self-dope the PANI in PSSA-g-PANI, indicating that PSSA-g-PANI easily non-covalent functionalize graphene, and enhance the solubility and processability, as shown in Figure 2.2. Figure 3.49 compares UV-Vis absorption spectra of graphite, PSSA-g-PANI and PSSA-g-PANI/graphene. The UV-Vis absorption spectrum of graphite without the PSSA-g-PANI shows that the light of whole wavelength is transmittance. While the UV-Vis absorption spectrum of PSSA-g-PANI/graphene exhibits larger absorbance than of PSSA-g-PANI, indicating that the graphene was exfoliated and dispersed in water by PSSA-g-PANI. After sonication and centrifugation of PSSA-g-PANI/graphite solution, the average diameter of exfoliated graphene from graphite is  $\sim 500$  nm and the average number of graphene layer is 4~5 layers, as shown in Figure 3.50.

### **3.5.2 Capacitance**

To evaluate the properties of PSSA-g-PANI/graphene composite as an electrode material for supercapacitors, the CV profile were obtained for the voltage sweeps from 0 to 0.8 V (see Figure 3.51 and 3.52) with a series of

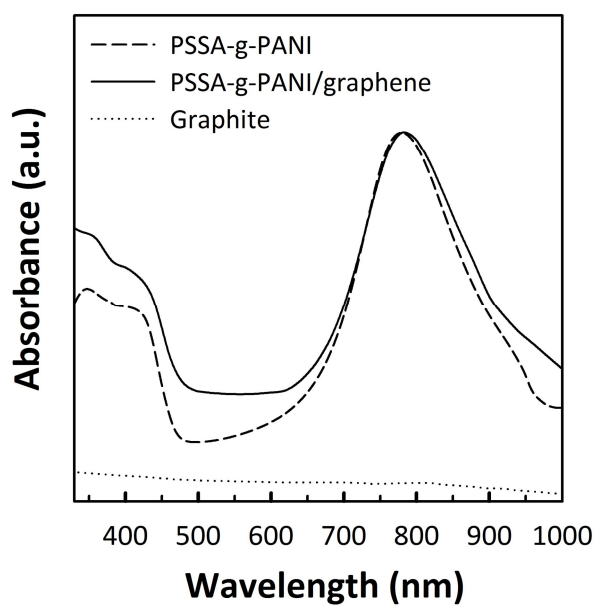


**Figure 3.49.** UV-Vis absorption spectra of graphite, PSSA-g-PANI and PSSA-g-PANI/graphene solutions.

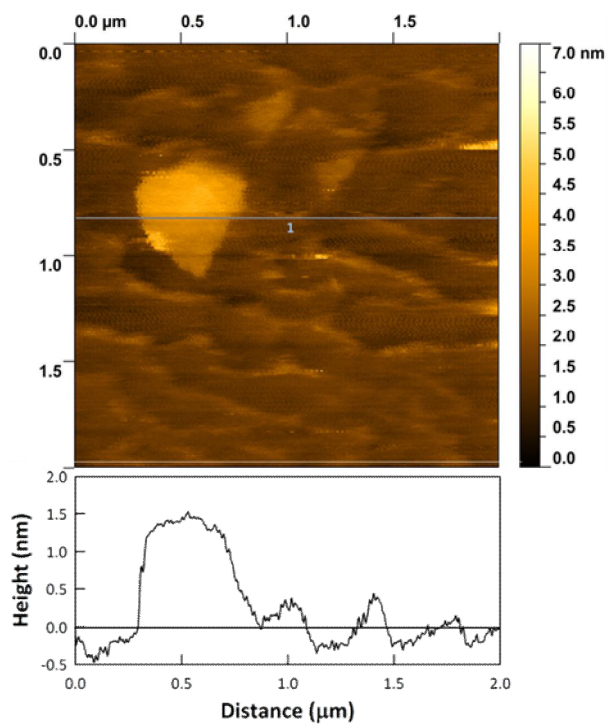


**Figure 3.50.** AFM image and height profile of exfoliated graphene.

scan rate from 10 to 100 mV/s. The electrochemical property of four kinds of PSSA-g-PANI/graphene composites was measured to identify effect with different length of PSSA and PANI on capacitance, and listed in Table 3.7. All PSSA-g-PANI/graphene composite are nearly rectangular in shape, indicating that they behave as EDLC type supercapacitor. The COMP#2 electrode gave a specific capacitance up to 335 F/g at a scan rate of 50 mV/s, which is the highest value in four PSSA-g-PANI/graphene composites. The PSSA-g-PANI in COMP#4, which have small amount of grafting site and long PANI length, easily exfoliated graphene from graphite and effectively disperse graphene in water. Also, the capacitance retention of the PSSA-g-PANI/graphene composite after 5000 cycles is found to be value 78% (see Figure 3.53).

### **3.5.3 Summary**

The water-soluble conducting polymer, PSSA-g-PANI, directly exfoliate graphenes from graphite and disperse graphene in water. PSSA-g-PANI/graphene composite films for supercapacitor electrode were fabricated by solution process. The capacitance of PSSA-g-PANI/graphene composites was affected as a length of PANI and PSSA, and the highest capacitance among PSSA-g-PANI/graphene composites is 335 F/g at a scan rate of 50 mV/s and 78% retention of capacitance after 5000 cycles.

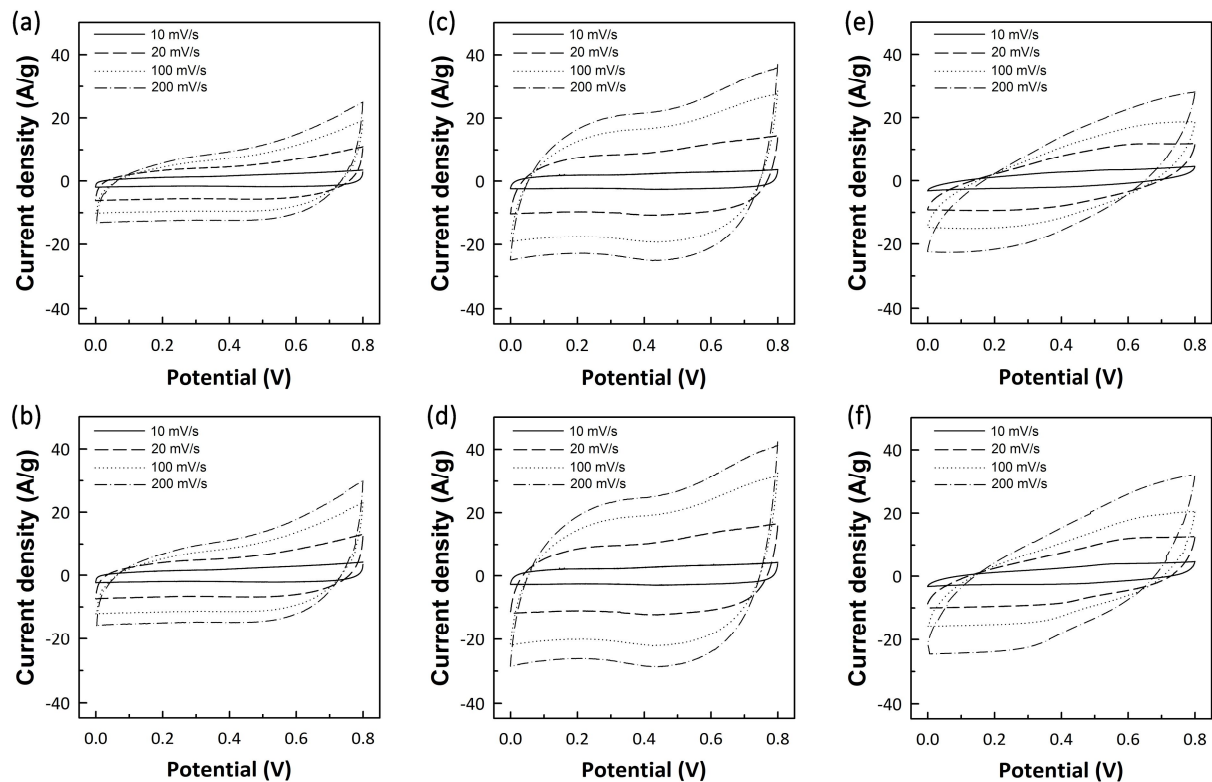


**Figure 3.51.** Cyclic voltammograms of PSSA-g-PANI/graphene composites: (a) COMP#1-1; (b) COMP#1-2; (c) COMP#2-1; (d) COMP#2-2; (e) COMP#3-1; (f) COMP#3-2.

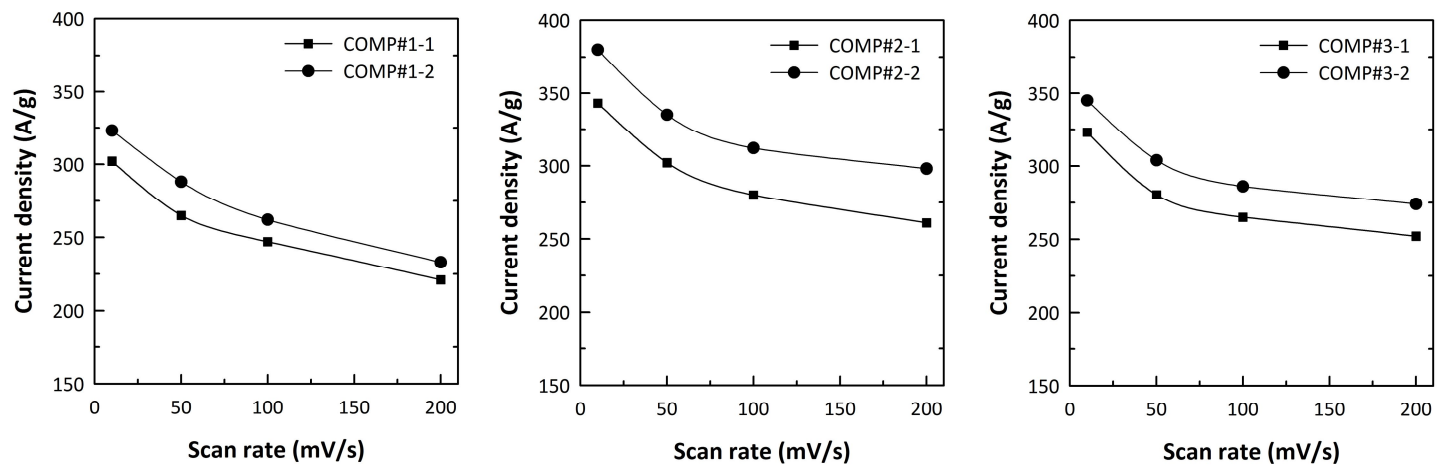


Figure 3.52. Specific capacitance with scan rate.

**Table 3.7.** Characteristic of PSSA-g-PANI and capacitance of composites.

Sample	PSSA-g-PANI		Specific capacitance <sup>b</sup> (F/g)
	SSA:AMS <sup>a</sup>	ANI/SSA	
COMP#1-1	15:1	0.3	265
COMP#1-2	15:1	0.5	288
COMP#2-1	20:1	0.3	302
COMP#2-2	20:1	0.5	335
COMP#3-1	25:1	0.3	280
COMP#3-2	25:1	0.5	303

<sup>a</sup> AMS is grafting site.

<sup>b</sup> scan rate is 50 mV/s

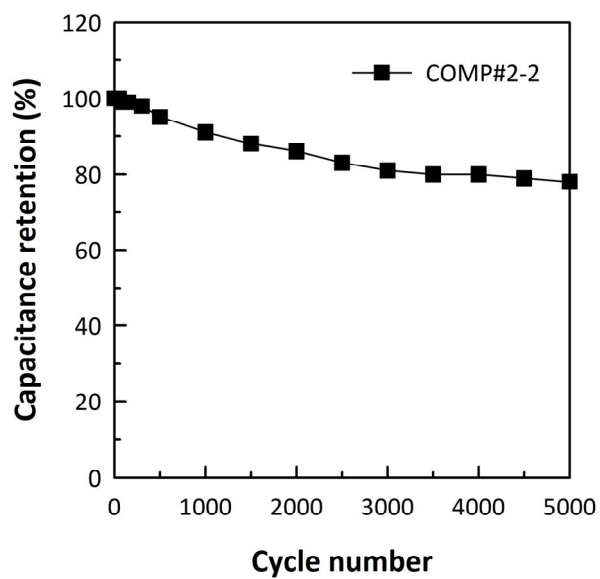


Figure 3.53. Cyclic performance of COMP#2-2.

## Chapter 4. Conclusions

Solution processable CNTs and graphene were synthesized and functionalized for composite, TFT and supercapacitor electrode, investigated their mechanical and electrical properties.

First, non-covalently functionalized MWCNTs were fabricated for polymer/MWCNT composite. One of the most widely used approaches for effective dispersion of CNTs in polymer matrix is to modify the surface of CNTs by introducing functional groups covalently on the surface of CNTs. Non-covalent functionalization avoids the destruction of the chemical structure of CNTs and thus improves the interfacial property between CNTs and polymer matrix without sacrifice of excellent mechanical and electrical properties of CNTs. Among various types of compatibilizer using non-covalent functionalization, block or graft copolymers have been used as effective compatibilizers for polymer/CNT composites. If the main chain in graft copolymer can interact with CNTs by  $\pi$ - $\pi$  interactions while the graft chain is miscible with matrix polymer, it is expected that CNTs are well dispersed in polymer matrix without sacrifice of excellent properties of CNTs. With keeping this in mind, in this study, two compatibilizers were synthesized, and they are used to polymer/MWCNT composites. When a small amount of the compatibilizers were added to polymer/MWCNT composites, the mechanical and electrical conductivity of the composites were increased as compared with those of the composites without

compatibilizer. The improved mechanical properties and electrical conductivity of composites containing compatibilizer are attributed to both homogeneous dispersion of MWCNTs in polymer matrices and good interfacial adhesion between polymer matrices and MWCNTs functionalized non-covalently with the compatibilizer. Consequently, the structure of compatibilizer is changeable with polymer matrix, indicating that the method using compatibilizer easily functionalizes CNTs and fabricates high performance polymer/CNT composite through solution-process.

Second, the GNRs were fabricated by bottom-up organic synthesis for semiconducting material of TFT. Although graphene itself is a zero-band-gap semi-metal, GNRs with a widths smaller than 10 nm exhibits semiconducting behavior that allows us to use them for active materials of electronic devices. In several methods for fabrication of GNRs, bottom-up organic synthesis of carbon nanomaterial is expected to control its structure on the atomic scale and thus enables chemists to reach their goal of synthesizing well-defined carbon nanomaterials. For fabrication of GNRs, precursor polymers were synthesized for GNRs by bottom-up method and then the polymers were converted into the GNRs through intramolecular cyclodehydrogenation reaction. All GNR-based TFTs show ambipolar transport behavior. The GNR-An film exhibits the best TFT performance among three GNRs due to longer conjugated length, larger width of nanoribbon and better  $\pi$ -stacking structure as compared to GNR-Ph and GNR-Np.

Another advantage of the bottom-up approach is to control electronic

properties of GNRs. One of the most feasible approaches to control the electronic properties of graphene is chemical doping by incorporation of heteroatoms (e.g., boron, nitrogen) into graphitic framework. This method can not only alter the band structure but also generate specific charge carrier (hole or electron). In order to examine the effect of nitrogen doping on GNRs, GNR-Ns with different amounts of nitrogen doping were synthesized by a bottom-up method. The electron mobility of GNR-N increases with increasing the amount of nitrogen doping in GNR-Ns and the charge transport behavior of GNR-Ns is changed from ambipolar to n-type. Particularly, the electron mobility of GNR-N100 is two orders of magnitude higher than that of GNR-N0. According to these results, solution processable GNRs are easily fabricated by bottom-up synthesis and their electrical property is tuned by doping.

Finally, graphene was directly exfoliated from graphite by water-soluble conducting polymer for supercapacitor electrode material. Due to their unique 2D structure and outstanding intrinsic physical properties, such as extraordinarily high electrical conductivity and large surface area, graphene-based materials exhibit great potential for application in supercapacitors. Also, development of the solution processable electrode material for high performance and various shape supercapacitor was highly demanded in accordance with the expansion of supercapacitor application from memory devices to electric vehicles. To develop the high performance and solution processable graphene-based supercapacitor electrode, graphenes were directly exfoliated from graphite by PSSA-g-PANI. The capacitance of

PSSA-g-PANI/graphene composites was affected as a length of PANI and PSSA, and the highest capacitance among PSSA-g-PANI/graphene composites is 335 F/g at a scan rate of 50 mV/s and 78% retention of capacitance after 5000 cycles. Consequently, the solution processable graphenes are directly exfoliated by water soluble conducting polymer and they are promising candidate for high performance supercapacitor electrode.

## Bibliography

- (1) Ajayan, P. M. *Chem. Rev.* **1999**, *99*, 1787.
- (2) Kroto, H. W. *Nature* **1987**, *329*, 529.
- (3) Campbell, E. E. B.; Fowler, P. W.; Mitchell, D.; Zerbetto, F. *Chem. Phys. Lett.* **1996**, *250*, 544.
- (4) Taylor, R.; Walton, D. R. M. *Nature* **1993**, *363*, 685.
- (5) Johnson, R. D.; Meijer, G.; Bethune, D. S. *J. Am. Chem. Soc.* **1990**, *112*, 8983.
- (6) Johnson, R. D.; Bethune, D. S.; Yannoni, C. S. *Acc. Chem. Res.* **1992**, *25*, 169.
- (7) Kroto, H. W.; Heath, J. R.; O'Brien, S. C. O.; Curl, R. F.; Smalley, R. E. *Nature* **1985**, *318*, 162.
- (8) Bethune, D. S.; Johnson, R. D.; Salem, J. R.; de Vries, M. S.; Yannoni, C. S. *Nature* **1993**, *366*, 123.
- (9) Kessler, B.; Bringer, A.; Cramm, S.; Schlebusch, C.; Eberhardt, W. *Phys. Rev. Lett.* **1997**, *79*, 2289.
- (10) Shinohara, H.; Sato, H.; Saito, Y. *J. Phys. Chem.* **1991**, *95*, 8449.
- (11) Ugarte, D. *Nature* **1992**, *359*, 707.
- (12) Fortner, J. D.; Lyon, D. Y.; Sayes, C. M.; Boyd, A. M.; Falkner, J. C.; Hotze, E. M.; Alemany, L. B.; Tao, Y. J.; Guo, W.; Ausman, K.

- D.; Colvin, V. L.; Hughes, J. B. *Environ. Sci. Technol.* **2005**, *39*, 4307.
- (13) Chen, K. L.; Elimelech, M. *Langmuir* **2006**, *22*, 10994.
- (14) Serivens, W. A.; Tour, J. M. *J. Am. Chem. Soc.* **1994**, *116*, 4517.
- (15) Duncan, L. K.; Jinschek, J. R.; Vikesland, P. J. *Environ. Sci. Technol.* **2008**, *42*, 173.
- (16) Brant, J. A.; Labille, J. Bottero, J. Y.; Wiesner, M. R. *Langmuir* **2006**, *22*, 3878.
- (17) Chen, K. L.; Elimelech, M. *J. Colloid Interface Sci.* **2007**, *309*, 126.
- (18) Iijima, S. *Nature* **1991**, *354*, 56.
- (19) Iijima, S.; Ichihashi, T. *Nature* **1993**, *363*, 603.
- (20) Thess, A.; Lee, R.; Nikolaev, P.; Dai, H.; Petit, P.; Robert, J.; Xu, C.; Lee, Y. H.; Kim, S. G.; Rinzler, A. G.; Colbert, D. T.; Scuseria, G. E.; Tománek, D.; Fischer, J. E.; Smalley, R. E. *Science* **1996**, *273*, 483.
- (21) Guo, T.; Nikolaev, P.; Rinzler, A. G.; Tománek, D.; Colbert, D. T.; Smalley, R. E. *J. Phys. Chem.* **1995**, *99*, 10694.
- (22) Guo, T.; Nikolaev, P.; Thess, A.; Colbert, D. T.; Smalley, R. E. *Chem. Phys. Lett.* **1995**, *243*, 49.
- (23) Li, W. Z.; Xie, S. S.; Qian, L. X.; Chang, B. H.; Zou, B. S.; Zhou, W. Y.; Zhao, R. A.; Wang, G. *Science*. **1996**, *274*, 1707.

- (24) Hata, K.; Futada, D. N.; Mizuno, K.; Namai, T.; Yumura, M.; Iijima, S. *Science*. **2004**, *306*, 1362.
- (25) Talapatra, S.; Kar, S.; Pal, S. K.; Vajtai, R.; Ci, L.; Victor, P.; Shaijumon, M. M.; Kaur, S.; Nalamasu, O.; Ajayan, P. M. *Nat. Nanotechnol.* **2006**, *1*, 112.
- (26) Satishkumar, B. C.; Govindaraj, A.; Sen, R.; Rao, C. N. R. *Chem. Phys. Lett.* **1998**, *293*, 47.
- (27) Sen, R.; Govindaraj, A.; Rao, C. N. R. *Chem. Mater.* **1997**, *9*, 2078.
- (28) Nikolaev, P.; Bronikowski, M. J.; Bradley, K.; Rohmund, F.; Colbert, D. T.; Smith, K. A.; Smalley, R. E. *Chem. Phys. Lett.* **1999**, *313*, 91.
- (29) Novoselov, K. S.; Geim, A. K.; Morozov, S. V.; Jiang, D.; Zhang, Y.; Dubonos, S. V.; Grigorieva, I. V.; Firsov, A. A. *Science*. **2004**, *306*, 666.
- (30) Jiang, Z.; Zhang, Y.; Stormer, H. L.; Kim, P. *Phys Rev. Lett.* **2007**, *99*, 106802.
- (31) Novoselov, K. S.; Jiang, Z.; Morozov, S. V.; Stormer, H. L.; Zeitler, U.; Maan, J. C.; Boebinger, G. S.; Kim, P.; Geim, A. K. *Science* **2007**, *315*, 1379.
- (32) Novoselov, K. S.; Geim, A. K.; Morozov, S. V.; Jiang, D.; Katsnelson, M. I.; Grigorieva, I. V.; Dubonos, S. V.; Firsov, A. A. *Nature* **2005**, *438*, 197.

- (33) Schedin, F.; Geim, A. K.; Morozov, S. V.; Hill, E. W.; Blake, P.; Katsnelson, M. I.; Novoselov, K. S. *Nat. Mater.* **2007**, *6*, 652.
- (34) Stankovich, S.; Dikin, D. A.; Dommett, H. B.; Kohlhaas, K. M.; Zimney, E. J.; Stach, E. A.; Piner, R. D.; Nguyen, S. T.; Ruoff, R. S. *Nature* **2006**, *442*, 282.
- (35) Stankovich, S.; Piner, R. D.; Chen, X.; Wu, N.; Nguyen, N.; Nguyen, S. T.; Ruoff, R. S. *J. Mater. Chem.* **2006**, *16*, 155.
- (36) Stankovich, S.; Dikin, D. A.; Piner, R. D.; Kohlhaas, K. A.; Kleinhammes, A.; Jia, Y.; Wu, Y.; Nguyen, S. T.; Ruoff, R. S. *Carbon* **2007**, *45*, 1558.
- (37) Yang, X.; Rouhanipour, A.; Zhi, L.; Räder, H. J.; Müllen, K. *J. Am. Chem. Soc.* **2008**, *130*, 4216.
- (38) Wu, J.; Pisula, W.; Müllen, K. *Chem. Rev.* **2007**, *107*, 718.
- (39) Berger, C.; Song, Z.; Li, T.; Li, X.; Ogbazghi, A. Y.; Feng, R.; Dai, Z.; Marchenkov, A. N.; Conrad, E. H.; First, P. N.; de Heer, W. A. *J. Phys. Chem. B* **2004**, *108*, 19912.
- (40) Berger, C.; Song, Z.; Li, X.; Wu, X.; Brown, N.; Naud, C.; Mayou, D.; Li, T.; Hass, J.; Marchenkov, A. N.; Conrad, E. H.; First, P. N.; de Heer, W. A. *Science* **2006**, *312*, 1191.
- (41) Reina, A.; Jia, X.; Ho, J.; Nezich, D.; Son, H.; Bulovic, V.; Dresselhaus, M. S.; Kong, J. *Nano Lett.* **2009**, *9*, 30.
- (42) Sutter, P. W.; Flege, J. I.; Sutter, E. A. *Nat. Mater.* **2008**, *7*, 406.

- (43) Gómez-Navarro, C.; Weitz, R. T.; Bittner, A. M.; Scolari, M.; Mews, A.; Burghard, M.; Kern K. *Nano Lett.* **2007**, *7*, 3499.
- (44) Wu, J.; Gherghel, L.; Watson, M. D.; Li, J.; Wang, Z.; Simpson, C. D.; Kolb, U.; Müllen, K. *Macromolecules* **2003**, *36*, 7082.
- (45) Kam, N. W. S.; Liu, Z.; Dai, H. *J. Am. Chem. Soc.* **2005**, *127*, 12492.
- (46) Shim, M.; Kam, N. W. S.; Chen, R. J.; Li, Y.; Dai, H. *Nano Lett.* **2002**, *2*, 285.
- (47) Holzinger, M.; Vostrowsky, O.; Hirsch, A.; Hennrich, F.; Kappes, M.; Weiss, R.; Jellen, F. *Angew. Chem. Int. Ed.* **2001**, *40*, 4002.
- (48) Georgakilas, V.; Kordatos, K.; Prato, M.; Guldi, D. M.; Holzinger, M.; Hirsch, A. *J. Am. Chem. Soc.* **2002**, *124*, 760.
- (49) Bacon, R. *J. Appl. Phys.* **1960**, *31*, 283.
- (50) Lu, J. P. *J. Phys. Chem. Solids* **1997**, *58*, 1649.
- (51) Poncharal, P.; Wang, Z. L.; Ugarte, D.; de Heer, W. A. *Science* **1999**, *283*, 1513.
- (52) Falvo, M. R.; Clary, G. J.; Taylor, R. M.; Chi, V.; Brooks, Jr F. P.; Washburn, S.; Superfine, R. *Nature* **1997**, *389*, 582.
- (53) Salvétat, J. P.; Kulik, A. J.; Bonard, J. M.; Briggs, A. D.; Stöckli, T.; Méténier, K.; Bonnamy, S.; Béguin, F.; Burnham, N. A.; Forró, L. *Adv. Mater.* **1999**, *11*, 161.
- (54) Avouris, P. *Chem. Phys.* **2002**, *281*, 429.

- (55) Kong, J.; Zhou, C.; Morpurgo, A.; Soh, H. T.; Quate, C. F.; Marcus, C.; Dai, H. *Appl. Phys. A* **1999**, *69*, 305.
- (56) Bryning, M. B.; Islam, M. F.; Kikkawa, J. M.; Yodh, A. G. *Adv. Mater.* **2005**, *17*, 1186.
- (57) Ajayan, P. M.; Stephan, O.; Colliex, C.; Trauth, D. *Science* **1994**, *265*, 1212.
- (58) Jin, L.; Bower, C.; Zhou, O. *Appl. Phys. Lett.* **1998**, *73*, 1197.
- (59) Shaffer, M. S. P.; Windle, A. H. *Adv. Mater.* **1999**, *11*, 937.
- (60) Geng, H.; Rosen, R.; Zheng, B.; Shimoda, H.; Fleming, L.; Liu, J.; Zhou, O. *Adv. Mater.* **2002**, *14*, 1387.
- (61) Pierard, N.; Fonseca, A.; Konya, Z.; Willems, I.; Tendeloo, V.; Nagy, J. B. *Chem. Phys. Lett.* **2001**, *335*, 1.
- (62) Xia, H.; Wang, Q.; Ki, K.; Hu, G. H. *J. Appl. Polym. Sci.* **2004**, *93*, 378.
- (63) Ghose, S.; Watson, K. A.; Sun, K. J.; Criss, J. M.; Siochi, E. J.; Connell, J. W. *Compos. Sci. Technol.* **2006**, *66*, 1995.
- (64) Ikeda, A.; Hayashi, K.; Konishi, T.; Kikuch, J. *Chem. Commun.* **2004**, 1334.
- (65) Cooper, C. A.; Ravich, D.; Lips, D.; Mayer, J.; Wagner, H. D. *Compos. Sci. Technol.* **2002**, *62*, 1105.
- (66) Haggenueller, R.; Gommans, H. H.; Rnizler, A. G.; Fischer, J. E.;

- Winey, K. I. *Chem. Phys. Lett.* **2000**, *330*, 219.
- (67) Jin, Z.; Pramoda, K. P.; Xu, G.; Goh, S. H. *Chem. Phys. Lett.* **2001**, *337*, 43.
- (68) Fu, K.; Huang, W.; Lin, Y.; Riddle, L. A.; Carroll, D. L.; Sun, Y. P. *Nano Lett.* **2001**, *1*, 439.
- (69) Blake, R.; Gun'ko, Y. K.; Coleman, J.; Cadek, M.; Fonseca, A.; Nagy, J. B.; Blau, W. J. *J. Am. Chem. Soc.* **2004**, *126*, 10226.
- (70) Lou, X.; Detrembleur, D.; Sciannamea, V.; Pagnouille, C.; Jérôme, R. *Polymer* **2004**, *45*, 6097.
- (71) Yao, Z.; Braidy, N.; Botton, G. A.; Adronov, A. *J. Am. Chem. Soc.* **2003**, *125*, 16015.
- (72) Viswanathan, G.; Chakrapani, N.; Yang, H.; Wei, B.; Chung, H.; Cho, K.; Ryu, C. Y.; Ajayan, P. M. *J. Am. Chem. Soc.* **2003**, *125*, 9258.
- (73) Qin, S.; Qun, D.; Ford, W. T.; Resasco, D. E.; Herrera, J. E. *Macromolecules* **2004**, *37*, 752.
- (74) Hwang, G. L.; Shieh, Y. T.; Hwang, K. C. *Adv. Funct. Mater.* **2004**, *25*, 487.
- (75) Wang, M.; Pramoda, K. P.; Goh, S. H. *Polymer* **2005**, *46*, 11510.
- (76) Velasco-Santos, C.; Martinez-Hernández, A. L.; Fisher, F. T.; Ruoff, R.; Castaño, V. M. *Chem. Mater.* **2003**, *15*, 4470.

- (77) Putz, K. W.; Mitchell, C. A.; Krishnamoorti, R.; Green, P. F. *J. Polym. Sci. Part B Polym. Phys.* **2004**, *42*, 2286.
- (78) Son, Y. W.; Cohen, M. L.; Louie, S. G. *Phys. Rev. Lett.* **2006**, *97*, 216803.
- (79) Barone, V.; Hod, O.; Scuseria, G. E. *Nano Lett.* **2006**, *6*, 2748.
- (80) Elf, J.; Li, G. W.; Xie, X. S. *Science* **2007**, *316*, 1191.
- (81) Li, X.; Wang, X.; Zhang, L.; Lee, S.; Dai, H. *Science* **2008**, *319*, 1229.
- (82) Cervantes-Sodi, F.; Piscanec, C. S.; Ferrari, A. C. *Phys. Rev. B* **2008**, *77*, 165427.
- (83) Son, Y. W.; Cohen, M. L.; Louie, S. G. *Nature* **2006**, *444*, 347.
- (84) Dutta, S.; Manna, A. K.; Pati, S. K. *Phys. Rev. Lett.* **2009**, *102*, 096601.
- (85) Li, Y.; Zhou, Z.; Shen, P.; Chen, Z. *ACS Nano* **2009**, *3*, 1952.
- (86) Kan, E. J.; Wu, X.; Li, Z.; Zeng, X. C.; Yang, J.; Hou, J. G. *J. Chem. Phys.* **2008**, *129*, 084712.
- (87) Nduwimana, A.; Wang, X. Q. *ACS Nano* **2009**, *3*, 1995.
- (88) Zhu, L.; Hu, H.; Chen, Q.; Wang, S.; Wang, J.; Ding, F. *Nanotechnology* **2011**, *22*, 185202.
- (89) Hod, D.; Barone, V. Peralta, J. E.; Scuseria, G. E. *Nano Lett.* **2007**, *7*, 2295.

- (90) Kan, E. J.; Li, Z.; Yang, J.; Hou, J. G. *J. Am. Chem. Soc.* **2008**, *130*, 4224.
- (91) Imambekov, A.; Glazman, L. I. *Phys. Rev. Lett.* **2008**, *100*, 206805.
- (92) Ritter, K. A.; Lyding, J. W. *Nat. Mater.* **2009**, *8*, 235.
- (93) Han, M. Y.; Özyilmaz, B.; Zhang, Y.; Kim, P. *Phys. Rev. Lett.* **2007**, *98*, 206805.
- (94) Gunlycke, D.; Areshkin, D. A.; White, C. T. *Appl. Phys. Lett.* **2007**, *90*, 142104.
- (95) Evaldsson, M.; Zozoulenko, I. V.; Xu, H.; Heinzl, T. *Phys. Rev. B* **2008**, *78*, 161407.
- (96) Schubert, G.; Schleede, J.; Fehske, H. *Phys. Rev. B* **2009**, *79*, 235116.
- (97) Cresti, A.; Roche, S. *Phys. Rev. B* **2009**, *79*, 233404.
- (98) Lin, Y. M.; Perebeinos, V.; Chen, Z.; Avouris, P. *Phys. Rev. B* **2008**, *78*, 161409.
- (99) Jiao, L.; Zhang, L.; Wang, X.; Diankov, G.; Dai, H. *Nature* **2009**, *458*, 877.
- (100) Cataldo, F.; Compagnini, G.; Patané, G.; Ursini, O.; Angelini, G.; Ribic, P. R.; Margaritondo, G.; Cricenti, A.; Palleschi, G.; Valentini, F. *Carbon* **2010**, *48*, 2596.
- (101) Cano-Márquez, A. G.; Rodríguez-Macias, F. J.; Campos-Delgado,

- J.; Espinosa-González, C. G.; Tristán-López, F.; Ramirez-González, D.; Cullen, D. A.; Smith, D. J.; Terrones, M.; Vega-Cantú, Y. I. *Nano Lett.* **2009**, *9*, 1527.
- (102) Kosynkin, D. V.; Lu, W.; Sinitskii, A.; Pera, G.; Sun, Z.; Tour, J. M. *ACS Nano* **2011**, *5*, 968.
- (103) Xie, L.; Wang, H.; Jin, C.; Wang, X.; Jiao, L.; Suenaga, K.; Dai, H. *J. Am. Chem. Soc.* **2011**, *133*, 10394.
- (104) Kumar, P.; Panchakarla, L. S.; Rao, C. N. R. *Nanoscale* **2011**, *3*, 2127.
- (105) Shinde, D. B.; Debgupta, J.; Kushwaha, A.; Aslam, M.; Pillai, V. K. *J. Am. Chem. Soc.* **2011**, *133*, 4168.
- (106) Sridhar, V.; Jeon, J. H.; Oh, I. K. *Carbon* **2011**, *49*, 222.
- (107) Elias, A. L.; Botello-Méndez, A. R.; Meneses-Rodríguez, D.; Conzález, V. J.; Ramirez-González, D.; Ci, L.; Muñoz-Sandoval, E.; Ajayan, P. M.; Terrones, H.; Terrones, M. *Nano Lett.* **2010**, *10*, 366.
- (108) Talyzin, A. V.; Luzan, S.; Anoshkin, I. V.; Nasibulin, A. G.; Jiang, H.; Kauppinen, E. I.; Mikoushkin, V. M.; Shnitov, V. V.; Marchenko, D. E.; Noréus, D. *ACS Nano* **2011**, *5*, 5132.
- (109) Paiva, M. C.; Xu, W.; Proença, M. F.; Novais, R. M.; Lægsgaard, E.; Besenbacher, F. *Nano Lett.* **2010**, *10*, 1764.
- (110) Kim, K.; Sussman, A.; Zettl, A. *ACS Nano* **2010**, *5*, 1362.
- (111) Bai, J.; Duan, X.; Huang, Y. *Nano Lett.* **2009**, *9*, 2083.

- (112) Tapasztó, L.; Dobrik, G.; Lambin, P.; Biró, L. P. *Nat. Nanotechnol.* **2007**, *3*, 397.
- (113) McAllister, M. J.; Li, J. L.; Adamson, D. H.; Schniepp, H. C.; Abdala, A. A.; Liu, J.; Herrera-Alonso, M.; Milius, D. L.; Car, R.; Prud'homme, R. K.; Aksay, I. A. *Chem. Mater.* **2007**, *19*, 4396.
- (114) Fujii, S.; Enoki, T. *J. Am. Chem. Soc.* **2010**, *132*, 10034.
- (115) Wei, D.; Liu, Y.; Zhang, H.; Huang, L.; Wu, B.; Chen, J.; Yu, G. *J. Am. Chem. Soc.* **2009**, *131*, 11147.
- (116) Sprinkle, M.; Ruan, M.; Hu, Y.; Hankinson, J.; Rubio-Roy, M.; Zhang, B.; Wu, X.; Berger, C.; de Heer, W. A. *Nat. Nanotechnol.* **2010**, *5*, 727.
- (117) Dössel, L.; Gherghel, L.; Feng, X.; Müllen, K. *Angew. Chem. Int. Ed.* **2011**, *50*, 2540.
- (118) Cai, J.; Ruffieux, P.; Jaafar, R.; Bieri, M.; Braun, T.; Blankenburg, S.; Muoth, M.; Seitsonen, A. P.; Saleh, M.; Feng, X.; Müllen, K.; Fasel, R. *Nature* **2010**, *466*, 470.
- (119) Simon, P.; Gogotsi, Y. *Nat. Mater.* **2008**, *7*, 845.
- (120) Winter, M.; Brodd, R. J. *Chem. Rev.* **2004**, *104*, 4245.
- (121) Vivekchand, S. R. C.; Rout, C. S.; Subrahmanyam, K. S.; Govindaraj, A.; Rao, C. N. R. *J. Chem. Sci.* **2008**, *120*, 9.
- (122) Pandolfo, A. G.; Hollenkamp, A. F. *J. Power Sources* **2006**, *157*, 11.

- (123) Inagaki, M.; Konno, H.; Tanaike, O. *J. Power Sources* **2010**, *195*, 7880.
- (124) Frackowiak, E.; Béguin, F. *Carbon* **2001**, *39*, 937.
- (125) Mayer, S. T.; Pekala, R. W.; Kaschmitter, J. L. *J. Electrochem. Soc.* **1993**, *140*, 446.
- (126) Lota, G.; Krzysztow, F.; Frackowiak, E. *Energy Environ. Sci.* **2011**, *4*, 1592.
- (127) Tao, X. Y.; Zhang, X. B.; Zhang, L.; Cheng, J. P.; Liu, F.; Luo, J. H.; Luo, Z. Q.; Geise, H. J. *Carbon* **2006**, *44*, 1425.
- (128) Xu, C.; Xu, B.; Gu, Y.; Xiong, Z.; Sun, J.; Zhao, X. S. *Energy Environ. Sci.* **2013**, *6*, 1388.
- (129) Yoon, S.; Lee, J.; Hyeon, T.; Oh, S. M. *J. Electrochem. Soc.* **2000**, *147*, 2507.
- (130) Chmiola, J.; Yushin, G.; Gogotsi, Y.; Portet, C.; Simon, P.; Taberna, P. L. *Science* **2006**, *313*, 1760.
- (131) Zhao, X.; Sánchez, B. M.; Dobson, P. J.; Grant, P. S. *Nanoscale* **2011**, *3*, 839.
- (132) Zhi, M.; Xiang, C.; Li, J.; Li, M.; Wu, N. *Nanoscale* **2013**, *5*, 72.
- (133) Deng, W.; Ji, X.; Chen, Q.; Banks, C. E. *RSC Adv.* **2011**, *1*, 1171.
- (134) Snook, G. A.; Kao, P.; Best, A. S. *J. Power Sources* **2011**, *196*, 1.
- (135) Zhang, L.; Zhao, X. S. *Chem. Soc. Rev.* **2009**, *38*, 2520.

- (136) Cho, J.; Daniel, I. M.; Dikin, D. A. *Compos. Part A* **2008**, *39*, 1844.
- (137) Liu, Y. T.; Zhao, W.; Huang, Z. Y.; Gao, Y. F.; Xie, X. M.; Wang, X. H.; Ye, X. Y. *Carbon* **2006**, *44*, 1581.
- (138) Kim, K. H.; Jo, W. H. *Macromolecules* **2007**, *40*, 3708.
- (139) Kim, K. H.; Jo, W. H. *Carbon* **2009**, *47*, 1126.
- (140) Kim, K. T.; Jo, W. H. *Compos. Sci. Technol.* **2009**, *69*, 2205.
- (141) Takahashi, A.; Lin, C. J.; Ohshimizu, K.; Higashihara, T.; Chen, W. C.; Ueda, M. *Polym. Chem.* **2012**, *3*, 479.
- (142) Hodge, P.; Power, G. A.; Rabjohns, M. A. *Chem. Commun.* **1997**, 73.
- (143) Lee, S. K.; Yang, W. J.; Choi, J. J.; Kim, C. H.; Jeon, S. J.; Cho, B. R. *Org. Lett.* **2005**, *7*, 323.
- (144) Bae, W. J.; Kim, K. H.; Park, Y. H.; Jo, W. H. *Chem. Commun.* **2003**, 2768.
- (145) Zou, J.; Liu, L.; Chen, H.; Khondaker, S. I.; McCullough, R. D.; Huo, Q.; Zhai, L. *Adv. Mater.* **2008**, *20*, 2055.
- (146) Zou, J.; Khondaker, S. I.; Huo, Q.; Zhai, L. *Adv. Funct. Mater.* **2009**, *19*, 479.
- (147) Sinani, V. A.; Gheith, M. K.; Yaroslavov, A.; Rakhnyanskaya, A. A.; Sun, K.; Mamedov, A. A.; Wicksted, J. P.; Kotov, N. A. *J. Am. Chem. Soc.* **2005**, *127*, 3463.
- (148) Sandler, J. K. W.; Kirk, J. E.; Kinloch, I. A.; Shaffer, M. S. P.;

- Windle, A. H. *Polymer* **2003**, *44*, 5893.
- (149) Kim, Y. J.; Shin, T. S.; Choi, H. D.; Kwon, J. H.; Chung, Y. C.; Yoon, H. G. *Carbon* **2005**, *43*, 23.
- (150) Hu, G.; Zhao, C.; Zhang, S.; Yang, M.; Wang, Z. *Polymer* **2006**, *47*, 480.
- (151) Jagesar, D. C.; Hartl, F.; Buma, W. J.; Brouwer, A. M. *Chem. Eur. J.* **2008**, *14*, 1935.
- (152) Hecht, D.; Hu, L.; Grüner, G. *Appl. Phys. Lett.* **2006**, *89*, 133112.
- (153) Ryu, S.; Maultzsch, J.; Han, M. Y.; Kim, P.; Brus, L. E. *ACS Nano* **2011**, *5*, 4123.
- (154) Schwab, M. G.; Narita, A.; Hernandez, Y.; Balandina, T.; Mali, K. S.; Feyter, S. D.; Feng, X.; Müllen, K. *J. Am. Chem. Soc.* **2012**, *134*, 18169.
- (155) Xing, T.; Li, L. H.; Hou, L.; Hu, X.; Zhou, S.; Peter, R.; Petracic, M.; Chen, Y. *Carbon* **2013**, *57*, 515.
- (156) Song, Y. J.; Lee, J. U.; Jo, W. H. *Carbon* **2010**, *48*, 389.
- (157) Jung, J. W.; Liu, F.; Russell, T. P.; Jo, W. H. *Energy Environ. Sci.* **2012**, *5*, 6857.
- (158) Caironi, M.; Bird, B.; Fazzi, D.; Chen, Z.; Pietro, R. D.; Newman, C.; Facchetti, A.; Siringhaus, H. *Adv. Funct. Mater.* **2011**, *21*, 3371.
- (159) Cervantes, F.; Csányi, G.; Piscanec, S.; Ferrari, A. C. *Phys. Rev. B*

**2008**, 77, 165427.

(160) Wei, D.; Liu, Y.; Wang, Y.; Zhang, H.; Huang, L.; Yu, G. *Nano Lett.* **2009**, 9, 1752.

(161) Voggu, R.; Rout, C. S.; Franklin, A. D.; Fisher, T. S.; Rao, C. N. R. *J. Phys. Chem. C* **2008**, 112, 13053.

(162) Dong, X.; Fu, D.; Fang, W.; Shi, Y.; Chen, P.; Li, L. J. *Small* **2009**, 5, 1422.

## 초 록

탄소나노재료의 우수한 기계적, 전기적 특성으로 인해 적용분야가 확대됨에 따라 쉽고 효율적인 적용을 위해 용액공정이 가능한 탄소나노재료의 개발이 요구된다. 본 연구에서는 탄소나노재료 특히 carbon nanotube (CNT)와 그래핀을 유기 합성과 기능화를 통해 용액공정이 가능하도록 하였으며, 이를 복합재료의 강화제, 박막트랜지스터의 활성화층, 슈퍼커패시터의 전극물질로 사용하는 연구를 하였다.

CNT는 강한 상호작용에 의해 응집되어 유기용매나 고분자 매트릭스에 분산이 되지 않기 때문에 기능화를 통해 용해성과 혼합성을 향상시켜야 한다. 본 연구에서는 CNT의 고유특성을 저하시키지 않는 non-covalent functionalization을 통해 multi-walled carbon nanotube (MWCNT)를 기능화 하기 위해 상용화재를 합성하였다. Poly(vinyl benzyloxy ethyl naphthalene)-g-poly(methyl methacrylate)와 poly(vinyl benzyloxy methyl naphthalene)-g-poly(*t*-butyl methacrylate-co-methacrylic acid)를 각각 poly(styrene-co-acrylonirile) (SAN)과 Nylon 66 (N66)에 MWCNT를 분산시키기 위한 상용화재로 합성은 성공적으로 이루어졌다. 상용화재의 backbone에 있는 naphthalene은 MWCNT와  $\pi$ - $\pi$  interaction을 하고 graft chain은 고분자 매트릭스와 혼합성을 향상시켜 MWCNT를 고분자 매트릭스내에서 균일하게 분산을 시킨다. SAN/MWCNT와 N66/MWCNT 복합재료에 상용화재를 사용한 경우 균일하게 분산된 MWCNT에 의해

상용화재를 사용하지 않거나 순수 고분자 매트릭스에 비해 인장특성과 전기 전도도가 향상된 복합재료를 제조할 수 있었다. 또한, 상용화재 graft chain에 있는 기능기의 수를 조절하여 MWCNT를 고분자 매트릭스에 분산시켜 그 특성을 확인함으로써 최적의 상용화재의 조건을 확인할 수 있었다.

그래핀은 zero-bandgap 물질로서 metallic property를 갖기 때문에 semiconducting material로 사용할 수 없다. 그래핀의 bandgap을 형성하기 위해 다양한 방법들이 연구되고 있는데 그 중에 그래핀의 폭을 감소시켜 graphene nanoribbon (GNR)을 만들 경우 semiconducting property를 나타낸다. GNR을 만든 방법 중 top-down방법은 GNR의 edge의 결점을 형성시키고, GNR의 형태와 크기를 조절하기 어려우며 만들어진 GNR의 용액공정이 불가능하다는 단점을 지니기 때문에 유기합성을 통해서 용액공정이 가능한 GNR을 제조하였다. 전구체 고분자를 합성 후 cyclodehydrogenation을 통해서 GNR을 형성하였고, 사용한 단량체인 phenylene, naphthalene, anthracene에 따라 폭이 다른 3종류의 GNR을 합성하였다. 합성한 GNR을 유기박막트랜지스터의 활성화층으로 용액공정을 통해 형성하였고, GNR의 전하수송특성을 확인한 결과 ambipolar 전하수송특성을 나타내었다. 3종류의 GNR중 GNR-An이 가장 높은 전하이동도를 보이는데 이는 다른 GNR에 비해 넓은 폭에 의해 conjugation 길이가 길고 결정화도 크기 때문이다.

일반적으로 공기중의 산소와 수분으로 인해 GNR을 쉽게 p-type으로 만들 수 있지만 있는 n-type으로 만들기 어렵다. n-type GNR을 얻기 위해 GNR내에 nitrogen을 도입하고자, benzene대신에

nitrogen이 포함된 pyrazine을 사용하여 전구체 고분자를 합성하였고 pyrazine의 양을 달리하여 총 3종류의 nitrogen-doped GNR (GNR-N)을 합성하였다. GNR 내에 nitrogen의 함량이 증가할수록 ambipolar에서 n-type 전하수송특성으로 변화하였고, nitrogen doping이 되지 않은 GNR보다 100배 높은 전하이동도 ( $0.102 \text{ cm}^2/\text{V}\cdot\text{s}$ )를 갖는 GNR-N100을 합성할 수 있었다.

배터리의 낮은 전력밀도와 긴 충전방전시간의 단점을 슈퍼캐패시터로 대체하고자 하지만, 낮은 성능으로 슈퍼캐패시터의 정전용량을 향상시키고자 하는 연구가 활발히 진행되고 있다. 본 연구에서는 수용성 고분자인 polystyrenesulfonic acid-g-polyaniline (PSSA-g-PANI)를 이용하여 그래핀을 graphite로부터 직접 박리하고 용액공정을 통해 electrode로 제조함으로써 슈퍼캐패시터의 정전용량을 향상시키고자 하였다. PSSA-g-PANI에서 grafting site 수와 PANI의 길이를 달리한 PSSA-g-PANI를 이용하여 6종류의 PSSA-g-PANI/graphene 복합재료를 만들어 정전용량을 측정하였고, grafting site가 적고 PANI의 길이간 긴 PSSA-g-PANI를 이용하여 335 F/g으로 큰 정전용량을 갖는 슈퍼캐패시터 전극물질을 제조할 수 있었다.

주요어: 탄소나노재료, 용액공정, 탄소나노튜브, 상용화재, 복합재료,  
그래핀, 그래핀나노리본, 박막트랜지스터, 슈퍼캐패시터,  
정전용량

학 번: 2011-30181

## List of Papers

1. K. T. Kim and W. H. Jo, *Compos. Sci. Technol.* **2009**, *69*, 2205.
2. K. T. Kim and W. H. Jo, *J. Polym. Sci. Part A: Polym. Chem.* **2010**, *48*, 4184.
3. K. T. Kim and W. H. Jo, *Carbon* **2011**, *49*, 819.
4. S. H. Shim, K. T. Kim, J. U. Lee and W. H. Jo, *ACS Appl. Mater. Interfaces* **2012**, *4*, 4184.
5. M. S. Kang, K. T. Kim, J. U. Lee and W. H. Jo, *J. Mater. Chem. C* **2013**, *1*, 1870.
6. K. T. Kim, J. W. Jung and W. H. Jo, *Carbon* **2013**, *63*, 202.
7. K. T. Kim, J. W. Lee and W. H. Jo, *Macromol. Chem. Phys.* **2013**, *214*, 2768.